

NORTHWESTERN UNIVERSITY

Integrated Material and Process Development for Metal-Organic Frameworks in
Post-Combustion Carbon Capture Applications

A DISSERTATION

SUBMITTED TO THE GRADUATE SCHOOL

IN PARTIAL FUFILLMENT OF THE REQUIREMENTS

for the degree

DOCTOR OF PHILOSOPHY

Field of Chemical and Biological Engineering

By

Karson T. Leperi

Evanston, Illinois

September 2018

Abstract

Integrated Material and Process Development for Metal-Organic Frameworks in Post-Combustion Carbon Capture Applications

Karson Leperi

Pressure swing adsorption (PSA) is a promising technology for carbon capture and sequestration (CCS). However, while there has been much interest in PSA process development, the choice of adsorbent for the separation is just as important as the process configuration. Therefore, it is important to develop PSA processes in conjunction with development of the adsorbent. One class of adsorbents that received significant interest in the past few decades are metal-organic frameworks (MOFs). MOFs are crystalline, porous materials synthesized through self-assembly of metal nodes and organic linkers. Due to the great variety of organic linker and metal node combinations, thousands of potential MOFs can be synthesized and specifically tailored for any applications including CCS. This work focuses on the simultaneous development of MOFs and PSA processes to better understand and improve the process to reduce the cost of CO₂ capture.

First, we investigated the impact of water on the performance of different materials in a two-stage Skarstrom cycle. In this investigation, we found that the dehydration method that resulted in the lowest CO₂ cost was to feed the wet flue gas directly into the column. This resulted in the first section of the column acting as a desiccant, capturing the water, while the remainder of the bed separated the CO₂ from the N₂. From this work we also found that the inclusion of water can shift the ranking of the ideal material, as we saw that zeolite 13X was the best performing material under dry conditions, but zeolite 5A performed equally well under wet conditions. Next, we developed a new general evaluation metric from CO₂ capture cost data for 190 MOFs using the four step Fractionated-Vacuum Pressure Swing Adsorption (FVPSA) cycle. This metric has a higher Spearman correlation coefficient with the cost data than several other metrics

previously proposed, making it useful for future work in quickly evaluating a MOF's potential for CCS applications. In developing the metric, we discovered that the most important feature of this metric is the working capacity of N_2 , followed by the working capacity of CO_2 . We also evaluated 16 MOFs that are reported in the literature to be promising for CCS using a modified Skarstrom cycle to rank them based on economic performance metrics, finding UTSA-16 as the best performer. Finally, we showed that to reduce the computational time for simulating PSA cycles, artificial neural networks (ANNs) are a promising surrogate model that are able to simulate PSA steps that may be used in a given cycle.

Acknowledgements

First and foremost, I would like to thank my advisors, Professors Randall Snurr and Fengqi You. Their guidance, scientific expertise and advice over the last five years have made this dissertation possible. I would also like to thank my thesis committee members, Professors Omar Farha and Neda Bagheri, for constructive feedback and thought-provoking questions.

I want to thank my colleagues and friends in the Snurr group and You group. Members of both groups were instrumental in providing comments and recommendations to improve the content of my research and presentations. I want to single out Dr. Yongchul Chung, Benjamin Bucior, and Daniel Garcia, who helped me with various tasks helping in the completion of this dissertation.

I also want to thank my mother, father, my sisters, Kim, Christie, Amy, Carrie and Kosette, and the rest of my family for their love and encouragement during my Ph.D. career. Finally, I want to thank my wife Paulina, for love, encouragement, and great discussions on statistics and machine learning; I love you.

Table of Contents

Abstract.....	2
Acknowledgements.....	4
List of Figures.....	8
List of Tables.....	14
Chapter 1: Introduction.....	16
1.1. Pressure Swing Adsorption.....	16
1.2. Metal-Organic Frameworks.....	17
1.3. Research Goals and Outline.....	18
Chapter 2: Methodology.....	20
2.1. PSA Modeling.....	20
2.1.1 Adsorbent Equations.....	20
2.1.2 Mass, Energy and Momentum Equations.....	21
2.2. Simulation Methodologies.....	23
2.2.1 Spatial Discretization.....	24
2.2.2 Temporal Integration.....	25
2.3. PSA Operation.....	26
2.3.1 Cycle Configuration.....	26
2.3.2 Boundary Condition Matching with Interacting steps in Multi-bed operation.....	28
2.3.3 Cyclic Steady State.....	29
2.4. NSGA-II Optimization Algorithm.....	31
Chapter 3: Optimization of Two-Stage Pressure/Vacuum Swing Adsorption with Variable Dehydration Level for Post-Combustion Carbon Capture.....	32
3.1. Introduction.....	32
3.2. Methods.....	35
3.2.1 Problem Statement.....	35
3.2.2 P/VSA Model Formulation.....	37
3.2.3 Adsorbent Materials.....	42
3.2.4 Feed Dehydration.....	44
3.2.5 Post Separation Compression.....	47
3.2.6 Process Economics.....	47
3.2.7 Solution Techniques.....	48
3.3. Results and Discussion.....	49
3.3.1 Single-Stage Maximized Purity and Recovery.....	49
3.3.2 Dry Flue Gas, Two-Stage Minimized Cost.....	54

3.3.3	Wet Flue Gas, Two-Stage Minimized Cost	55
3.4.	Conclusion	61
Chapter 4:	Development of a General Evaluation Metric for Rapid Screening of Adsorbent Materials for Post-Combustion CO ₂ Capture.....	62
4.1.	Introduction.....	62
4.2.	Computational Methods.....	66
4.2.1	Widom Particle Insertions.....	66
4.2.2	Grand Canonical Monte Carlo (GCMC) simulations	67
4.2.3	Equilibrium Isotherm Fitting	67
4.2.4	Process Simulation, Optimization, and Economic Analysis	68
4.3.	Results and Discussion	70
4.3.1	Development of a Pre-Screening Heuristic.....	70
4.3.2	MOF Screening.....	73
4.3.3	Evaluation Metrics from the Literature.....	75
4.3.4	General Evaluation Metric (GEM) for MOF Ranking.....	78
4.3.5	Metric Validation	82
4.3.6	High-performing MOFs	86
4.4.	Conclusions.....	86
Chapter 5:	Process-Level Modeling to Evaluate Selected Metal-Organic Frameworks for Post-Combustion Capture	88
5.1.	Introduction.....	88
5.2.	Methodology	88
5.2.1	Adsorbent Isotherm Fitting	88
5.2.2	PSA Cycle.....	90
5.2.3	NSGA Optimization Technique.....	93
5.3.	Results.....	94
5.3.1	Purity / Recovery Maximization.....	94
5.3.2	Economic Analysis	96
5.4.	Conclusion	99
Chapter 6:	Rapid Simulation of Pressure Swing Adsorption Cycles Using Artificial Neural Networks	100
6.1.	Introduction.....	100
6.2.	Methodology	103
6.2.1	Artificial Neural Network Structures.....	103
6.2.2	Data Collection and Initial Training	106
6.2.3	Optimization Framework and ANN Retraining.....	107

6.3. Results.....	108
6.3.1 Three Step Cycle.....	108
6.3.2 Four Step Cycle (Skarstrom Cycle)	114
6.3.3 Five Step Cycle.....	115
6.4. Conclusions.....	120
Chapter 7: Conclusions and Recommendations	121
7.1. Conclusions.....	121
7.2. Recommendation for Future Research.....	122
References.....	123
Appendix A: Nomenclature	135
Appendix B: Economic Equations and Equation Parameters	138
Appendix C: Competitive dual-site Langmuir isotherm validation	149
Appendix D: N ₂ Heat of Adsorption Sensitivity Analysis.....	154

List of Figures

Figure 2.1. Finite volume discretization scheme	24
Figure 2.2. A four step Skarstrom Cycle ⁵⁵ and the pressure profile through one cycle.....	27
Figure 2.3. Internal column profiles for Skarstrom cycle with zeolite 13X as the adsorbent. The profiles correspond to the bed at the end of each step with the colors corresponding to Pressurization (Blue), Adsorption (Green), Depressurization (Red) and Light Reflux (Black).....	28
Figure 2.4. A schematic of the Skarstrom cycle showing the bed operation with four separate steps.	29
Figure 3.1. P/VSA cycle with post-separation compression.....	36
Figure 3.2. (a) CO ₂ isotherms for all materials at 40°C and (b) comparison of the CO ₂ selectivity over N ₂ of each material over the range of temperatures experienced.....	44
Figure 3.3. TEG absorption scheme.....	45
Figure 3.4. Cooling and condensation scheme.	45
Figure 3.5. Total Annualized Cost of dehydration methods.	46
Figure 3.6. Pareto curves for multi-objective optimization of purity and recovery.....	51
Figure 3.7. Internal column profiles for the highest purity shown in Figure 3.6. Solid lines correspond to Zeolite 13X, P _H =4.46 bar, t _{ads} =794 s, t _{pur} =789 s, L=4.28 m, cycle time=1945 s. Dashed lines correspond to HKUST-1, P _H =1.5 bar, t _{ads} =680 s, t _{pur} =646 s, L=4.81 m, cycle time=1642 s. For both materials, the profiles correspond to the bed at the end of each step with the colors corresponding to Pressurization (Blue), Adsorption (Green), Depressurization (Red), and Purge (Black).	52
Figure 3.8. Internal column profiles comparing dry (dashed lines) and wet (solid lines) flue gas using a single stage with zeolite 13X under the same operating parameters. The profiles correspond to the bed at the end of each step with the colors corresponding to Pressurization (Blue), Adsorption (Green), Depressurization (Red), and Purge (Black).	57

Figure 3.9. Internal column profiles of the 1st stage of a two-stage P/VSA system with wet flue gas using zeolite 13X. The profiles correspond to the bed at the end of each step with the colors corresponding to Pressurization (Blue), Adsorption (Green), Depressurization (Red), and Purge (Black). 58

Figure 3.10. Internal column profiles of the 2nd stage of a two-stage P/VSA system like Fig. 3.9 with wet flue gas using zeolite 13X. The profiles correspond to the bed at the end of each step with the colors corresponding to Pressurization (Blue), Adsorption (Green), Depressurization (Red), and Purge (Black). 59

Figure 4.1. Post-combustion carbon capture schematic utilizing the fractionated vacuum pressure swing adsorption (FVPSA) cycle (top insert) for capturing the CO₂. Note that we have considered only the carbon capture portion of the process in this work and have not included the compression costs of the CO₂ product. 70

Figure 4.2. a. Optimal heats of adsorption analysis for the FVPSA cycle using a generic adsorbent material with density of 1.1 g/cm³. Each point represents the highest CO₂ purity that could be achieved while recovering 90% of the CO₂ product. Each line represents a different N₂ internal energy of adsorption. The dashed horizontal line is the DOE target for a CO₂ purity of 90%; b. Minimum energy required to capture a tonne of CO₂ as a function of sorbent density for a generic adsorbent with CO₂ internal energy of adsorption of -32 kJ/mol and N₂ internal energy of adsorption of -10 kJ/mol. The generic adsorbent material in both studies has a single site Langmuir isotherm for CO₂ and N₂, with saturation loading of 10 mol/kg, and an Arrhenius equation pre-exponential parameter of 10⁻¹⁰ Pa⁻¹ and 10⁻⁰⁹ Pa⁻¹ for CO₂ and N₂ respectively. 72

Figure 4.3. Flow diagram for the filtering of candidate MOFs from the CoRE MOF Database. We note that the criteria listed in the boxes are the criteria for keeping MOFs and not removing them. Dark blue boxes contain filters based on intrinsic material properties, such as availability of atomic partial charges and the cost of metal. Sky blue boxes are filters based on the heuristics developed from both GCMC and FVPSA

simulations. Green boxes are filters based on GCMC simulation results. Orange boxes are filters based on FVPSA simulations..... 74

Figure 4.4. a. Relationship between the cost of CO₂ capture and the Separation Factor (SF). For MOFs with low nitrogen working capacity, the SF values are inflated due to very low working capacities of N₂. This leads to no obvious trend between the Separation Factor and the cost of CO₂ capture; b. Relationship between the cost of CO₂ capture and the Modified Separation Factor (with WC_{N₂} < 0.01 mol/kg values set to 0.01 mol/kg), which shows a clearer trend. 77

Figure 4.5. The importance of each feature in the evaluation metric (EM) (equation 4.11) developed in this work for the Spearman correlation coefficient (SCC). The higher the value of SCC, the better the metric is in terms of predicting the cost of CO₂ capture. From right to left, the features are the adsorbent density, the selectivity at adsorption conditions, the internal energy of adsorption of CO₂, the internal energy of adsorption of N₂, the selectivity at desorption conditions, the working capacity of CO₂, and the working capacity of N₂. SCC for each column is calculated with the feature listed on top plus the features listed in the previous columns. For example, the three EM features used to calculate SCC in the third column are the N₂ working capacity, the CO₂ working capacity, and the selectivity at desorption condition. 80

Figure 4.6. Relationship between the four feature General Evaluation Metric (Equation 4.12) and the cost of CO₂ capture. The Spearman correlation coefficient is -0.86..... 81

Figure 4.7. Maximum CO₂ purity as a function of the four feature General Evaluation Metric. Materials that were not able to attain 90% purity are assigned an arbitrary cost of CO₂ capture of \$55 per tonne of CO₂..... 83

Figure 4.8. Validation of the four feature General Evaluation Metric. Results for all nine of the adsorbents in the validation data set, which the GEM was not trained on, are in good agreement with the trend from the training data. The training data is from 190 CoRE MOFs, and the validation data is from 58 CoRE MOF structures that failed the original screening criteria and zeolite 13X. Only those materials able to meet the

purity and recovery requirements are plotted. Adsorption isotherm data for the CoRE MOFs are from GCMC simulations, and isotherm data for zeolite 13X is based on experimental data. ⁵¹	84
Figure 5.1. Schematic of the 5-step modified Skarstrom cycle used in this study. It is noted that the schematic displays the ordering of the steps for a single column. So, one column will first run the pressurization step, followed by the feed step.	92
Figure 5.2. Purity / Recovery Pareto front for the 15 MOFs and Zeolite 13X. Of the 16 adsorbents tested, only 9 were able to achieve the DOE's goals for CO ₂ capture.	95
Figure 5.3. The energy / productivity Pareto front for the 9 adsorbents capable of achieving the DOE's goals. The best performing material from this analysis is UTSA-16. All of these points are ensured to have a CO ₂ purity and recovery above 90%.....	97
Figure 5.4. Pure Component Isotherms for (a) CO ₂ and (b) N ₂ at 313 K. The difference in CO ₂ working capacity between the three materials is visible, explaining the difference in performance.	98
Figure 6.1. Diagram of a Fractionated Vacuum Pressure Swing Adsorption (FVPSA) Cycle and the ANN used to represent the Feed step. The input into the ANN is the column profile at the beginning of the step (which includes all the state variables) and operating parameters important for the feed step. The output of the ANN is the column profile at the end of the Feed step and CO ₂ and N ₂ that is being fed into / emitted from the column during the step.	105
Figure 6.2. A general schematic for the artificial neural network. The initial profile of the column is fed into the input layer along with the operating parameters. The neural network calculates the profile of the column at the end of the step or the CO ₂ / N ₂ that is fed/emitted from the column.	106
Figure 6.3. Flow diagram of the algorithm used to calculate the purity / recovery Pareto front. The ANNs are used with a derivative based optimization solver to calculate the optimal Pareto front. The predicted optimal points are then simulated with the PADE equations to determine the accuracy of the ANN results. If the error between the ANN results and the PDE simulation results is greater than 10 ⁻⁰³ for any point in	

the column, the PDAE simulation results are added to the training data set and the ANNs are retrained with the new training data set. 109

Figure 6.4. Schematics of the three steps tested in this chapter: (a) 3 step cycle, (b) Skarstrom cycle, and (c) 5 step cycle..... 110

Figure 6.5. Comparison of the (a) CO₂ gas mole fraction, (b) CO₂ molar loading, and (C) temperature profiles throughout the column between the neural network and PDAE simulation results for the result with the highest CO₂ purity with a CO₂ recovery of 90%. The different colored data points correspond to the profiles at the end of the Feed Pressurization (red), Feed (blue), and CnC Depressurization (black) steps. From these plots, it is seen that there is good agreement between the ANN and PDAE simulation results, with only small differences at the end of the column during the Feed step. (d) The Pareto front established from the ANNs for the three step PSA cycle. 111

Figure 6.6. Comparison of the (a) CO₂ gas mole fraction, (b) CO₂ molar loading, and (C) temperature profiles throughout the column between the neural network and PDAE simulation results for the result with the highest CO₂ purity with a CO₂ recovery of 91%. The different colored data points correspond to the profiles at the end of the Feed Pressurization (red), Feed (blue), and CnC Depressurization (black) steps. From these plots, we can see that the CO₂ front is not reaching the end of the column at the end of the Feed step. Due to this, there is a significant decrease in the maximum CO₂ purity for a recovery of 90% and 91%. The ANN predicted CO₂ purity and recovery are 76.6% and 91% respectively. The PDAE simulation predicted CO₂ purity and recovery are 76.6% and 90.5% respectively. 112

Figure 6.7. Comparison of the (a) CO₂ gas mole fraction, (b) CO₂ molar loading, and (C) Temperature column profile throughout the column between the neural network and PDE simulation results for the result with the highest CO₂ purity with a CO₂ recovery of 90%. The lines correspond to the profile at the end of the Feed Pressurization (red), Feed (blue), CnC Depressurization (purple), and Light Reflux (black) steps. (d) The Pareto front established from the ANNs for the Skarstrom cycle. 116

Figure 6.8. Comparison of the (a) CO₂ gas mole fraction, (b) CO₂ molar loading, and (C) Temperature column profile throughout the column between the neural network and PDE simulation results for the result with the highest CO₂ purity with a CO₂ recovery of 90%. The lines correspond to the profile at the end of the Light Product Pressurization (red), Feed (blue), Heavy Reflux (purple), CoC Depressurization (black), and CnC Depressurization (green) steps. 117

List of Tables

Table 3.1 Estimated parameters for annualized dehydration cost.....	46
Table 3.2. Upper and lower bounds on the operating parameters for each case study.	51
Table 3.3. Minimum cost breakdown for a two-stage system with dry flue gas. Costs are in \$ million per year.....	53
Table 3.4. Optimal operating parameters for the first stage of the two-stage PSA system with dry flue gas. The cycle time is the sum of the times required for each step.	53
Table 3.5. Optimal operating parameters for the second stage of the two-stage PSA system with dry flue gas. The cycle time is the sum of the times required for each step.....	53
Table 3.6. Minimum cost breakdown for a 2-stage system with wet flue gas. Costs are in \$ million per year	60
Table 3.7. Optimal operating parameters for the first stage of the two-stage PSA system with wet flue gas. The cycle time is the sum of the times required for each step.	60
Table 3.8. Optimal operating parameters for the second stage of the two-stage PSA system with wet flue gas. The cycle time is the sum of the times required for each step.....	60
Table 4.1. Definitions of the various performance metrics found in the literature that are evaluated in this study. Subscripts 1 and 2 represent components 1 and component 2, where 1 is the more strongly adsorbing species	64
Table 4.2. Spearman correlation coefficient between the screening metrics and the CO ₂ capture cost. Metrics that include the working capacity of N ₂ have higher correlation coefficients than the others. The right column is the Spearman correlation coefficient between the CO ₂ capture cost and the evaluation metrics with a minimum N ₂ working capacity of 0.01 mol/kg implemented. It can be seen that by implementing this minimum value, all of the metrics experienced an increase in the magnitude of the correlation.	76

Table 4.3. High-performing metal-organic frameworks from the screening with reported experimental gas adsorption data. Accessible geometric surface area, pore limiting diameter, and largest cavity diameter are calculated using Zeo++ software with probe radius = 1.55 Å.	85
Table 5.1. MOFs investigated during this study along with references for the experimental measurements of their CO ₂ and N ₂ isotherms and heats of adsorption.....	91
Table 5.2. Decision parameters optimized and fixed for the modified Skarstrom cycle	96
Table 5.3. Working capacities of three adsorbents (mol/kg) under adsorption conditions with a CO ₂ mole fraction of 15% and 90%. Adsorption conditions are taken as 1 bar pressure and 313 K. Desorption conditions are taken as a 90:10 CO ₂ :N ₂ stream at 0.1 bar at 313 K.....	98
Table 6.1. The Mean Square Error of the final ANNs (ANNs at the end of the optimization framework) for all data points in the training set. The MSE is broken down by the state variable and the PSA step.	113
Table 6.2. Validation results between the ANNs and PDAE simulations for the three step cycle.	113
Table 6.3. The Mean Square Error of the final ANNs (ANNs at the end of the optimization framework) for all data points in the training set for the Skarstrom cycle. The MSE is broken down by the state variable and the PSA step.	118
Table 6.4. Validation results between the ANNs and PDAE simulations for the Skarstrom cycle.	118
Table 6.5. The Mean Square Error of the final ANNs (ANNs at the end of the optimization framework) for all data points in the training set for the five step PSA cycle. The MSE is broken down by the state variable and the PSA step. From this, we can see the CoC Depressurization step and the Heavy Reflux step had some of the higher errors compared to the other three steps.....	119
Table 6.6. Validation results between the ANNs and PDAE simulations for the Skarstrom cycle.	119

Chapter 1: Introduction

Over recent decades, temperatures around the world have been increasing rapidly. It is widely accepted that this global warming is mainly due to anthropogenic greenhouse gases, especially CO₂. Although there has been substantial effort to develop renewable technologies with minimal net carbon emissions, fossil fuels will continue to play a significant part in the world energy mix. Due to continue significance of fossil fuels in the near term time frame, there is significant interest in methods to reduce the CO₂ emissions from existing power plants. One proposed method is carbon capture and sequestration (CCS). While several technologies exist and have been tested for CCS applications, pressure swing adsorption is one of the most promising due to higher performance and lower energy requirements compared to other technologies.¹⁻⁴

1.1. Pressure Swing Adsorption

Separation of gases accounts for a large fraction of the production costs in the chemical and petroleum industries, along with representing a large fraction of the cost of CCS. With advances in adsorbents, adsorption based separation has seen a considerable increase in applications.⁵⁻⁷ While originally intended for gas drying, adsorption based separation has seen additional uses in hydrogen separation,⁸⁻¹⁰ separation of hydrocarbons,¹¹⁻¹³ methane upgrading,^{14,15} alcohol dehydration¹⁶⁻¹⁸ and isotope enrichment.^{19,20}

Adsorption processes are generally based around porous solid adsorbents that selectively interact with one component of a gaseous mixture over the remaining components. The interactions between the solid and the gas are the basis of the separation process and generally fall into one of three categories: molecular sieving, kinetic separation and equilibrium separation.^{21,22} In molecular sieving, only certain components of a gaseous mixture are able to enter the pores of the adsorbent while the remaining components are excluded. Kinetic separation relies on differences in the diffusion rates between the gas components to separate them. Finally, equilibrium separation is based on differences in the thermodynamic attraction between the adsorbent and the gases.

One of the other important factors for adsorption processes is the method for regenerating the adsorbent. In industrial applications, there are typically multiple columns, where some fraction of the columns are in adsorption mode while the other columns are being regenerated. For the separation of components from a gaseous mixture, two regeneration techniques are typically employed.²¹

1. **Temperature Swing Adsorption (TSA):** In this process, the separation of the gaseous mixture involves the cycling of the temperature of the column. The gas is fed into the column at a low temperature where the heavy product adsorbs while the light product flows through the column. Afterwards, the temperature of the column is raised either through heat applied to the wall of the column or by using a superheated purge gas. One major drawback of TSA is the long cycle time due to the long times required for the heat to transfer throughout the bed. These long cycle times lead to a large bed, which is why TSA is typically used for purification applications.²²
2. **Pressure Swing Adsorption (PSA):** In this process, the separation involves the cycling of the pressure of the column from high adsorption pressures to lower desorption pressures. Due to shorter times required for depressurization, the cycle times of PSA processes are relatively short, which is why it is generally recommended for bulk separation applications such as CCS.²²

1.2. Metal-Organic Frameworks

As described above, one of the most important components of a PSA process is the adsorbent used in the columns. Over the years, many different kinds of adsorbents have been used in PSA and TSA applications, including activated carbon, alumina, hydrotalcites, silica gel, zeolites and carbon molecular sieves.^{23–27} However, one class of materials that has been gaining interest in recent years are metal-organic frameworks (MOFs). MOFs are crystalline, porous materials that are synthesized in a building-block manner using metal “nodes” and organic “linkers.”^{28–30} The building-block synthesis of MOFs allows for them to be specifically tailored to particular application such as CCS.³¹

The wide variety of possible adsorbents has led several researchers to investigate and try to find the ideal adsorbents for various separation applications. In general, researchers have used evaluation metrics based on the pure component and predicted mixture isotherms of a material to assess its performance. These metrics have included the working capacity, selectivity, regenerability and parasitic energy of the material.^{3,32} With such evaluation metrics, recently a large-scale study was performed where over 130,000 hypothetical MOF structures were computationally evaluated.³³ In addition to the previous metrics, other studies have looked into simulating breakthrough of gas mixtures in a fixed bed adsorber.^{34–37} In these studies, the breakthrough time and the concentration profile at the end of the column are used to compare the separation performance of different adsorbent materials, including MOFs.

1.3. Research Goals and Outline

The main goal of this thesis work was the simultaneous investigation into the development of the PSA process along with finding the best performing MOFs for the application. Throughout the dissertation, several different PSA cycles including Skarstrom, FVPSA, and several five step cycles with Heavy Reflux steps are examined and optimized with different adsorbents. This is done in order to find the best cycle for CCS. Along with the process development, we investigated hundreds of different MOFs in order to determine the best properties for predicting high performing adsorbents to provide recommendations for future synthesis research.

In Chapter 2, we introduce the technique for modeling and optimizing PSA systems computationally. First, we provide the sets of partial differential algebraic equations (PDAEs) that describe PSA processes including mass, energy, and momentum balance equations, along with adsorption isotherms and mass transfer equations. We follow this up by discussing methodology for solving the sets of PDAEs, along with the genetic algorithm used to optimize the operating parameters of the PSA system.

In Chapter 3, we explore the effect of water on the performance of different adsorbents in separating CO₂ from N₂. We test two MOFs, HKUST-1 and Ni-MOF-74, and two zeolites, zeolite 5A and 13X, and examine their performance in dry and wet flue gas in a two-stage Skarstrom cycle.

Chapter 4 examines the creation of a general evaluation metric (GEM) for the rapid evaluation of MOFs for CCS applications. Using the calculated cost of CO₂ capture for 190 MOFs found in the Computation-Ready Experimental (CoRE) MOF database,³⁸ the metric is created by finding the most important isotherm features for cost prediction. Once these features are found, we then optimize the exponents on these features to maximize the correlation between the GEM and the CO₂ capture cost for each MOF.

In Chapter 5, 16 MOFs that are reported as promising for CCS applications in the literature are investigated using a modified Skarstrom cycle. We examine the MOF's ability to achieve the CCS goals of a 90% pure CO₂ product while recovering 90% of the CO₂, along with their economic performance through their productivity and energy requirements.

In Chapter 6, we investigate the use of artificial neural networks (ANNs) for rapid simulation of PSA cycles. ANNs are trained as surrogate models for each step of typical PSA cycles. These surrogate models are then used to determine the optimal operating parameters for three different PSA cycles using a derivative-based optimization solver.

Finally, in Chapter 7, conclusions from the previous chapters are summarized and recommendations for future research directions are provided.

Chapter 2: Methodology

2.1. PSA Modeling

2.1.1 Adsorbent Equations

Adsorption Isotherms: Adsorption isotherms define the equilibrium relationship between the concentration of a species in the gas phase and the concentration of the species in the adsorbed phase. It is important that these isotherms are able not only to model the change in the adsorption loading with changing pressure of the species, but also changing temperatures and the presence of other species that will compete for the adsorption sites. In previous work, it has been shown that Langmuir isotherms (single and dual site) work well in representing adsorption isotherms of zeolites and MOFs.^{32,39}*

$$q_i^* = \frac{q_{sat,i,1} B_{i,1} y_i P}{1 + \sum_{i=1}^{n_{comps}} B_{i,1} y_i P} + \frac{q_{sat,i,2} B_{i,2} y_i P}{1 + \sum_{i=1}^{n_{comps}} B_{i,2} y_i P} \quad (2.1)$$

$$B_{i,s} = b_{i,s} \exp\left(\frac{-\Delta U_{i,s}}{RT}\right)$$

where an Arrhenius equation is used to model the adsorption at different temperatures.

Mass Transfer: Along with the molar loading of each gas species, the mass transfer rate of each species from the bulk phase to the adsorbed phase also plays an important part in the separation process. In general, the three main mass transfer resistances to the adsorption uptake are: external fluid film resistance, macropore diffusion and micropore diffusion. It has been previously shown that the external fluid film resistances are often negligible²¹ and micropore diffusion resistance is non-existent or negligible for the adsorbents being investigated.^{40,41} In order to calculate the macropore diffusion, it is necessary to calculate

* A list of important nomenclature is provided in Appendix A

the bulk diffusion coefficient (D_m), which can be estimated with the Chapman-Enskog equation,²¹ and the Knudsen diffusion coefficient, which is calculated with the equation

$$D_{K,i} = 48.5d_{pore} \sqrt{\frac{T}{MW_i}} \quad (2.2)$$

With the Knudsen and the bulk diffusion coefficients, the macropore diffusivity is calculated as follows.

$$D_{p,i} = \frac{\varepsilon_p D_{eff,i}}{\tau} \quad (2.3)$$

$$\frac{1}{D_{eff,i}} = \frac{1}{D_m} + \frac{1}{D_{k,i}}$$

For modeling of the mass transfer, the Linear Driving Force (LDF) model is used, which approximates the intra-particle diffusion with a lumped expression.⁴¹

$$\frac{\partial q_i}{\partial t} = k_i (q_i^* - q_i) \quad (2.4)$$

$$k_i = \frac{15D_{p,i}}{r_p^2}$$

The LDF equation has been widely used in other works.^{39,42,43} It is noted that the LDF model is only applicable when the cycle times of the process are considerably larger than the intra-particle diffusion times.^{44,45}

2.1.2 Mass, Energy and Momentum Equations

Mass Balance: PSA processes generally take place in randomly packed bed adsorption columns with several phenomena interacting with each other such as advection, diffusion and the adsorption and desorption of the gas components. Assuming axially dispersed plug flow in the column and the ideal gas law, the total and individual component mass balances are²¹

$$\frac{1}{P} \frac{\partial P}{\partial t} - \frac{1}{T} \frac{\partial T}{\partial t} = \frac{-T}{P} \frac{\partial}{\partial z} \left(v_z \frac{P}{T} \right) - \frac{(1-\varepsilon)}{\varepsilon} \frac{RT}{P} \sum_{i=1}^{n_{comp}} \frac{\partial q_i}{\partial t} \quad (2.5)$$

$$\begin{aligned} \frac{\partial y_i}{\partial t} = D_L \left(\frac{\partial^2 y_i}{\partial z^2} + \frac{1}{P} \frac{\partial P}{\partial z} \frac{\partial y_i}{\partial z} - \frac{1}{T} \frac{\partial T}{\partial z} \frac{\partial y_i}{\partial z} \right) - v_z \frac{\partial y_i}{\partial z} + \quad & i \in \{1 \dots n_{comps} - 1\} \\ \frac{RT}{P} \frac{(1-\varepsilon)}{\varepsilon} \left((y_i - 1) \frac{\partial q_i}{\partial t} + y_i \sum_{i,i \neq j}^{n_{comps}} \frac{\partial q_i}{\partial t} \right) \quad & (2.6) \end{aligned}$$

Energy Balance: Because adsorption is an exothermic process and the resulting desorption is endothermic, spatial and temporal variations in the temperature occur. While assuming isothermal conditions is an acceptable assumption for purification processes (tasks where the primary adsorbed component is less than 1% of the feed gas), for bulk gas separation it is important to model the temperature and account for temperature variations throughout the column. It is generally assumed that the only temperature gradient present is in the axial direction, and there is negligible difference in temperature between the adsorbent and the gas phase. The column and wall energy balances are

$$\begin{aligned} \left(\varepsilon C_g C_{p,g} + (1-\varepsilon) (C_{p,a} q_{s,0} + C_{p,s} \rho_s) \right) \frac{\partial T}{\partial t} = \\ K_z \frac{\partial^2 T}{\partial z^2} - C_{p,g} C_g v_z \varepsilon \frac{\partial T}{\partial z} - (1-\varepsilon) \rho_s \sum_{i=1}^{n_{comp}} (\Delta H_i) \frac{\partial q_i}{\partial t} + \frac{2h_{i,wall}}{r_{in}} (T_w - T) \quad (2.7) \end{aligned}$$

$$C_{p,w} \rho_w \frac{\partial T_w}{\partial t} = K_w \frac{\partial^2 T_w}{\partial z^2} - \frac{2r_{in} h_{in}}{r_{out}^2 - r_{in}^2} (T_w - T) - \frac{2r_{out} h_{out}}{r_{out}^2 - r_{in}^2} (T_w - T_a) \quad (2.8)$$

However, due to the size of the columns used in industrial applications, it is commonly assumed that the bed behaves adiabatically. This reduces the column energy balance equation to

$$\begin{aligned} \left(\varepsilon C_g C_{p,g} + (1-\varepsilon) (C_{p,a} q_{s,0} + C_{p,s} \rho_s) \right) \frac{\partial T}{\partial t} = \\ K_z \frac{\partial^2 T}{\partial z^2} - C_{p,g} C_g v_z \varepsilon \frac{\partial T}{\partial z} - (1-\varepsilon) \rho_s \sum_{i=1}^{n_{comp}} (\Delta H_i) \frac{\partial q_i}{\partial t} \quad (2.9) \end{aligned}$$

Momentum Balance: As the flue gas flows through the porous bed, it experiences a drop in pressure due to viscous energy losses and drops in kinetic energy. While it is apparent that during pressure changing steps, such as pressurization and depressurization, that pressure drop is important, it has also been shown that pressure drop plays an important role in constant pressure steps such as the Feed step.^{46,47} In packed columns, the Ergun equation is commonly used to describe the pressure drop throughout the bed.

$$-\frac{\partial P}{\partial z} = \frac{150\mu(1-\varepsilon)^2}{4r_p^2\varepsilon^2}v_z + \frac{1.75}{2r_p}\left(\frac{1-\varepsilon}{\varepsilon}\right)\left(\sum_i MW_i \frac{y_i P}{RT}\right)v_z |v_z| \quad (2.10)$$

In the equation above, the first term on the right hand side represents the losses due to viscous flow in the bed, and the second term represents the losses in the kinetic energy due to turbulence.

2.2. Simulation Methodologies

As discussed in section 2.1, PSA processes are modeled with coupled partial differential and algebraic equations (PDAEs) in space and time. While analytical solutions have been obtained,^{21,48,49} these solutions involve significant assumptions such as isothermal conditions, uncoupled isotherms and negligible pressure drops. In order to solve the PDAEs without these assumptions, it is necessary to discretize the spatial or temporal domains or both. In this work, the Method of Lines (MOL) approach is used to solve the PDAEs.⁵⁰ With this approach, the PDAEs are discretized in the spatial domain, converting them to a set of differential algebraic equations (DAEs), which are then integrated using time integration routines. The main advantage of this approach is that it allows for high accuracy in both the spatial and temporal domains of the problem. This is important, as one of the most common features of PSA systems is a steep adsorption in the spatial domain, leading to a stiff problem for the time integration routine to solve. The spatial discretization and temporal integration schemes are discussed in the subsequent sections.

2.2.1 Spatial Discretization

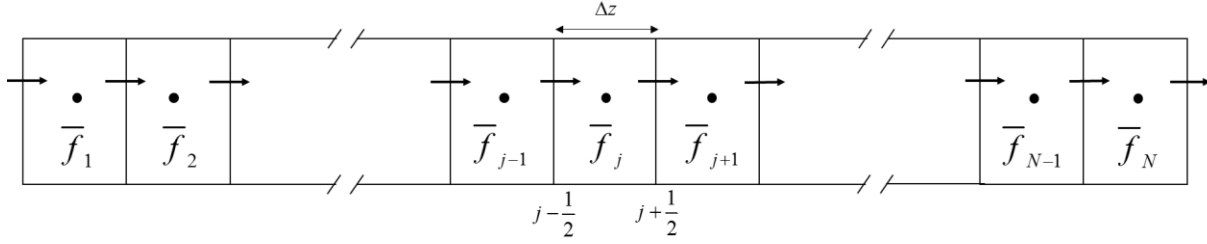


Figure 2.1. Finite volume discretization scheme

As mentioned above, in the MOL approach it is necessary to discretize the spatial domain to convert the PDAEs into a system of DAEs. We use the finite volume method (FVM) as the discretization method. In this approach, the spatial domain is divided into discrete volume elements, as shown in Figure 2.1. In these volumes, the value of each state variable is assigned to be equal to the average value over the entire volume. Using these values, the spatial derivatives are then replaced with the surface fluxes at the boundaries of the volumes. For instance, the first right hand term from equation (2.9) would become the following after finite volume discretization.

$$K_z \frac{\partial^2 T_j}{\partial z^2} = \frac{1}{\Delta z} K_z \left(\frac{T_{j+1} - T_j}{\Delta z} - \frac{T_j - T_{j-1}}{\Delta z} \right) \quad (2.11)$$

In the equation above, $K_z \frac{T_{j+1} - T_j}{\Delta z}$ and $K_z \frac{T_j - T_{j-1}}{\Delta z}$ are the diffusion mass flux terms across the boundaries of volume j . However, while the FVM can be used by itself when diffusion is the dominant term in the equations, additional care needs to be taken when advection becomes the dominant term. In general, higher-order methods are able to model the smooth regions, but they introduce oscillations near steep fronts in the solution. Lower order methods, while ensuring no oscillations, often lack accuracy and flatten the steep front. In order to solve the PDAEs without introducing oscillations or flattening, it is necessary to use flux limiters with the FVM. With flux limiters, higher order methods are used around the smooth areas of

the solution, while lower order methods are used around the discontinuities. One flux limiter that has been shown in previous works^{51,52} to require less computational time to solve PSA problems while maintaining a high accuracy is the weighted essentially non-oscillatory (WENO) scheme. The WENO scheme is

$$f_{j+0.5} = \frac{\alpha_{0,j}}{\alpha_{0,j} + \alpha_{1,j}} \left[\frac{1}{2} (f_{j+1} + f_j) \right] + \frac{\alpha_{1,j}}{\alpha_{0,j} + \alpha_{1,j}} \left(\frac{3}{2} f_j - \frac{1}{2} f_{j-1} \right) \quad (2.12)$$

where $\alpha_{0,j} = \frac{2/3}{(f_{j+1} - f_j + 10^{-10})^4}$ and $\alpha_{1,j} = \frac{1/3}{(f_j - f_{j-1} + 10^{-10})^4}$. It is noted that equation (2.12) is

applicable when $v_{j+0.5} \geq 0$. If the velocity is negative, the following equation is used

$$f_{j+0.5} = \frac{\alpha_{0,j}}{\alpha_{0,j} + \alpha_{1,j}} \left[\frac{1}{2} (f_{j+1} + f_j) \right] + \frac{\alpha_{1,j}}{\alpha_{0,j} + \alpha_{1,j}} \left(\frac{3}{2} f_{j+1} - \frac{1}{2} f_{j+2} \right) \quad (2.13)$$

where $\alpha_{0,j} = \frac{2/3}{(f_j - f_{j+1} + 10^{-10})^4}$ and $\alpha_{1,j} = \frac{1/3}{(f_{j+1} - f_{j+2} + 10^{-10})^4}$

2.2.2 Temporal Integration

After spatial discretization has been performed, a set of DAEs is left. However, due to the stiff nature of the problem, the method chosen for solving the DAEs is important in the accuracy and the computational efficiency of the solution. For solving the DAEs in the temporal dimension, the ode15s solver provided in MATLAB is used.^{53,54} In this solver, numerical differentiation formulas (NDFs) are used along with variable time steps to decrease the computational time required to solve the problem compared to other methods while maintaining a low truncation error.

2.3. PSA Operation

As described in section 1.1, pressure swing adsorption operates cyclically, undergoing adsorption and desorption steps in a packed bed. The desorption step is used to remove the gas that had adsorbed during the adsorption step and is achieved by reducing the pressure of the bed. In Pressure/Vacuum Swing adsorption processes, the adsorption step occurs at pressures higher than atmospheric conditions, while the desorption steps occur under vacuum.

2.3.1 Cycle Configuration

Over the past decades, hundreds of PSA cycle configurations have been developed for a variety of different gas separations. One of the first PSA cycles developed was the Skarstrom cycle, shown in Figure 2.2.⁵⁵ This cycle consists of four steps: pressurization, adsorption, depressurization (counter-current) and light reflux. In the first step, the pressurized flue gas is used to pressurize the column from the feed/heavy product end. In the second step, the flue gas is continuously fed into the column. During this step, the CO₂ (heavy product) is adsorbed while the N₂ (light product) exits out of the top of the column (light product end). After the column has become saturated with CO₂, the column is depressurized from the heavy end, resulting in the CO₂ desorbing and being removed from the column. Finally, a portion of the N₂ gas produced during the adsorption step is used to purge the remaining CO₂ from the column, increasing the recovery. After the light reflux step, the pressurization step is then repeated to continue the process in a cyclic manner. It should be noted that while the figure shows a single column proceeding through all four steps with a tank being used to store some of the N₂, the original patent called for two columns running concurrently but two steps out of sync. This would allow for the N₂ gas from the adsorption step of one

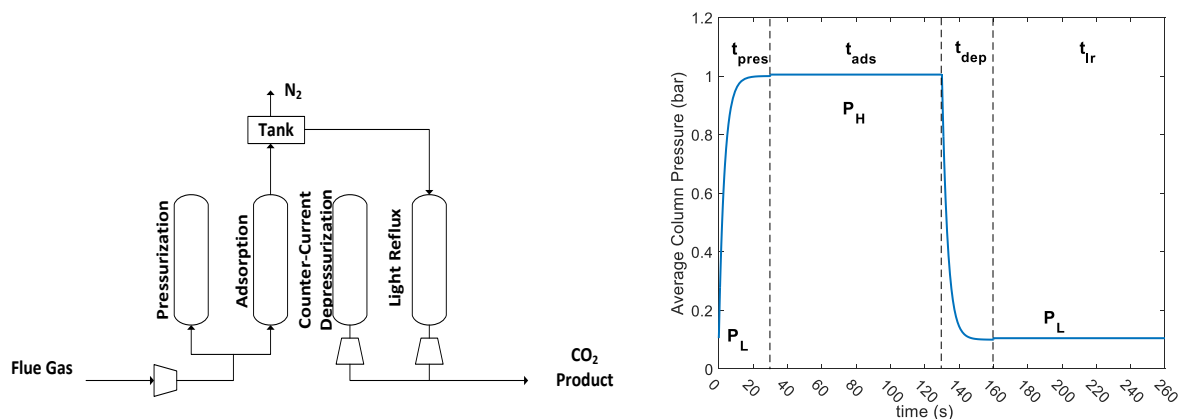


Figure 2.2. A four step Skarstrom Cycle⁵⁵ and the pressure profile through one cycle.

column to be used directly for the light reflux step, without having to store it. In Figure 2.3, the internal column profiles of the CO₂ mole fraction in the gas phase, CO₂ molar loading, N₂ molar loading and column temperature for a Skarstrom cycle with zeolite 13X as the adsorbent are shown.

The Skarstrom cycle represents one of the simplest PSA process operations. Unfortunately, it has been shown in several works to be unable to obtain the high purities of CO₂ necessary for CCS.^{56,57} This is because the cycle was originally designed for operations where the purity of the light product is the highest concern (e.g. hydrogen purification, air dehydration, air separation). In order to improve the purity of the heavy product, several modifications to the cycle have been proposed, including heavy reflux steps, light product pressurization steps, co-current depressurization steps, pressure equilibration steps and adding a second stage where the product from the first stage is the feed of the second stage.^{24–26,39,43,58} All PSA processes differ with respect to which operating steps they employ and their sequence.

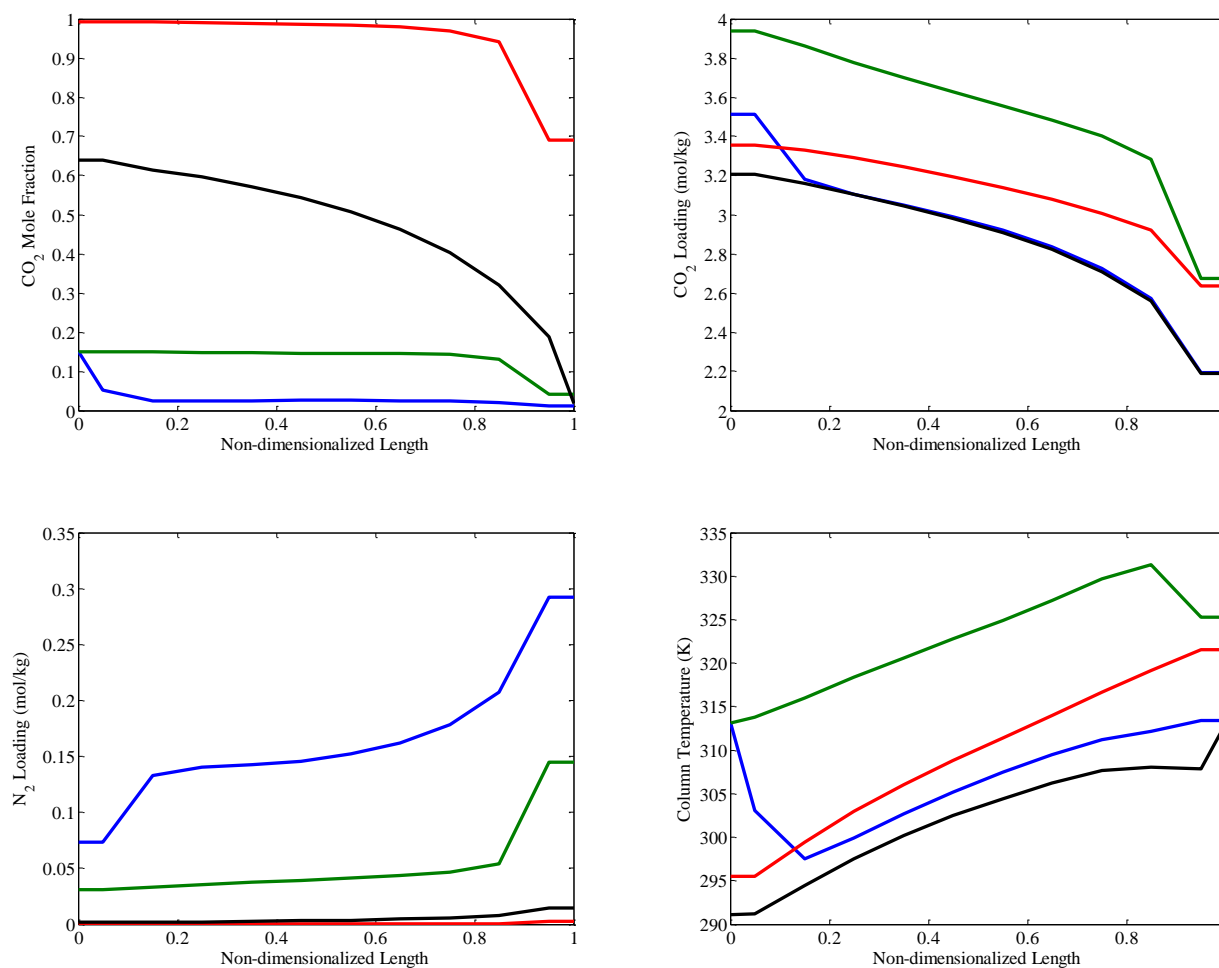


Figure 2.3. Internal column profiles for Skarstrom cycle with zeolite 13X as the adsorbent. The profiles correspond to the bed at the end of each step with the colors corresponding to Pressurization (Blue), Adsorption (Green), Depressurization (Red) and Light Reflux (Black).

2.3.2 Boundary Condition Matching with Interacting steps in Multi-bed operation

In order for PSA cycles to operate continuously, multiple beds are needed to be in operation at all times. This allows one bed to always be performing the separation (pressurization and feed step), while the other bed is being regenerated (depressurization and light reflux steps). However, this presents a challenge, as in order to accurately model the PSA cycle, it is necessary not only to simulate the PSA bed, but also the boundary conditions between interacting steps. As seen in Figure 2.4, in order to accurately simulate the light reflux step, we need to know composition and temperature of the emissions from the feed step. Two

strategies for dealing with boundary condition matching are unibed and multibed simulations. In the unibed approach, only one column is simulated through the entire PSA process and the boundary conditions are stored for the interacting steps. The multibed approach on the other hand simulates all the beds, but only

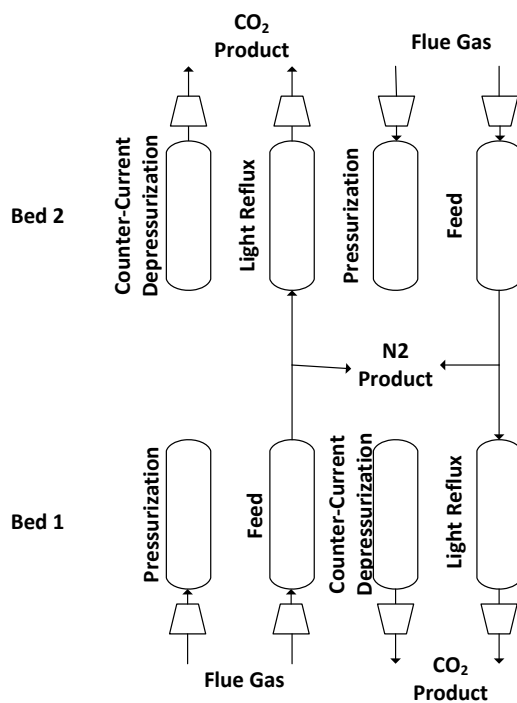


Figure 2.4. A schematic of the Skarstrom cycle showing the bed operation with four separate steps for a portion of the cycle so that all steps are covered between the two beds. This allows the boundary conditions to be matched simultaneously, while the final column profile of one bed must be matched to the initial column profile of the other bed. Since our work has PSA cycles that contain up to 6 steps with complex timing setups, we will use the unibed approach for matching boundary conditions among interacting steps.

2.3.3 Cyclic Steady State

One feature of PSA processes that makes them more complex to solve compared to other separation processes is that they are always operating under transient conditions. As the PSA process switches from

one operating step to another, the boundary conditions around the column change. This results in the process never reaching a steady state. However, after several cycles, PSA processes do reach a state where the conditions in the bed do not change from one cycle to another, which is defined as cyclic steady state (CSS). Therefore, although the bed is constantly changing during a cycle, the conditions of the column remain constant between cycles.

In order to solve for the CSS conditions of a column for a given set of operating conditions, successive substitution is employed to reach the steady state. In this technique, the column is run for one cycle. After one cycle has been run, the cycle is repeated with the conditions of the column at the end of the cycle inputted as the initial conditions for the next cycle. This method is chosen because it replicates the PSA process in real life and is simple to implement compared to other methods for determining CSS. However, with the successive substitution approach, another problem that arises is how to determine when CSS has been achieved. The three definitions that have been used in the literature are:

1. The change in the state variables between consecutive cycles is below a certain relative or absolute threshold.^{26,43,51}
2. The change in PSA performance indicator measurements (e.g. purity, recovery, mass balance) is below a certain relative or absolute threshold.^{25,39,51}
3. The PSA cycle is run for a predefined number of cycles and the conditions of the final cycle are taken as CSS.^{2,40}

In this work, CSS is defined as a combination of the first and second methods. CSS is said to have been reached when the maximum change in the state variables (e.g. molar loading for all components, mole fraction of the gas phase, temperature) is below 0.5%. In addition, in order to ensure no further accumulation is occurring in the column, the ratio of the gas entering the column to the gas exiting the column over the entire cycles needs to be between 0.995 and 1.005 for CSS to be achieved.

2.4. NSGA-II Optimization Algorithm

While it is important to be able to successfully model the PSA process, this is only one part of the overall modeling process. In the Skarstrom cycle shown in Figure 2.2, several of the operating parameters such as the velocity of the feed gas, the length of the column and the time of individual steps can take on a range of values which will have a dramatic effect on the final product. In order to determine the highest purity or lowest cost of the PSA process, it is necessary to use an optimization algorithm to determine the optimal operating values. Several strategies have been successfully used to determine the optimal operating conditions for PSA systems including complete discretization equation based^{56,59} and reduced order modeling.⁶⁰ For this work, a genetic algorithm is used to determine the optimal conditions, specifically the nondominated sorting genetic algorithm II (NSGA-II).⁶¹ NSGA-II is an evolutionary genetic algorithm that has been designed for efficient solution of multi-objective problems. Like most evolutionary algorithms, NSGA-II works by creating an initial population containing random sets of values of the variables and then evaluating these solutions. Then, an offspring population set is created by performing genetic operations such as mutation and cross-over on the parent population. The offspring population is then evaluated. The offspring and the parent population are ranked based on the objective values and the best solutions are selected as the new parent population. Finally, a new offspring population is created and evaluated. This process is repeated until a cutoff criterion is reached, such as maximum number of generations or maximum time evaluation.

In most of this work, the NSGA-II algorithm is used to determine the optimal operating conditions to minimize the overall cost of capturing CO₂ while ensuring that the CO₂ purity and recovery are above 90%. The overall cost of capturing CO₂ includes the operating cost and the capital cost of the entire process.

Chapter 3: Optimization of Two-Stage Pressure/Vacuum Swing Adsorption with Variable Dehydration Level for Post-Combustion Carbon Capture

3.1. Introduction

In 2010, 30.4 gigatons of CO₂ were emitted into the atmosphere worldwide, with around 38% of the emissions in the US coming from the generation of electricity.⁶² To reduce these emissions, there have been substantial efforts to develop renewable energy technologies with minimal net carbon emissions. However, over the next few decades, fossil fuels will continue to play an important role in our energy mix. Therefore, there is a significant interest in reducing the CO₂ emissions from existing power plants via Carbon Capture and Storage (CCS).⁶³ Although several methods exist for CCS, including absorption,^{4,64,65} membranes,^{4,64,66,67} and algae,^{68,69} Pressure/Vacuum Swing Adsorption (P/VSA) is perhaps the most promising method due to its higher performance and lower energy requirements compared to the other technologies.¹⁻⁴ Due to this, P/VSA has been studied extensively for post-combustion carbon capture, including both experimental and computational studies of various process configurations and adsorbent materials.^{2,25,26,39,51,59,70,71} However, in most published investigations, the flue gas being fed into the P/VSA bed is assumed to be completely dehydrated, containing only CO₂ and N₂. In reality, flue gas contains SO_x, NO_x, and water in addition to the CO₂ and N₂. While NO_x and SO_x are already removed from flue gas in many power plants, additional removal of water, if it is required for CCS, would represent an additional cost that must be considered in evaluating CCS technologies.

Several experimental studies have investigated the impact of water on the adsorption of CO₂ for various materials. Wang and LeVan⁷² investigated the effects of water on CO₂ adsorption for zeolites 13X and 5A. They measured the adsorption of CO₂ at water loadings of 1.0 mol/kg, 3.4 mol/kg, and 9.4 mol/kg at temperatures from 0°C to 50°C. Their results showed that at the highest water loading, corresponding to a

relative humidity of less than 1.4%, both of the zeolites experienced a tenfold decrease in CO₂ adsorption. Liu et al.⁷³ investigated the adsorption of pure component CO₂ and H₂O, along with their mixtures, in the metal-organic frameworks (MOFs) HKUST-1 and Ni-MOF-74. They determined that the two MOFs were able to maintain higher CO₂ loadings at high water loadings compared to zeolites 13X and 5A. In another work, Yazaydin et al.⁷⁴ computationally and experimentally showed that CO₂ adsorption in HKUST-1 can be slightly enhanced by hydrating the crystal to 4 wt% compared to a fully dehydrated sample. In this system, the water molecules coordinated to the open metal sites of the MOF, and the enhanced CO₂ adsorption was attributed to higher Coulombic interactions between the water and CO₂ molecules compared to the interactions between the MOF and CO₂.

In addition to studies of CO₂/water mixtures on different adsorbent materials, there have been several experimental investigations of P/VSA systems for post-combustion CO₂ capture with wet flue gas streams. Li et al.⁷⁵ experimentally demonstrated the effect of water on the performance of a VSA process for carbon capture. The VSA process used zeolite 13X as the adsorbent and consisted of three steps: pressurization, adsorption with the feed gas, and counter-current evacuation. With dry flue gas, the process achieved a recovery of 78.5% and a purity of 69%, with a column productivity of 0.287 kg CO₂/(hr·kg adsorbent). When wet flue gas was used, the recovery dropped to 60.4%, the productivity dropped to 0.225 kg CO₂/(hr·kg adsorbent), and the purity rose to 72%. This change in performance was due to water adsorbing in the zeolite, reducing the CO₂ capacity of the adsorbent. In a follow up study, Li et al.⁷⁶ examined the use of a layered bed using zeolite 13X along with F200 and CDX-activated alumina as the desiccant. With the layered bed, they were able to achieve a CO₂ purity of 74.8% and a recovery of 77.6%.

The effect of water on the performance of a VSA process from an optimization perspective has been studied by Krishnamurthy et al.²⁷ They studied the effect of water on the performance of a 4-step VSA process with zeolite 13X. They showed that, although the process was still able to achieve the overall goal of 95% purity and 90% recovery, the water increased the energy consumption to 230 kWh/ton and reduced

the productivity of the bed to 1.03 tons of $\text{CO}_2/(\text{m}^3 \text{ adsorbent} \cdot \text{day})$. This is compared to the dry flue gas case, where the energy consumption was 154 kWh/ton and the productivity was 1.52 tons of $\text{CO}_2/(\text{m}^3 \text{ adsorbent} \cdot \text{day})$. They also examined a new two-bed, dual-adsorbent process. The first bed contained silica gel and dehydrated the flue gas before feeding the product to the second bed containing zeolite 13X. With this configuration, they were able to achieve a minimum energy consumption of 177 kWh/ton and a productivity of 1.29 tons/ $(\text{m}^3 \text{ adsorbent} \cdot \text{day})$ for wet flue gas.

Even with recent research progress on adsorption technologies for carbon capture, there are still significant gaps in our knowledge. Although several studies have investigated the detrimental effect of water on the performance of the system and the systematic optimization of the process to overcome this, most CCS studies treat the stream entering the CO_2 capture unit as either fully saturated with water or bone dry. However, using standard technology for water removal prior to CO_2 capture, the water level could be treated as a decision variable. To the best of our knowledge, no work has attempted to optimize the humidity level to minimize the overall cost of adsorption-based carbon capture. In addition, most work on process-level optimization of P/VSA processes only investigated a single adsorbent material. A notable exception is the work of Hasan et al.,⁴⁰ where 70 zeolites were evaluated using full process optimization after first screening through hundreds of zeolite structures.

In this work, we aim to provide insight into the optimal operating conditions for various adsorbents for post-combustion CO_2 capture at the lowest total cost including the costs of dehydration and compression. We develop a detailed P/VSA simulation model that accounts for pressure drop, heat effects, isotherm non-linearity, and deleterious effects of water on the adsorption of CO_2 . We then use this model to simulate a two-stage Skarstrom cycle and optimize several operating parameters including the water level in the gas stream that enters the P/VSA system, in order to give the lowest cost while maintaining necessary purity and recovery constraints. This optimization is performed for two zeolites and two MOFs. Finally, we use

the results to compare the performance of the different materials in order to gain insight into the optimal water level in the flue gas to minimize the total cost.

3.2. Methods

In this section, we describe the process model for the P/VSA technology, the feed dehydration technologies, and the compression of the CO₂ product. These models are used to simulate the process, which is then optimized to determine the minimum cost of CO₂ capture for each adsorbent material.

3.2.1 Problem Statement

The overall goal of this work is to determine the minimum cost for separating CO₂ from flue gas and compressing it for pipeline transportation. It is assumed that the flue gas is at 1 atm and 313 K, with a composition of 14.1 mol% CO₂, 5.5 mol% H₂O, and the remainder N₂.⁷⁷ The total flow rate of the flue gas is assumed to be 1 kmol/s, approximately equivalent to the emissions from a 30 megawatt coal power plant.⁷⁸ It is noted that 30 MW is a small scale power plant, and additional issues might arise from scaling up the process, primarily due to uncertainty of adsorbent costs and required vacuum pressures. For the final product, the purity and recovery are both set to 90% for most calculations; some additional calculations using 95% purity are presented in the Appendix B. The purity and recovery are set to minimize compression costs for pipeline transportation and ensure that a significant portion of the CO₂ emission is captured. For pipeline transportation, the CO₂ product is then compressed to 110 bar and maintained below 35°C. A Skarstrom cycle is used as the cycle configuration due to its operational simplicity and its long history of use in industry. The cycle consists of the following steps: 1) Pressurization, 2) Adsorption, 3) Counter-Current Depressurization, and 4) Light-Product Purge.²¹ The bed begins at the low pressure (P_L). During the pressurization step, the flue gas is used to raise the pressure of the column from the low pressure to the high pressure (P_H). After the bed is pressurized, the valve at the end of the column is opened and the flue gas flows through the bed, with relatively pure N₂ leaving the bed. When the bed is almost saturated, the valve at the end of the column is closed, and the bed is depressurized from the front end. Finally, after the

column is depressurized, some of the N_2 gas from the adsorption step is fed into the end of the column to increase the recovery of CO_2 . In order to meet the purity and recovery constraints, a two-stage Skarstrom cycle is used, where the product stream from the first stage is fed into the second stage. This configuration has been studied theoretically^{24,25,79,80} and experimentally,^{58,81} showing that over 90% purity and recovery can be achieved. The overall two-stage P/VSA system with the compression chain is shown in Figure 3.1. Although two-stage PSA systems are directly linked together in industrial applications, for this work, it is assumed that there is a buffer tank between the two stages, allowing a uniform feed stream for the second stage.

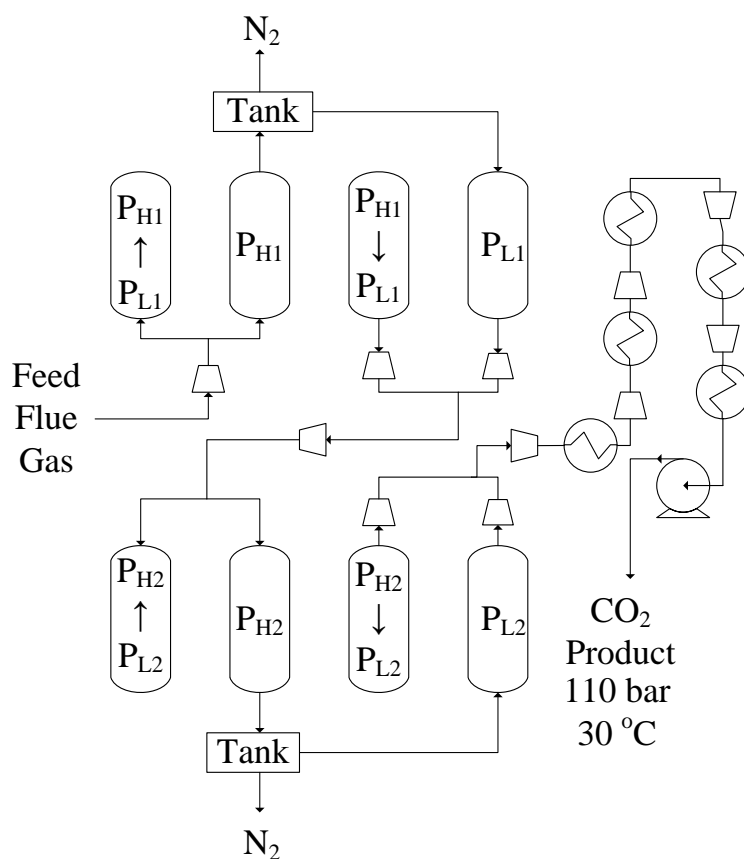


Figure 3.1. P/VSA cycle with post-separation compression

3.2.2 P/VSA Model Formulation

The adsorption model used in this work involves a system of coupled partial differential equations (PDEs) and non-linear algebraic equations.²¹ The following assumptions are made:

- The Ideal Gas Law accurately describes the gas phase;
- The viscosity of the gas is independent of pressure;
- There are no radial effects in the concentration, pressure, or temperature in both the gas and solid phase;
- There is thermal equilibrium between the gas phase and the solid phase;
- The Ergun equation is used to represent the axial pressure drop;
- The particle size and void fraction are constant throughout the bed;
- The linear driving force model⁴¹ is used to describe gas diffusion into the adsorbent;
- The temperature outside the wall is maintained constant.

All of the equations used in the model are put into non-dimensional forms. The non-dimensional variables are as follows:

$$\begin{aligned}
 \bar{P} &= \frac{P}{P_0}; & \bar{T} &= \frac{T}{T_0}; & \bar{T}_w &= \frac{T_w}{T_0}; & x_i &= \frac{q_i}{q_{s0}} \\
 \bar{u}_z &= \frac{u_z}{u_0}; & \tau &= \frac{tu_0}{L}; & x_i^* &= \frac{q_i^*}{q_{s0}}; & \bar{T}_a &= \frac{T_a}{T_0} \\
 \bar{P}_L &= \frac{P_L}{P_0}; & Z &= \frac{z}{L}
 \end{aligned} \tag{3.1}$$

In our model, we use the following component mass balance to calculate the mole fraction of CO₂ (y_i) in the gas phase:

$$\frac{\partial y_i}{\partial \tau} = \frac{1}{Pe} \left(\frac{\partial^2 y_i}{\partial Z^2} + \frac{1}{\bar{P}} \frac{\partial \bar{P}}{\partial Z} \frac{\partial y_i}{\partial Z} - \frac{1}{\bar{T}} \frac{\partial y_i}{\partial Z} \frac{\partial \bar{T}}{\partial Z} \right) - \bar{u}_z \frac{\partial y_i}{\partial Z} + \frac{\psi \bar{T}}{\bar{P}} \left((y_i - 1) \frac{\partial x_i}{\partial \tau} + y_i \frac{\partial x_{N_2}}{\partial \tau} \right) \tag{3.2}$$

where $Pe = u_0 L / D_L$ and $\psi = [(1 - \varepsilon) / \varepsilon] (RT_0 q_{s0} / P_0)$. The axial dispersion coefficient, D_L , is given by the following equation:²¹

$$D_L = 0.7D_m + r_p u_0 \quad (3.3)$$

The mole fraction of N_2 is calculated through the equation:

$$y_{CO_2} + y_{N_2} = 1 \quad (3.4)$$

The overall mass balance results in the following equation for calculating the total pressure:

$$\frac{\partial \bar{P}}{\partial \tau} = \left(-\bar{P} \frac{\partial \bar{u}_z}{\partial Z} - \bar{u}_z \frac{\partial \bar{P}}{\partial Z} + \bar{u}_z \frac{\bar{P}}{T} \frac{\partial \bar{T}}{\partial Z} \right) - \psi \bar{T} \sum_i \frac{\partial x_i}{\partial \tau} + \frac{\bar{P}}{T} \frac{\partial \bar{T}}{\partial \tau} \quad (3.5)$$

The following energy balance is used to represent the temperature in the wall:

$$\frac{\partial \bar{T}_w}{\partial \tau} = \pi_1 \frac{\partial^2 \bar{T}_w}{\partial Z^2} + \pi_2 (\bar{T}_w - \bar{T}) - \pi_3 (\bar{T}_w - \bar{T}_a) \quad (3.6)$$

where

$$\pi_1 = \frac{K_w}{\rho_w C_{p,w} u_0 L} \quad (3.7)$$

$$\pi_2 = \frac{2r_i h_{in} L}{\rho_w C_{p,w} u_0 (r_o^2 - r_i^2)} \quad (3.8)$$

$$\pi_3 = \frac{2r_o h_{out} L}{\rho_w C_{p,w} u_0 (r_o^2 - r_i^2)} \quad (3.9)$$

The temperature of the gas and solid phases in the column are calculated by the following equation:

$$\frac{\partial \bar{T}}{\partial \tau} = \pi_4 \frac{\partial^2 \bar{T}}{\partial Z^2} - \pi_5 \bar{u}_z \frac{\partial \bar{T}}{\partial Z} + \sum_i (\pi_{6i} + \pi_7 \bar{T}) \frac{\partial x_i}{\partial \tau} - \pi_8 (\bar{T} - \bar{T}_w) \quad (3.10)$$

where

$$\pi_4 = \frac{K_z}{(\rho_g C_{p,g} \varepsilon + (1-\varepsilon)(C_{p,s} \rho_s + C_{p,a} q_{s0})) u_0 L} \quad (3.11)$$

$$\pi_5 = \frac{\rho_g C_{p,g} \varepsilon}{(\rho_g C_{p,g} \varepsilon + (1-\varepsilon)(C_{p,s} \rho_s + C_{p,a} q_{s0}))} \quad (3.12)$$

$$\pi_{6i} = \frac{(1-\varepsilon)(-\Delta H_i) q_{s0}}{T_0 (\rho_g C_{p,g} \varepsilon + (1-\varepsilon)(C_{p,s} \rho_s + C_{p,a} q_{s0}))} \quad (3.13)$$

$$\Delta H_i = \Delta U_i - R \bar{T} T_0 \quad (3.14)$$

$$\pi_7 = \frac{(1-\varepsilon)(C_{p,g} - C_{p,a}) q_{s0}}{(\rho_g C_{p,g} \varepsilon + (1-\varepsilon)(C_{p,s} \rho_s + C_{p,a} q_{s0}))} \quad (3.15)$$

$$\pi_8 = \frac{2h_m L}{r_i u_o (\rho_g C_{p,g} \varepsilon + (1-\varepsilon)(C_{p,s} \rho_s + C_{p,a} q_{s0}))} \quad (3.16)$$

$$\rho_g = \frac{\bar{P} P_H}{R \bar{T} T_0} \quad (3.17)$$

The linear driving force (LDF) is used to calculate the mass transfer between the gas phase and the solid phase.

$$\frac{\partial x_i}{\partial \tau} = \frac{k_i L}{u_0} (x_i^* - x_i) \quad (3.18)$$

The pressure drop throughout the column is calculated using the Ergun equation.

$$-\frac{\partial \bar{P}}{\partial Z} = \frac{150\mu(1-\varepsilon)^2 Lu_0}{4r_p^2 P_0 \varepsilon^3} \bar{u}_z + \frac{1.75(1-\varepsilon) Lu_0^2}{2r_p P_0 \varepsilon^3} \left(\sum_i MW_i y_i \rho_g \right) \bar{u}_z \left| \bar{u}_z \right| \quad (3.19)$$

For all of the equations above, the parameters used for the simulation are provided in Appendix B. In order to solve these equations, the initial and boundary conditions of the column need to be known. When initializing the simulation, it is assumed the bed and the column wall are in equilibrium with the flue gas at atmospheric temperature. Since the first step in the Skarstrom cycle is the pressurization step, the pressure in the bed is initially at the purge pressure.

$$\bar{P} = \bar{P}_L; \quad y_i = y_{feed}; \quad \bar{T} = \bar{T}_a; \quad x_i = x_i^* |_{y_{feed}}; \quad \bar{T}_w = \bar{T}_a \quad (3.20)$$

After starting up, the initial conditions of each step are assumed to be the same as the bed profile at the end of the previous step. The boundary conditions for each step are provided below, where $Z=0^+$ and $Z=1^-$ are the two ends of the column. For the pressurization step at $Z=0^+$ and $Z=1^-$, the boundary conditions are given by equations (3.21) and (3.22), respectively.

$$\bar{P} = \bar{P}_L \rightarrow 1; \quad y_i = y_{feed}; \quad \bar{T} = 1; \quad \bar{T}_w = \bar{T}_a \quad (3.21)$$

$$\frac{\partial \bar{P}}{\partial Z} = 0; \quad \frac{\partial y_i}{\partial Z} = 0; \quad \frac{\partial \bar{T}}{\partial Z} = 0; \quad \bar{T}_w = \bar{T}_a \quad (3.22)$$

The boundary conditions for the adsorption step at $Z=0^+$ and $Z=1^-$ are given by equations (3.23) and (3.24).

$$\bar{P} = 1.05; \quad y_i = y_{feed}; \quad \bar{T} = 1; \quad \bar{T}_w = \bar{T}_a \quad (3.23)$$

$$\bar{P} = 1; \quad \frac{\partial y_i}{\partial Z} = 0; \quad \frac{\partial \bar{T}}{\partial Z} = 0; \quad \bar{T}_w = \bar{T}_a \quad (3.24)$$

It is noted that for the adsorption step, the inlet pressure is used as the inlet boundary condition, from which the inlet velocity is then calculated. The boundary conditions for the depressurization step at $Z=0^+$ and $Z=1^-$ are given by equations (3.25) and (3.26).

$$\bar{P} = 1 \rightarrow \bar{P}_L; \quad \frac{\partial y_i}{\partial Z} = 0; \quad \frac{\partial \bar{T}}{\partial Z} = 0; \quad \bar{T}_w = \bar{T}_a \quad (3.25)$$

$$\frac{\partial \bar{P}}{\partial Z} = 0; \quad \frac{\partial y_i}{\partial Z} = 0; \quad \frac{\partial \bar{T}}{\partial Z} = 0; \quad \bar{T}_w = \bar{T}_a \quad (3.26)$$

The boundary conditions for the purge step at $Z=0^+$ and $Z=1^-$ are given by equations (3.27) and (3.28).

$$\bar{P} = \bar{P}_L; \quad \frac{\partial y_i}{\partial Z} = 0; \quad \frac{\partial \bar{T}}{\partial Z} = 0; \quad \bar{T}_w = \bar{T}_a \quad (3.27)$$

$$\bar{P} = 2\bar{P}_L; \quad y_i = y_{i,ads}; \quad \bar{T} = \bar{T}_{ads}; \quad \bar{T}_w = \bar{T}_a \quad (3.28)$$

where $y_{i,ads}$ and T_{ads} are the time averaged mole fraction and temperature during the adsorption step at the $Z=1^-$ boundary.

This Skarstrom cycle is continuously simulated until a cyclic steady state (CSS) is reached, which happens when the changes in the state variables are less than 0.5% between the end of the purge step and the beginning of the pressurization step. Once the bed has reached CSS, the performance of the process is evaluated via the purity of the CO_2 stream and the recovery of the CO_2 , which is calculated as the CO_2 that is not lost during the adsorption step (see Appendix B). When the wet flue gas is used as the feed, the purity is calculated on a dry basis, as it is assumed that the water can easily be separated from the CO_2 while the product is being prepared for pipeline transportation.

3.2.3 Adsorbent Materials

For this study, four materials are chosen: zeolite 5A, zeolite 13X, and the MOFs Ni-MOF-74 and HKUST-1. For all these materials, dual-site competitive Langmuir adsorption with temperature dependent isotherm parameters are used to describe the adsorption. For zeolite 5A, HKUST-1, and Ni-MOF-74, experimental CO₂ and N₂ isotherms⁸²⁻⁸⁶ were retrieved from the literature and fitted to the following equations:

$$q_i^* = \frac{q_{b,i} B_i y_i P}{1 + \sum_i B_i y_i P} + \frac{q_{d,i} D_i y_i P}{1 + \sum_i D_i y_i P}$$

$$B_i = b_i \exp\left(-\frac{\Delta U_{b,i}}{RT}\right)$$

$$D_i = d_i \exp\left(-\frac{\Delta U_{d,i}}{RT}\right)$$
(3.29)

Zeolite 13X is described by the following dual site Langmuir equations given by Haghpanah et al.⁵¹

$$q_i^* = \frac{q_{b,i} B_i C_i}{1 + \sum_i B_i C_i P} + \frac{q_{d,i} D_i C_i}{1 + \sum_i D_i C_i P}$$

$$B_i = b_i \exp\left(-\frac{\Delta U_{b,i}}{RT}\right)$$

$$D_i = d_i \exp\left(-\frac{\Delta U_{d,i}}{RT}\right)$$
(3.30)

where C is the molar concentration in the gas phase moles per cubic meter. The fitted isotherms at 40°C and the selectivity at 1 bar for each material are displayed in Figure 3.2.

When humid flue gas is used as the feed to the P/VSA system, the impact of water on the performance is accounted for by reducing the equilibrium molar loading of the adsorbent for both CO₂ and N₂

$$q_{i,humid}^* = \alpha \cdot q_{i,dry}^*$$
(3.31)

where α is the impact factor of water on the CO₂ and N₂ uptake. It is assumed that the presence of water equally impacts the adsorption of N₂ and CO₂. Using the results of Liu et al.⁷³ and Yu et al.,⁷² the impact of water is accounted for in the simulation through the following equation:

$$\alpha = \begin{cases} e^{-cq_w}, & Z \leq \frac{L_{wl}}{L} \\ 1, & Z > \frac{L_{wl}}{L} \end{cases} \quad (3.32)$$

where q_w is the water loading predicted from the isotherms, and L_{wl} is the penetration length of the water front. The water isotherms for both zeolites are given by a Toth isotherm:⁸⁷

$$q_w = \frac{a \cdot wl \cdot P}{\left[1 + (b \cdot wl \cdot P)^t\right]^{1/t}} \quad (3.33)$$

The water isotherm of Ni-MOF-74 is given by⁷³

$$q_w = \frac{q_b b P_{H_2O}}{1 + b P_{H_2O}} + \frac{q_d d P_{H_2O}}{1 + d P_{H_2O}} \quad (3.34)$$

$$P_{H_2O} = wl \cdot \min(100 \text{ kPa}, P)$$

where wl is the mole fraction of water in the gas. Finally, the water isotherm of HKUST-1 is given by⁷³

$$q_{H_2O} = aP_{H_2O}^5 + bP_{H_2O}^4 + cP_{H_2O}^3 + dP_{H_2O}^2 + eP_{H_2O} \quad (3.35)$$

$$P_{H_2O} = wl \cdot \min(100 \text{ kPa}, P)$$

The length of the water front penetration is calculated through the following equation.

$$L_{wl} = \frac{F \cdot wl \cdot t_c}{\pi r_m^2 \rho_s (1 - \varepsilon) (q_w|_{P=P_H} - q_w|_{P=P_L})} \quad (3.36)$$

The isotherm parameters for all of the materials are provided in Tables B2.3-B2.5.

3.2.4 Feed Dehydration

Two dehydration technologies were developed for analysis: triethylene glycol (TEG) absorption and cooling and condensation (C&C). In TEG absorption, the flue gas is fed into the bottom of an absorption column with lean TEG fed from the top as shown in Figure 3.3. The TEG absorbs the water from the gas. The TEG is then regenerated through distillation. In C&C, the flue gas is chilled through a refrigeration cycle incorporating Refrigerant-152a. The liquid water is then separated from the flue gas in a flash drum as shown in Figure 3.4.

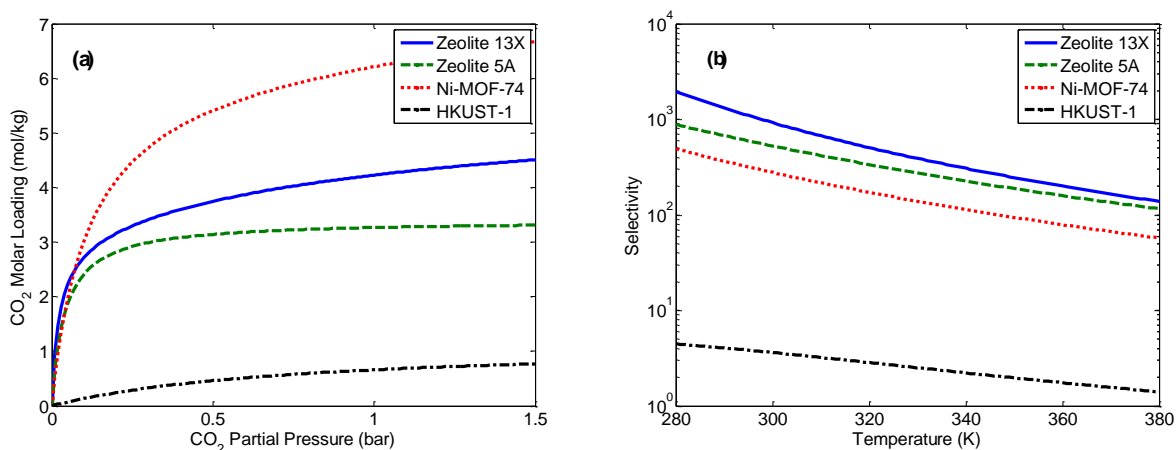


Figure 3.2. (a) CO₂ isotherms for all materials at 40°C and (b) comparison of the CO₂ selectivity over N₂ of each material over the range of temperatures experienced.

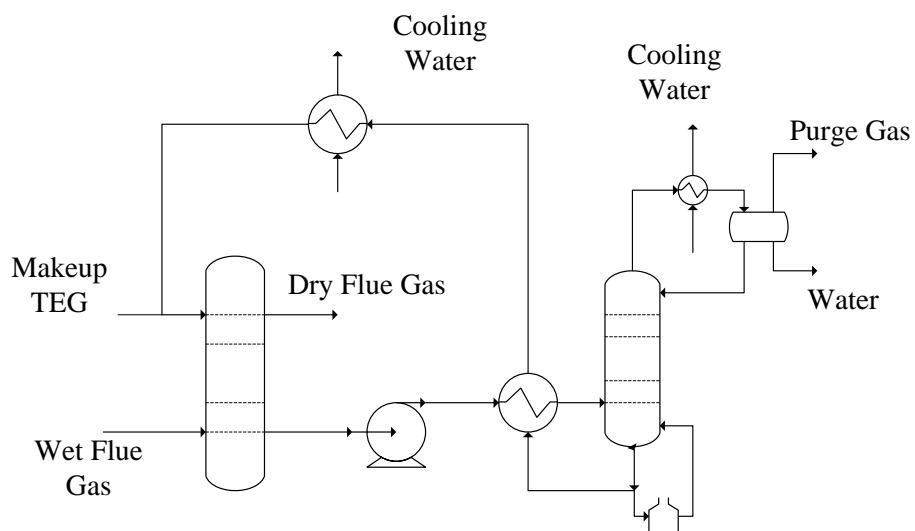


Figure 3.3. TEG absorption scheme.

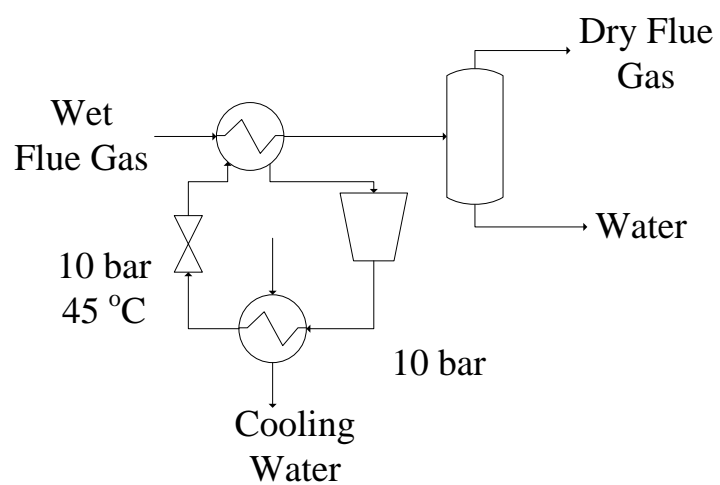


Figure 3.4. Cooling and condensation scheme.

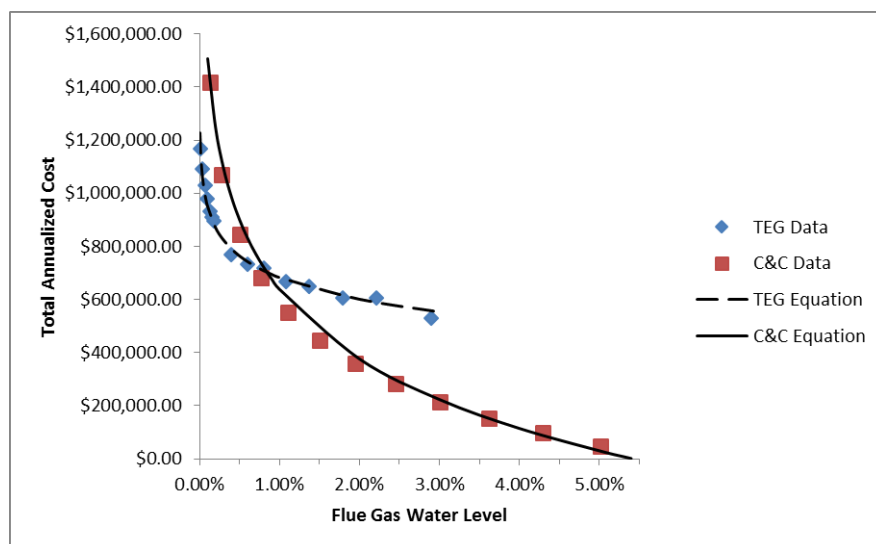


Figure 3.5. Total Annualized Cost of dehydration methods.

Table 3.1 Estimated parameters for annualized dehydration cost.

Technology	a (\$/year)	b (\$/year)
Cooling and Condensation	-377,405	-1,100,000
TEG Absorption	-118,480	137,095

For both technologies, Aspen HYSYS was used to simulate the process, and total annualized costs were estimated using relevant literature as described in Appendix B.^{88,89} The costs of the processes were then fitted to logarithmic functions based on the desired water level as shown in Figure 3.5 in order to integrate the dehydration technologies with the P/VSA system. This allows the water level of the gas entering the P/VSA unit to be modeled as a continuous operating parameter instead of as discrete points as in our previous preliminary investigation.⁹⁰ The general equation for the Total Annualized Cost of dehydration is

$$DC = a \cdot \ln(wl) + b \quad (3.37)$$

with the coefficients for each technology provided in Table 3.1. The dependence of the total cost on the required dehydration level for each technology is shown in Figure 3.5. At lower levels of dehydration (i.e., higher amounts of water remaining in the treated gas stream), C&C is cheaper due to lower capital costs compared with TEG absorption. However, at higher levels of dehydration, the temperature needed to condense the desired amount of water results in high operating costs associated with the refrigeration cycle. It was determined that the water level remaining in the flue gas at which the two technologies are economically equivalent is 0.8 mol%. Above this value, cooling and condensing is selected, while below it TEG absorption is a better choice.

3.2.5 Post Separation Compression

For transportation through a pipeline network, it is necessary to compress the CO₂ product stream to 110 bar.⁶³ This compression is accomplished through a 5-stage compressor train with intercooling to compress the stream to 90 bar (Figure 3.1). At 90 bar, the gas is then cooled and condensed at 22°C.⁹¹ Once the CO₂ is condensed, the stream is pressurized to 110 bar using a pump.

3.2.6 Process Economics

All equations used for sizing the equipment, along with calculating the capital and operating costs of the P/VSA process, are retrieved from relevant sources and described in the Appendix B.^{88,89} For the adsorbent, the cost of the zeolites is assumed to be \$1/kg. For the two MOFs, we are using the estimated mass production cost based on the work of Liu et al.⁹² It is assumed that HKUST-1 would cost \$21/kg and Ni-MOF-74 would cost \$7/kg. For calculations of operating cost, it is assumed that the P/VSA unit runs for 8,000 hours per year and that the cost of electricity for the compressors, vacuum pumps, and liquid pumps is \$0.06/kWh. For calculation of the annualization factor, the lifetime of all capital equipment except for the adsorbents is assumed to be 20 years. For the adsorbent, the lifetime is assumed to be 5 years. The interest rate for both is assumed to be 10%.

In calculating the total cost of the P/VSA column, it is necessary to know the inner diameter and the wall thickness. The column is assumed to be made from carbon steel and to have a thickness of 0.015 m. The column diameter is determined by the feed rate, velocity of the inlet gas, and the number of columns used. The diameter is calculated as follows:²

$$D = \sqrt{\frac{4}{\pi} \left(\frac{10^5}{P_H} \frac{T_0}{273.15} 22.4 \right) \left(\frac{F \cdot t_c}{u_{ads} t_{ads} N} \right)} \quad (3.38)$$

where t_c is the cycle time of the process, which is the sum of the times of each step, u_{ads} is the velocity of the feed gas during the adsorption step, N is the number of columns and P_H is in Pa. In order to prevent the diameter of the column from becoming too large, the number of columns is set to 12 for the first stage and 4 for the second stage. The difference in number of columns for each stage is to maintain a roughly equivalent diameter between the two stages.

3.2.7 Solution Techniques

To solve the system of PDEs, we first discretize the spatial variables using the finite volume method (FVM)⁹³ using a weighted essentially non-oscillatory (WENO)⁹⁴ scheme, as this method has been shown in previous investigations to allow for the use of a smaller number of finite volumes without sacrificing the accuracy of the simulation.⁵¹ The equations are discretized into 10 volume elements and then the set of ordinary differential equations are solved using MATLAB's stiff solver ode15s.⁵³ The objectives of each case study are optimized using the nondominated sorting genetic algorithm (NSGA-II), as this allowed the full model to be used in the optimization algorithm and allows for parallel implementation.⁶¹ For the NSGA-II, the population is set to 10 times the number of decision variables, which are shown in Table 3.2. The algorithm is set to run for at least 60 generations or until no visible improvement is seen in the objective functions for 5 generations.

3.3. Results and Discussion

In order to achieve the final goal of minimizing the cost of the P/VSA system, three case studies are examined. First, we examine the maximum purity and recovery for each material using a single stage with dry flue gas. This is done in order to determine the single-stage capabilities of all the materials and from there to eliminate any materials not capable of achieving the desired purity and recovery in two stages. For the second case study, we minimize the total cost of a two-stage P/VSA system while maintaining the required purity and recovery of 90% each. For this case study, it is assumed that the flue gas is dehydrated completely prior to the P/VSA system. We do not consider the cost of the dehydration for this case study, since it will be equal for all materials. In the third case study, we minimize the cost of the entire superstructure including the dehydration, with the dehydration level as one of the optimization variables. For all three case studies, the bounds of the operating variables are listed in Table 3.2. For each case study, the genetic algorithm is run for each material separately.

3.3.1 Single-Stage Maximized Purity and Recovery

In the first study, the capabilities of each material in a single-stage Skarstrom cycle are tested. This results in 7 potential decision variables for optimization: the times for each of the four steps in the cycle, the length of the column, the adsorption pressure and the purge pressure. In order to reduce the number of decision variables, the pressurization steps and depressurization steps were allowed to run until the column was fully pressurized or depressurized, respectively. We also set the purge pressure *a priori*. Due to the highly nonlinear shape of the CO₂ isotherms for these materials, lower purge pressures are desirable to increase the working capacity of the adsorbents, resulting in higher purities and recoveries. However, there are practical limits on how low the pressure can be. Therefore, the purge pressure is set to a lower bound of 0.1 bar, since the purpose of this case study is to determine the capabilities of the materials in a practical system. This results in four decision variables for optimization for each of the materials.

The Pareto curves resulting from the optimization for the four materials are shown in Figure 3.6. It is immediately apparent that none of the four materials is capable of achieving the desired goal of 90% purity while recovering 90% of the CO₂ in a single-stage Skarstrom cycle. The best performing material, zeolite 13X, is only able to achieve a purity of 76% with a recovery close to 90%. It is also apparent that HKUST-1 is the worst performing material. While zeolite 5A and Ni-MOF-74 are able to achieve purities of 70% and 67%, respectively, HKUST-1 is unable to reach even 30% purity. When comparing the adsorbent isotherms in Figure 3.2, it is apparent that this low performance is due to the lower CO₂ uptake of HKUST-1 compared to the other materials. The internal column profiles of gas-phase CO₂ mole fraction, CO₂ and N₂ loading, and temperature for zeolite 13X and HKUST-1 for the highest purity points are shown in Figure 3.7. The optimized values of the decision variables are provided in the figure captions. When economics are not considered, it is optimal to pressurize the feed stream. For example, P_H is 4.46 bar for 13X and 4.2 bar for Ni-MOF-74. It should be noted that by lowering the vacuum pressure even further, it would be possible to achieve the 90% purity goal with the three best performing materials. However, due to issues with scaling up vacuum pumps capable of achieving these low pressures we set the lower bound for the vacuum pressure to be 0.1 bar.

From the mole fraction profiles in Figure 3.7, it is seen that zeolite 13X (solid lines) is able to achieve significantly higher purity of CO₂ after the depressurization step (red) compared to HKUST-1 (dashed lines). This difference in performance between zeolite 13X and HKUST-1 can be explained by the working capacities for both gases, which can be approximated as the change in the molar loading between the end of the adsorption step (green) and the end of the purge step (black) integrated across the bed. Using this approximation, the CO₂ and N₂ working capacities of zeolite 13X are 0.7 and 0.15 mol/kg, respectively. For HKUST-1, the CO₂ and N₂ working capacities are 0.22 and 0.45 mol/kg, respectively. It is also seen

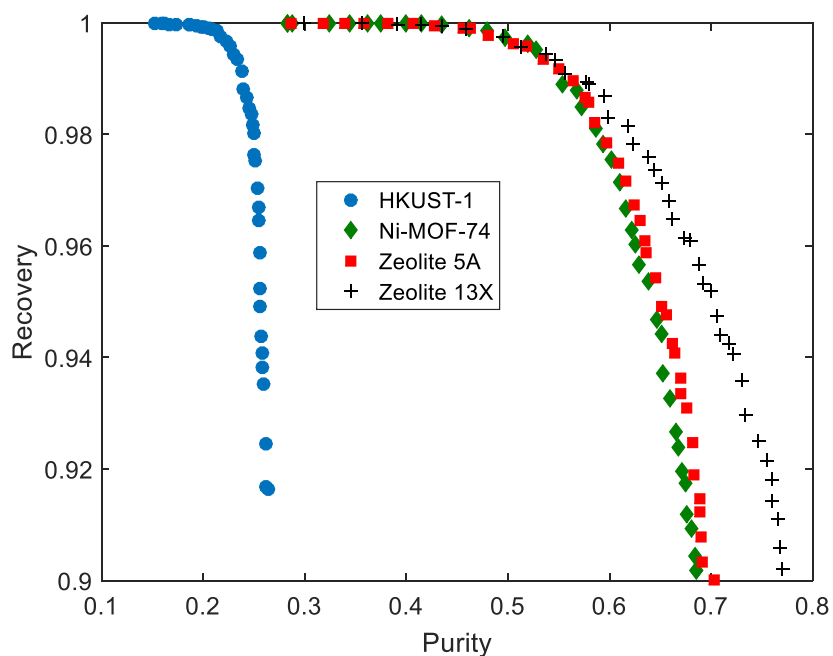


Figure 3.6. Pareto curves for multi-objective optimization of purity and recovery.

Table 3.2. Upper and lower bounds on the operating parameters for each case study.

Case Study	P_H (bar)	P_L (bar)	t_{ads} (s)	t_{purge} (s)	L (m)	Humidity Level (mol%)
1 stage maximum purity/ recovery	1-10	Fixed at 0.1	20-2000	20-2000	1-5	Fixed at 0%
2 stage dry flue gas minimum cost	1-10	0.1- 0.5	20-2000	20-2000	1-5	Fixed at 0%
2 stage wet flue gas minimum cost	1-10	0.1- 0.5	20-2000	20-2000	1-5	0.01 - 5.5 mol%

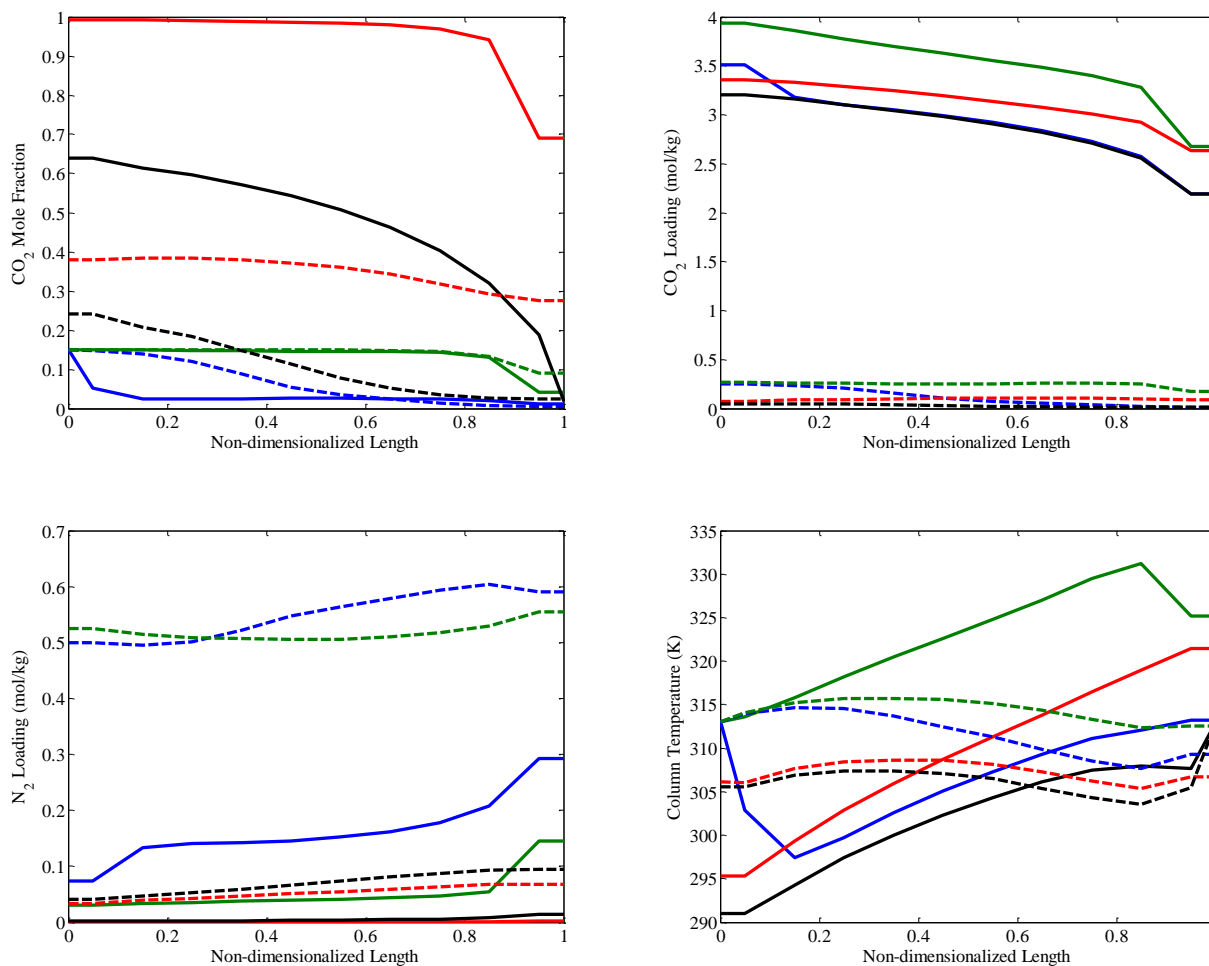


Figure 3.7. Internal column profiles for the highest purity shown in Figure 3.6. Solid lines correspond to Zeolite 13X, $P_H=4.46$ bar, $t_{ads}=794$ s, $t_{pur}=789$ s, $L=4.28$ m, cycle time=1945 s. Dashed lines correspond to HKUST-1, $P_H=1.5$ bar, $t_{ads}=680$ s, $t_{pur}=646$ s, $L=4.81$ m, cycle time=1642 s. For both materials, the profiles correspond to the bed at the end of each step with the colors corresponding to Pressurization (Blue), Adsorption (Green), Depressurization (Red), and Purge (Black).

Table 3.3. Minimum cost breakdown for a two-stage system with dry flue gas. Costs are in \$ million per year.

Material	Operating Costs	Annualized Capital Costs	Post-Separation Costs	Total Costs
Zeolite 13X	2.47	0.27	2.44	5.19
Zeolite 5A	2.68	0.25	2.47	5.40
Ni-MOF-74	3.16	0.86	2.42	6.44

Table 3.4. Optimal operating parameters for the first stage of the two-stage PSA system with dry flue gas. The cycle time is the sum of the times required for each step.

Material	Adsorption Pressure (bar)	Purge Pressure (bar)	Adsorption Time (s)	Purge Time (s)	Length (m)	Cycle Time (s)
Zeolite 13X	1.00	0.10	726	382	1.73	1173
Zeolite 5A	1.27	0.10	521	291	1.69	878
Ni-MOF-74	1.36	0.10	657	418	1.50	1145

Table 3.5. Optimal operating parameters for the second stage of the two-stage PSA system with dry flue gas. The cycle time is the sum of the times required for each step.

Material	Adsorption Pressure (bar)	Purge Pressure (bar)	Adsorption Time (s)	Purge Time (s)	Length (m)	Cycle Time (s)
Zeolite 13X	1.26	0.10	589	249	3.81	1120
Zeolite 5A	1.30	0.10	664	449	4.95	1520
Ni-MOF-74	2.66	0.10	330	215	3.22	939

that a significant change in temperature occurs in the column during the P/VSA cycle. Between the end of the adsorption step and the end of the purge step, the average temperature in the column decreases by 20°C. This shift in the temperature helps to explain why the working capacity achieved during the P/VSA cycle is smaller than working capacities calculated simply from the isotherms of the material. In addition, due to a temperature gradient developed in the column, the difference between the maximum and minimum temperature experienced throughout the cycle is around 40°C. Since it will be difficult for HKUST-1 to achieve the purity and recovery goals of 90% each, HKUST-1 is not considered in the other case studies.

3.3.2 Dry Flue Gas, Two-Stage Minimized Cost

Since one stage cannot meet the desired purity and recovery, a two-stage P/VSA process is constructed and the system is optimized for minimum total cost with the minimum purity and recovery as constraints. In this case study, the flue gas is assumed to be completely dehydrated prior to the separation process. This allows us to compare the performance of each of the adsorbents under dry conditions initially. Since a two-stage configuration is used and the purge pressure is allowed to vary in order to reduce operating costs of the vacuum pump, the number of decision variables increases to ten for this case study.

The minimum cost from the optimization for each of the materials is shown in Table 3.3. The optimal operating parameters are provided in Tables 3.4 and 3.5. The adsorption pressures are notably lower than in the previous section, now that the cost of pressurization is taken into account. However, the purge pressures all optimize to 0.1 bar, indicating that the economic cost of the vacuum pumps and their operation is justified by the improved performance at this low desorption pressure.

Based on the total costs, zeolite 13X is the best performing material of the three studied. The total cost for zeolite 13X is \$5.19 million per year, corresponding to a cost of \$32.1 per ton of CO₂ captured. It can be seen that the majority of the costs for the process are associated with the operating costs (compressor and vacuum pump costs for the P/VSA process) and the post-separation compression costs (which encompass both capital and operating costs for the 5-stage compressor train, heat exchangers and pumps).

The annualized capital costs account for only approximately 5% of the overall costs of the system. Ni-MOF-74 has the highest costs, costing \$1.2 million dollars more per year than zeolite 13X. This is largely due to higher operating costs associated with higher adsorption pressures in both the first and second stages, as shown in Table 3.4 and Table 3.5. However, Ni-MOF-74 also has significantly higher capital costs than the two zeolites, because the MOF itself is more expensive to produce than the two zeolites. It should be noted that the cost of the MOF is one of the most uncertain parameters in the model.

3.3.3 Wet Flue Gas, Two-Stage Minimized Cost

Before performing an optimization of a two-stage system with wet flue gas, we compared results for a single stage with wet and dry flue gas to determine the magnitude of the effect that water has on the CO₂ purity and recovery. A single-stage Skarstrom cycle is simulated with zeolite 13X as the adsorbent and 5.5 mol% water in the feed stream under the following operating parameters: $P_H = 1$ bar, $P_L = 0.1$ bar, $t_{ads} = 726$ s, $t_{pur} = 382$ s, $L = 1.73$ m. Under these conditions, a purity of 52.1% (on a dry basis) is achieved with a recovery of 93.1%. This is compared to the dry flue gas at the same operating parameters, where a purity of 49.7% and a recovery of 97.5 % is achieved. The internal column profiles for the dry and wet flue gas conditions are shown in Figure 3.8. It can be seen that in the presence of water the CO₂ front travels further into the bed than under dry flue gas conditions. This is because water reduces the adsorption capacity of the first section of the bed. This results in more CO₂ being lost during the adsorption step and a decrease in the overall recovery. The presence of water also decreases the amount of N₂ in the column, resulting in increased purity for the wet flue gas conditions. Based on these results, it can be concluded that complete dehydration of the flue gas before the P/VSA cycle is unnecessary (at least for some adsorbents). For 13X, the water front stays concentrated at the entrance of the bed, and the first section of the bed acts as a desiccant.

Next, the operating parameters of a two-stage Skarstrom cycle are optimized for each material in the presence of water. For this case study, 11 decision variables are used: the ten decision variables

mentioned in the previous case study along with the water level in the gas stream entering the P/VSA system. This results in a population of 110 for the optimization run, which is run for at least 60 generations for each material. Since water is a heavy product, more readily adsorbed by all the adsorbents, the water that is adsorbed in the first stage of the system also enters the second stage. Therefore, it is assumed that the humidity level in the feed entering the first stage is also the humidity level entering the second stage.

From the optimization, the minimum cost for each material is shown in Table 3.6, and the corresponding operating parameters are given in Tables 3.7 and 3.8. Zeolite 13X and 5A have the lowest total costs of \$5.52 million per year and \$5.53 million per year respectively, or ~\$34.1 per ton of CO₂. While zeolite 13X has the lowest operating cost of the three materials, it has higher capital costs than zeolite 5A. One interesting result of the optimization is that all of the materials required little to no dehydration before the P/VSA columns. The water levels for all of the adsorbents are seen in Table 3.7 and Table 3.8. All of the materials were able to accomplish this by using the first section of the column as a desiccant, dehydrating the flue gas in the process, and having the second section of the column separate the CO₂ from the N₂. This is seen in the column profiles of zeolite 13X in Figures 3.9, 3.10. The water front is seen in the reduced CO₂ loading at the front of the bed in the first and second stage column profiles of zeolite 13X shown in Figures 3.9 and 3.10. Note that in all cases, the length of the column that is affected by water is less than the length of one of the finite volumes. In order to account for this, the water penalty factor is adjusted so the average decrease in the loading over the entire finite volume is equal to the penalty factor over the length of the column affected. For zeolite 13X, the water front penetrated the first 0.15 m of the bed in the first stage, and the first 0.1 m of the second stage. For the zeolite 5A, the water front penetrated 0.08 m and 0.03 m for the first and second stages, respectively. Finally, for Ni-MOF-74, the water front penetrated 0.12 m and 0.07 m for the first and second stages, respectively.

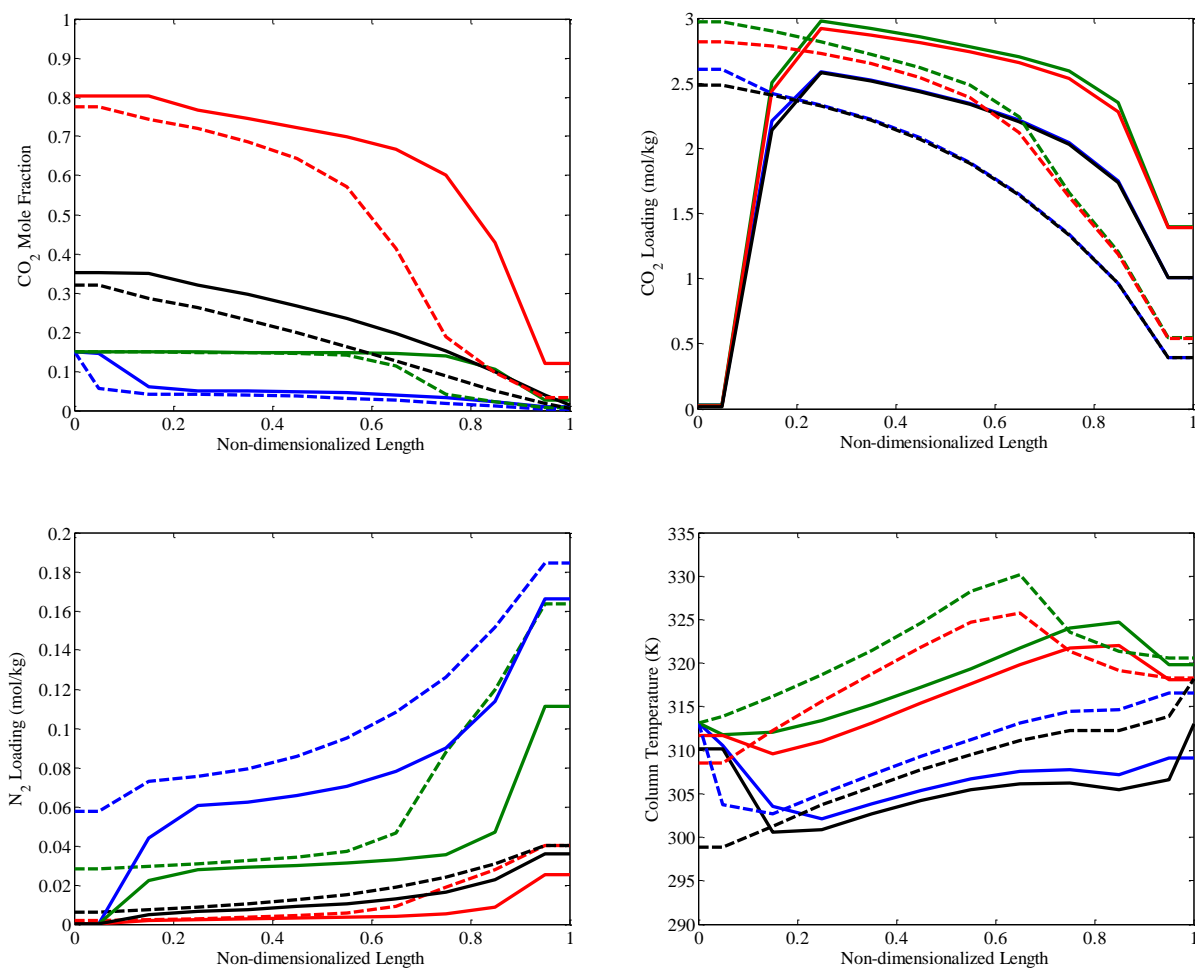


Figure 3.8. Internal column profiles comparing dry (dashed lines) and wet (solid lines) flue gas using a single stage with zeolite 13X under the same operating parameters. The profiles correspond to the bed at the end of each step with the colors corresponding to Pressurization (Blue), Adsorption (Green), Depressurization (Red), and Purge (Black).

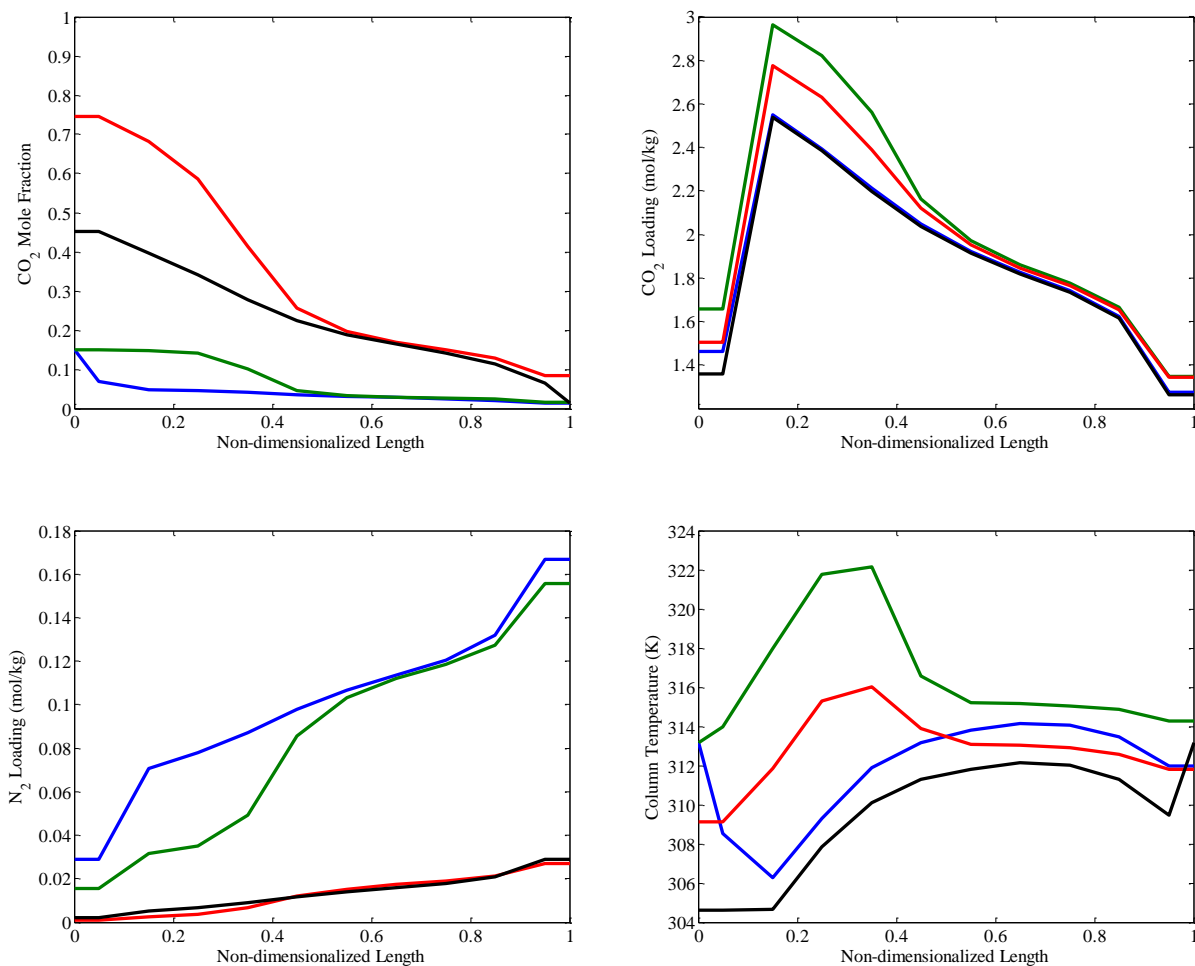


Figure 3.9. Internal column profiles of the 1st stage of a two-stage P/VSA system with wet flue gas using zeolite 13X. The profiles correspond to the bed at the end of each step with the colors corresponding to Pressurization (Blue), Adsorption (Green), Depressurization (Red), and Purge (Black).

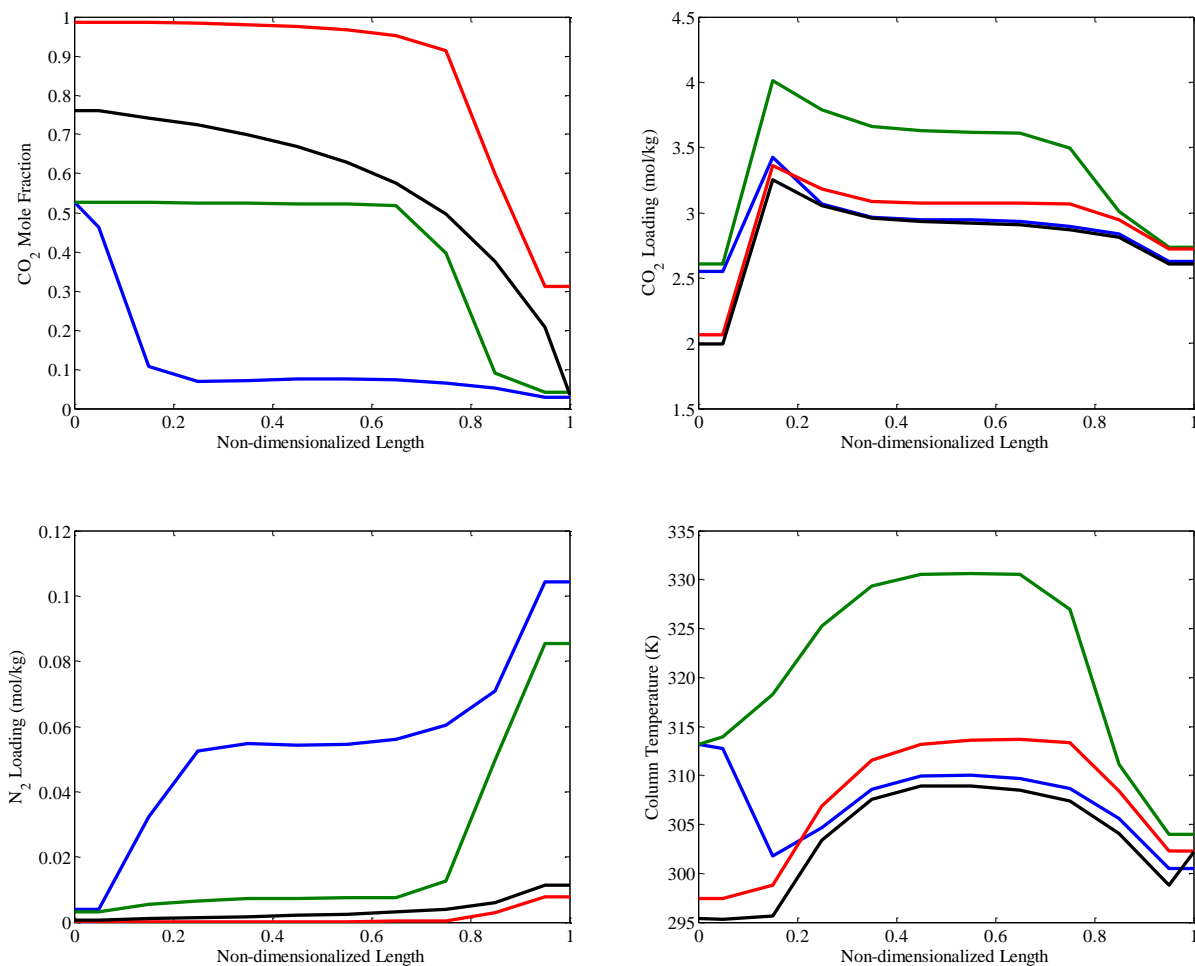


Figure 3.10. Internal column profiles of the 2nd stage of a two-stage P/VSA system like Fig. 3.9 with wet flue gas using zeolite 13X. The profiles correspond to the bed at the end of each step with the colors corresponding to Pressurization (Blue), Adsorption (Green), Depressurization (Red), and Purge (Black).

Table 3.6. Minimum cost breakdown for a 2-stage system with wet flue gas. Costs are in \$ million per year

Material	Operating Costs	Capital Costs	Post-Separation Costs	Dehydration Costs	Total Costs	Dehydration Technology
Zeolite 13X	2.66	0.39	2.46	0	5.52	None
Zeolite 5A	2.83	0.24	2.46	0	5.53	None
Ni-MOF-74	3.49	0.83	2.46	0.084	6.86	C&C

Table 3.7. Optimal operating parameters for the first stage of the two-stage PSA system with wet flue gas. The cycle time is the sum of the times required for each step.

Material	Adsorption Pressure (bar)	Purge Pressure (bar)	Adsorption Time (s)	Purge Time (s)	Length (m)	Humidity Level (%)	Cycle Time (s)
Zeolite 13X	1.21	0.10	676	263	3.23	5.50	1053
Zeolite 5A	1.48	0.10	562	335	2.10	5.50	975
Ni-MOF-74	1.81	0.10	709	553	1.90	4.34	1354

Table 3.8. Optimal operating parameters for the second stage of the two-stage PSA system with wet flue gas. The cycle time is the sum of the times required for each step.

Material	Adsorption Pressure (bar)	Purge Pressure (bar)	Adsorption Time (s)	Purge Time (s)	Length (m)	Humidity Level (%)	Cycle Time (s)
Zeolite 13X	1.71	0.10	370	257	3.56	5.50	883
Zeolite 5A	1.44	0.10	307	246	3.57	5.50	788
Ni-MOF-74	2.90	0.14	300	154	3.90	4.34	773

3.4. Conclusion

A robust simulator was developed that is capable of modeling a P/VSA process accounting for heat effects, pressure drops, and non-linear isotherms. It uses a finite volume scheme coupled with a WENO scheme for quickly and accurately solving the system of PDEs. With this simulation, a genetic algorithm was used to optimize the operating parameters for CO₂ capture, allowing us to investigate the performance of three different materials with and without the presence of water in the flue gas stream. The model also includes the use of absorption or cooling and condensation to partially dehydrate the flue gas before it enters the P/VSA system. The results of this study indicate that under dry flue gas conditions, zeolite 13X is the best performing material with a cost of CO₂ capture of \$32.1 per ton of CO₂. Under the wet flue gas conditions, both zeolite 13X and zeolite 5A performed equally well with a cost of CO₂ capture of ~\$34.1 per ton of CO₂. It is also seen that all of the adsorbents tested used the first section of the P/VSA column as a desiccant to dehydrate the flue gas, presumably due to the adsorbents strong interactions with the water. This results in little to no dehydration prior to the adsorption column being needed. This work emphasizes that the level of water removed before a P/VSA cycle for CO₂ capture is an important variable and some adsorbent materials could even operate with minimum dehydration of the flue gas. Finally, it is also seen that a two-stage Skarstrom cycle is a valid approach for capturing CO₂ with 90% recovery and 90% purity. Future work should consider other cycles, which may accomplish this separation in a single stage.

Chapter 4: Development of a General Evaluation Metric for Rapid Screening of Adsorbent Materials for Post-Combustion CO₂ Capture

4.1. Introduction

The atmospheric CO₂ concentration is escalating rapidly and is thought to be responsible for unusual climate changes observed around the globe.⁹⁵ Most scenarios for limiting global temperature increases to less than 2°C include a near-term role for carbon capture technologies,⁹⁶ such as amine scrubbing, before more permanent, renewable energy technologies become economically viable. In amine scrubbing, CO₂ is absorbed by an aqueous amine solution, followed by stripping of the captured CO₂ out of the liquid phase by heating. However, there is a significant energy penalty associated with heating the aqueous amine. Because of this, alternative technologies, such as adsorption-based technology, are proposed.

Adsorption-based technology is attractive due to its low cost of regeneration compared with amine scrubbing.⁹⁷ Adsorption-based technologies can be divided into three main processes differing in how the adsorbent is regenerated: (1) pressure swing adsorption (PSA), (2) temperature swing adsorption (TSA), and (3) a combination of both PSA and TSA. The performance of these processes is highly dependent on the adsorbent material, and the development of improved adsorbents is arguably the main challenge in realizing industrial-scale deployment of adsorption-based CO₂ capture technology.

Several adsorbent materials, such as activated carbons and zeolites, have been evaluated in PSA processes for CO₂ capture in recent years.^{40,98} In addition, a new class of porous materials, metal-organic frameworks (MOFs),^{99,100} have been gaining interest because MOFs generally have higher CO₂ uptake^{31,101} than traditional adsorbent materials and can, in some instances, maintain their high uptake in the presence of water.^{102–104} However, with over 5,000 MOFs already synthesized,³⁸ and the potential to synthesize

countless additional MOF structures, it is difficult to quickly find the best MOFs for CO₂ capture or other separation challenges.

A key challenge in screening adsorbents for CO₂ capture is choosing performance metrics that can be calculated at the early stages of materials screening. Some minimum basic information that can be reasonably obtained for a new material is the uptake of CO₂ and N₂ at relevant conditions, either from experiment or molecular simulation. With this information (and some additional assumptions, for example about the kinetics of adsorption), one option would be to perform macroscopic process simulation of a PSA process to rank materials based on the cost of CO₂ capture. However, carrying out such simulations, including optimization of the operating parameters, in a high-throughput manner is currently not feasible for tens of thousands of MOF structures and requires expertise not common to researchers synthesizing new MOFs.

An alternative approach is to develop an evaluation metric that can accurately capture the process-level information to rank materials based on the features of equilibrium isotherm data. Simple examples of such metrics include the working capacity and the selectivity. However, one often finds that materials with high working capacity have low selectivity or vice versa. Thus, researchers have tried to develop metrics that incorporate both the selectivity and the working capacity with some weighting. Prominent examples are shown in Table 4.1. These metrics require single-component adsorption isotherms and typically estimate the mixture thermodynamics using the multi-component Langmuir model or Ideal Adsorbed Solution Theory (IAST). One of them, the Adsorbent Performance Indicator,¹⁰⁵ also requires the CO₂ enthalpy of adsorption, to account for the ease of regeneration of the adsorbent materials. These metrics have been proposed over the years to rank different adsorbents without carrying out full-scale process simulations, but are largely based on physical intuition and have not been thoroughly tested in the context of process modelling and simulation results.

More recently, efforts have focused on the development of performance measures based on simplified process models of PSA or TSA processes as proposed by Lin and co-workers,³² Krishna,¹⁰⁶ Braun and co-workers,¹⁰⁷ and Huck and co-workers.¹⁰⁸ These models are simple and can be applied for large-scale screening but are limited in terms of their applicability for ranking adsorbents on their expected performance because the metrics do not directly take into account whether the material meets the specified purity and recovery requirements.

Table 4.1. Definitions of the various performance metrics found in the literature that are evaluated in this study. Subscripts 1 and 2 represent components 1 and component 2, where 1 is the more strongly adsorbing species

Adsorbent Metric	Definition	Reference
Henry Selectivity	$\alpha_0 = \frac{K_{H,1}}{K_{H,2}}$	(Knaebel, 1999) ¹⁰⁹
PSA Sorbent Selection Parameter	$S = \alpha_{1,2} \frac{WC_1}{WC_2}$	(Rege and Yang, 2001) ¹¹⁰
Adsorbent Performance Indicator	$API = \frac{(\alpha_{1,2} - 1)WC_1}{ \Delta H_{ads,1} }$	(Wiersum et al., 2013) ¹⁰⁵
Adsorbent Figure of Merit	$AFM_1 = WC_1 \frac{\alpha_1^2}{\alpha_2}$	(Notaro, 1998) ¹¹¹
Adsorbent Figure of Merit	$AFM_2 = \frac{WC_1}{WC_2} \frac{\alpha_1^2}{\alpha_2}$	(Rege and Yang, 2001) ¹¹⁰
Separation Factor	$SF = \frac{WC_1 y_2}{WC_2 y_1}$	(Pirngruber et al., 2012) ¹¹²

An emerging approach in the field is to directly integrate process modelling into adsorbent materials screening, to find correlations between material properties and process objectives. An example of such investigations is the work of Maring and Webley where they found a moderate correlation between the cost of CO₂ capture and the heat of adsorption of CO₂.¹¹³ Rajagopalan and co-workers evaluated the capabilities of metrics to screen potential adsorbents by determining the performance (CO₂ purity of the final product, energy requirements, and productivity) of four adsorbents (Mg-MOF-74, UTSA-16, Zeolite 13X and an activated carbon) along with three hypothetical adsorbents using a four step PSA cycle with light product pressurization. After comparing the performance results of the different adsorbents along with the calculated metric values, they found that the working capacity of N₂ was the best predictor of the process performance of the different adsorbents.¹¹⁴ However, these investigations evaluated only a handful of materials, and the conclusions drawn from the work may not be generalized in predicting the performance of other adsorbent materials. One exception to this is the work by Khurana and Farooq,¹¹⁵ who developed and validated a neural network model for 74 adsorbent materials to predict if an adsorbent material could achieve certain purity and recovery requirements.

In this contribution, we examined over 2,900 MOFs for post-combustion CO₂ capture to identify the best adsorbent materials with the lowest cost of CO₂ capture while meeting the required purity and recovery targets. Performing PSA simulations on 2,900 MOFs would take considerable computational resources. Since many of these materials may not be good candidates for post-combustion CO₂ capture, we first carried out PSA simulations on generic adsorbent materials to find the optimal ranges of the internal energy of adsorption for CO₂ and N₂, along with the adsorbent density, to achieve the desired goals for CO₂ capture. The optimal ranges were coupled with the cost of metals in the MOFs to reduce the MOF dataset to 369 candidates. Among these 369 candidate MOFs, we found 190 were able to achieve the desired CO₂ purity and recovery goals of 90% with the chosen PSA cycle. For these 190 materials, we carried out full-scale process simulations and economic analyses to calculate the CO₂ capture cost for each MOF. Using the data

generated from process simulations and economic analyses, we developed a general evaluation metric (GEM) that can be used to identify high-performing adsorbent materials for post-combustion CO₂ capture. We compared this metric with other evaluation metrics from the literature using the Spearman correlation coefficient and found that the predicted cost of CO₂ capture and the GEM correlates better than any other metric reported in the literature.

4.2. Computational Methods

4.2.1 Widom Particle Insertions

Widom particle insertion calculations were carried out at 298 K for all structures in the CoRE MOF 2014 DDEC database¹¹⁶ using the RASPA code to predict the internal energy change upon adsorption in the infinite-dilution limit.¹¹⁷ 5,000 configurational-biased insertions of CO₂ and N₂ were used for each structure. The Lennard-Jones (LJ) plus Coulomb potential was used to model the non-bonded interactions between MOF atoms and CO₂ and N₂ atoms (also for the interactions among the guest molecules for GCMC simulations below):

$$V_{ij} = 4\epsilon_{ij} \left[\left(\frac{\sigma_{ij}}{r_{ij}} \right)^{12} - \left(\frac{\sigma_{ij}}{r_{ij}} \right)^6 \right] + \frac{q_i q_j}{4\pi\epsilon_0 r_{ij}} \quad (4.1)$$

Here i and j are the interacting atoms; r_{ij} is the distance between atoms i and j ; q_i is the partial charge of atom i ; ϵ and σ are the LJ parameters; and ϵ_0 is the vacuum permittivity constant ($8.854187817 \times 10^{-12}$ C²/(J-m)). For the MOF atoms, LJ parameters were taken from the Universal Force Field (UFF),¹¹⁸ and partial charges were obtained from the DDEC results of Nazarian et al.¹¹⁶ The Transferable Potentials for Phase Equilibria (TraPPE)¹¹⁹ were used to model the adsorbate molecules. LJ parameters for unlike atoms were approximated with the Lorentz-Berthelot mixing rules, and LJ potentials beyond 12.8 Å were truncated without applying tail corrections. All simulations were performed with an $N \times N \times N$ simulation box to satisfy the minimum image convention with respect to the 12.8 Å cutoff. The Ewald summation technique was used to calculate Coulombic interactions, with alpha and kvec parameters using 10^{-6}

precision. Throughout the simulation, the MOF atoms were held fixed at their crystallographic positions (as reported in CoRE MOF 2014 DDEC database).¹¹⁶

4.2.2 Grand Canonical Monte Carlo (GCMC) simulations[†]

GCMC simulations were carried out to compute the single- and multi-component adsorption isotherms for CO₂ and N₂ at 0.01 - 10 bar and 298 K in 369 MOFs. The same force field was used as described above for the Widom insertion calculations, and again the RASPA code was used. Isotherms were generated by performing the simulations starting at the lowest pressure and using the final configuration from each pressure as the initial configuration for the next simulation. This procedure helps the system reach equilibrium faster. Mixture isotherms were calculated for a 15:85 gas-phase mixture of CO₂ and N₂. The Peng-Robinson equation of state was used to compute the gas phase fugacity values for CO₂ and N₂, which are needed as inputs to the simulation. The Metropolis-Hasting algorithm was used to sample the phase space for specified fugacities and temperature. Both pure and mixture GCMC simulations used 5,000 equilibration cycles followed by 5,000 production cycles to collect ensemble averages of the system properties. In a cycle, N Monte Carlo moves are performed, where N is the maximum between 20 and the number of adsorbate molecules in the simulation box at the beginning of the cycle. Insertion, deletion, translation, and rotation moves were used with equal probabilities. For mixture simulations, identity change moves were also used in conjunction with the other Monte Carlo moves with equal probabilities.

4.2.3 Equilibrium Isotherm Fitting

To perform process level simulations, it is necessary to have an analytical expression or other rapid method to calculate the CO₂ and N₂ molar loadings at various pressures, gas-phase concentrations, and temperatures. In this work, the pure-component CO₂ and N₂ isotherms from the GCMC simulations were fitted to dual and single-site Langmuir models, respectively. For the CO₂ isotherm, we assume that the

[†] All GCMC simulations were performed by Dr. Yongchul Chung.

stronger site, designated as site 1, only adsorbs CO₂, while CO₂ and N₂ compete on the weaker site, designated as site 2:

$$q_{CO_2} = \frac{q_{sat,CO_2,1} B_{CO_2,1} p_{CO_2}}{1 + B_{CO_2,1} p_{CO_2}} + \frac{q_{sat,CO_2,2} B_{CO_2,2} p_{CO_2}}{1 + B_{CO_2,2} p_{CO_2} + B_{N_2,2} p_{N_2}} \quad (4.2)$$

$$q_{N_2} = \frac{q_{sat,N_2,2} B_{N_2,2} p_{N_2}}{1 + B_{CO_2,2} p_{CO_2} + B_{N_2,2} p_{N_2}} \quad (4.3)$$

Here $q_{sat,i,s}$ and $B_{i,s}$ are the saturation loading and isotherm parameter of component i on site s , respectively.

In order to maintain thermodynamic consistency,¹²⁰ we set the saturation loading of site 2 equal for N₂ and CO₂. The isotherms were then simultaneously fitted to minimize the absolute square error. After all of the parameters were fitted, we used an Arrhenius-type equation to account for the temperature dependence of the CO₂ and N₂ loading,

$$B_{i,s} = b_{0,i,s} \exp\left[\frac{\Delta U_i}{RT}\right] \quad (4.4)$$

where ΔU_i is the internal energy change upon adsorption in the infinite-dilution limit calculated from the Widom particle insertion method. For simplicity, we will sometimes call ΔU_i the “heat of adsorption” below. To test the accuracy of the isotherm predictions, we compared the results against multi-component GCMC simulations of 10 random MOFs from the CoRE MOF database. For the 10 random MOFs, the mean unsigned errors between the multicomponent Langmuir model and the GCMC data are 0.049 and 0.022 mol/kg for CO₂ and N₂, respectively.

4.2.4 Process Simulation, Optimization, and Economic Analysis

Process simulation, optimization, and economic analysis were carried out for 369 MOFs to evaluate their CO₂ capture performance. The PSA model developed in the previous chapter was used as a starting point to develop a four-step Fractionated Vacuum Pressure Swing Adsorption (FVPSA) cycle (see Figure

4.1).^{2,51,56} We note that in order to accelerate the simulation time, we assume that the column behaves adiabatically to reduce the energy balance equations.

In this work, we used the four-step FVPSA cycle, as shown in Figure 4.1. This cycle consists of the following steps: (1) Pressurization, (2) Feed, (3) Co-Current Depressurization, and (4) Counter-Current Depressurization. The bed begins the Pressurization step at the low pressure (P_L) and is pressurized up to the feed pressure (P_H) using the flue gas during this step. Once the bed is fully pressurized, the top of the column is opened, and the flue gas is fed through, which is the beginning of the “Feed” step. During this Feed step, the CO_2 preferentially adsorbs in the MOFs, concentrating the CO_2 in the column, while N_2 flows out the top. After a predetermined amount of time, the bottom inlet of the column is closed, and vacuum is pulled from the top of the column, dropping the pressure to an intermediate value (P_I), which is the start of the “Co-Current Depressurization” step. This step is used to further remove N_2 from the column, increasing the purity of the final CO_2 product. Once P_I has been reached, the top of the column is closed, and the pressure at the bottom of the column is dropped back to P_L . It is during this final step, the Counter-Current Depressurization step, that the CO_2 is collected. The cost of the overall process is calculated using the economic equations provided in Appendix B. The process for each MOF is then optimized using the non-dominated sorting genetic algorithm (NSGA-II)⁶¹ and the following optimization variables: feed pressure (P_H), intermediate pressure (P_I), column length (L), and time of the feed step (t_{feed}). The lower pressure, P_L , is set at 0.1 bar. Additional details are available in Appendix B. Initial optimizations were done for 369 MOFs to determine the maximum CO_2 purity that could be obtained while recovering 90% of the CO_2 . And for those 190 MOFs that could achieve 90% CO_2 purity, a second optimization was done to minimize the overall cost, with constraints of 90% CO_2 purity and 90% recovery of CO_2 . We note that the reported cost in this chapter only includes the capital and operating costs of the FVPSA cycle. Dehydration and post-combustion compression costs are not included.

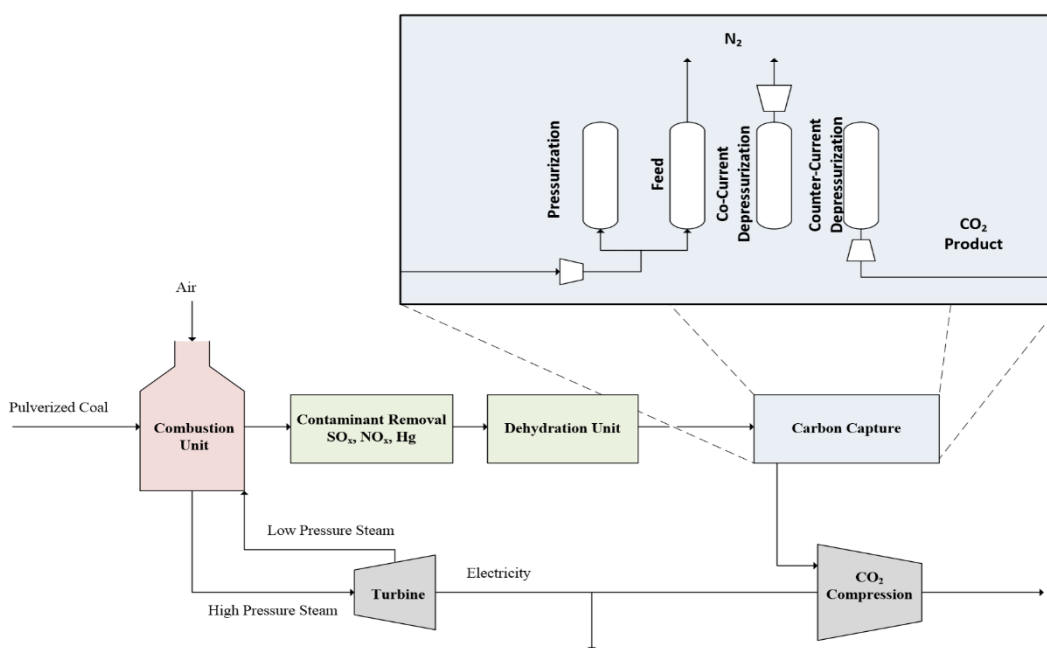


Figure 4.1. Post-combustion carbon capture schematic utilizing the fractionated vacuum pressure swing adsorption (FVPSA) cycle (top insert) for capturing the CO₂. Note that we have considered only the carbon capture portion of the process in this work and have not included the compression costs of the CO₂ product.

4.3. Results and Discussion

4.3.1 Development of a Pre-Screening Heuristic

Performing process-level optimization on the 5,109 materials in the CoRE MOF database would be tremendously time-consuming. In addition, many materials are unlikely to meet the given CO₂ purity and recovery constraints for a given PSA cycle. We, therefore, sought to use initial process-level modelling to develop heuristics that could be used in a pre-screening stage to reduce the number of materials that would need to be evaluated using process-level optimization.

To do this, we created a “generic” adsorbent and modelled it at the process simulation level to study the effect of the heats of adsorption of CO₂ and N₂ and the density of the adsorbent material on the separation performance. The adsorption properties of the generic adsorbent are described by the dual-site competitive

Langmuir model, and we varied the heats of adsorption for CO₂ and N₂ and the adsorbent density to study the effect of these variables on system performance.

First, we fixed the density of adsorbent at 1.1 g/cm³, and carried out process simulation and optimization to maximize the CO₂ purity (subject to the 90% recovery constraint) with different values of the heats of adsorption for CO₂ and N₂. Figure 4.2a shows that the heat of adsorption for N₂ has a large effect on the maximum attainable CO₂ purity. In particular, if the magnitude of the N₂ heat of adsorption is above 16 kJ/mol, the adsorbent is unable to achieve a CO₂ purity of 90%. In addition, the difference between the N₂ and CO₂ heats of adsorption plays a significant role, and there appears to be an optimal range of this difference around 20 – 30 kJ/mol when the heat of adsorption for N₂ is 10 kJ/mol. The peak occurs because, at high CO₂ heats of adsorption, the amount of CO₂ adsorbed at desorption conditions is too high, reducing the working capacity of CO₂ for the material. These results are consistent with previous investigations.¹²¹

Next, we fixed the CO₂ and N₂ internal energies of adsorption to –32 kJ/mol and –10 kJ/mol, respectively, and carried out process simulation and optimization to minimize the energy consumption of the process for different values of the adsorbent density. Figure 4.2b shows that the required energy for capturing CO₂ at 90% purity and 90% recovery is high for adsorbent materials with low density. (Note that, for this study, the saturation loading and the density of the material were treated as independent of each other to determine the effects of the density only.) As the density of the adsorbent material increases, the energy required to capture CO₂ decreases until it levels off around 0.9 g/cm³. Since heat is generated during the PSA adsorption step and consumed during the desorption step, a dense MOF material helps to moderate the temperature changes throughout the PSA cycle by acting as a “heat sink.” Indeed, we find that, at low adsorbent density (<0.9 g/cm³), the temperature variations in the column during the PSA cycle are larger, resulting in a decrease in performance (higher energy requirements for CO₂ capture) due to lower CO₂ loadings at higher temperatures. As the density of the adsorbent increases, the column behaves more isothermally, which improves the working capacity of the column, allowing for smaller pressure ratios

between the high and low pressure to be used to achieve the desired CO₂ working capacity. Since the low pressure is fixed in these simulations to 0.1 bar, this results in lower feed pressures being selected.

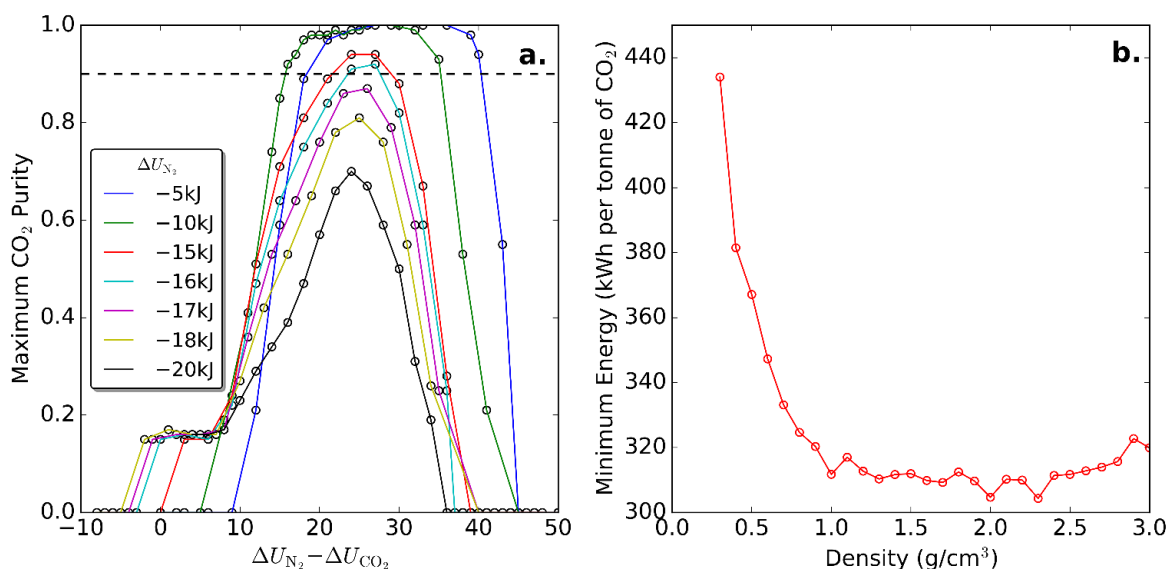


Figure 4.2. a. Optimal heats of adsorption analysis for the FVPSA cycle using a generic adsorbent material with density of 1.1 g/cm³. Each point represents the highest CO₂ purity that could be achieved while recovering 90% of the CO₂ product. Each line represents a different N₂ internal energy of adsorption. The dashed horizontal line is the DOE target for a CO₂ purity of 90%; b. Minimum energy required to capture a tonne of CO₂ as a function of sorbent density for a generic adsorbent with CO₂ internal energy of adsorption of -32 kJ/mol and N₂ internal energy of adsorption of -10 kJ/mol. The generic adsorbent material in both studies has a single site Langmuir isotherm for CO₂ and N₂, with saturation loading of 10 mol/kg, and an Arrhenius equation pre-exponential parameter of 10⁻¹⁰ Pa⁻¹ and 10⁻⁰⁹ Pa⁻¹ for CO₂ and N₂ respectively.

Based on these studies with a generic adsorbent, we propose the following pre-screening heuristics. Adsorbents should be eliminated from consideration if (1) the N₂ heat of adsorption is less than -16 kJ/mol, (2) the magnitude of the difference in the heats of adsorption for CO₂ and N₂ is greater than 35 kJ/mol or less than 15 kJ/mol, or (3) the adsorbent density is < 0.9 g/cm³. While these heuristics were developed for the FVPSA cycle, they may also apply to other cycles, and testing this hypothesis would be an interesting topic for future study.

4.3.2 MOF Screening

We started our MOF screening with the 5,109 structures in the CoRE MOF database. A flow diagram for the reduction of MOFs under consideration for economic evaluation is shown in Figure 4.3. Due to the importance of accurately modelling electrostatic interactions between the MOF and CO₂, we removed MOFs without DDEC partial atomic charges, leaving 2,902 structures. Next, we removed any MOFs where the cost of the metal nodes is prohibitively expensive, because any adsorbent used for CO₂ capture application will need to be produced on a large scale, and any MOF containing expensive metal nodes will significantly increase the capital cost of such a system. We estimated the cost of the metal for each MOF on a mass basis and removed any MOFs where the cost of metal is greater than \$40 per kg.

At this point, we had 800 MOFs. Additional structures were eliminated based on the heuristics developed above. Thus, we filtered out (1) MOFs with N₂ heats of adsorption less than -16 kJ/mol; (2) MOFs where the magnitude of the difference in the heats of adsorption between CO₂ and N₂ is > 35 kJ/mol or < 15 kJ/mol; and (3) MOFs with density < 0.9 g/cm³. We note that in Figure 4.3, the criteria listed are the criteria for keeping the MOFs and not for removing them.

Following this procedure, we were left with 390 MOFs, for which we carried out GCMC simulations at post-combustion CO₂ capture conditions. Based on the results from the molecular simulations, we removed an additional 21 MOFs that had very low CO₂ uptake ($q_{CO_2} < 0.1$ mol/kg at a CO₂ pressure of 10 bar). With this set of 369 MOFs, process simulation and optimization were performed to determine the maximum CO₂ purity that could be achieved while recovering 90% of the CO₂. Based on the results from these process

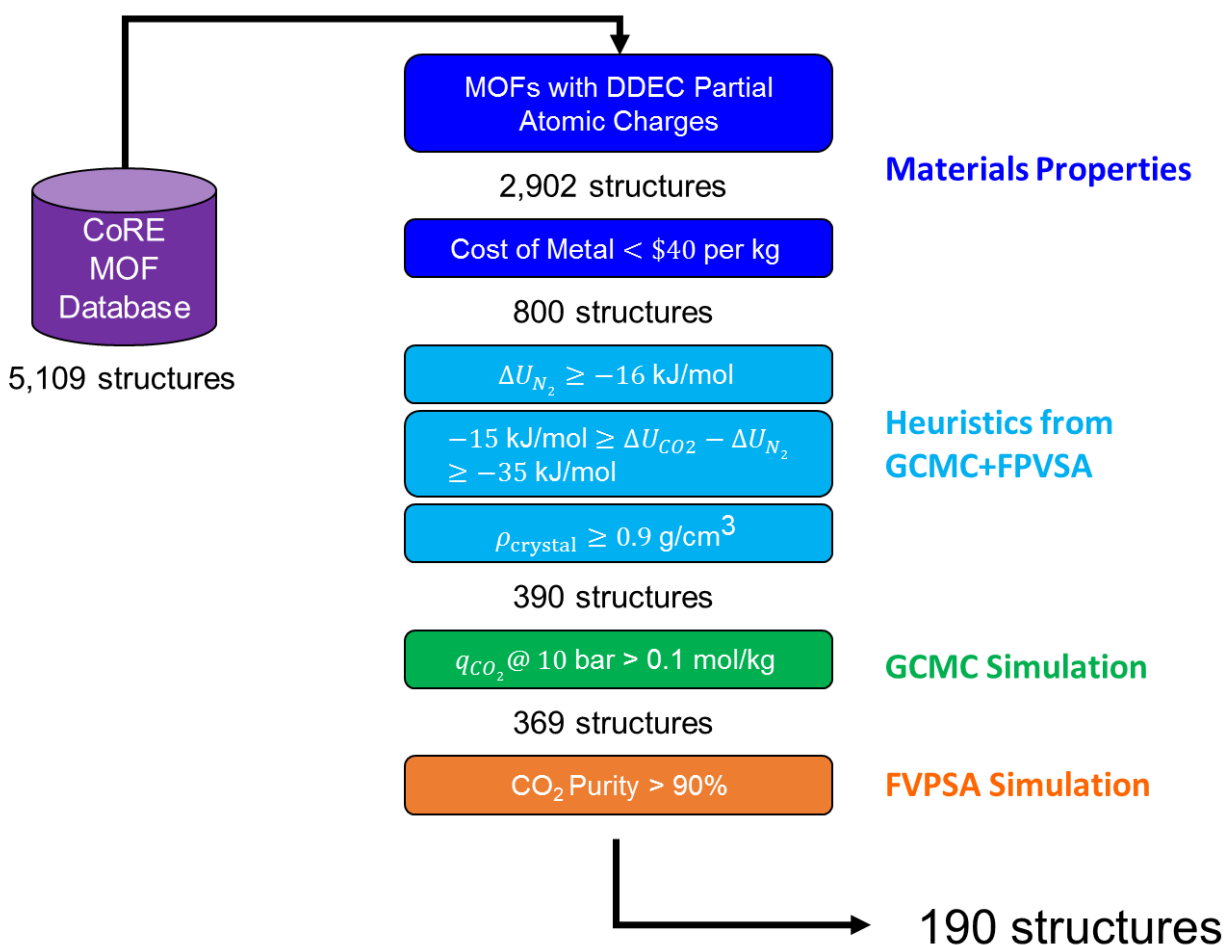


Figure 4.3. Flow diagram for the filtering of candidate MOFs from the CoRE MOF Database. We note that the criteria listed in the boxes are the criteria for keeping MOFs and not removing them. Dark blue boxes contain filters based on intrinsic material properties, such as availability of atomic partial charges and the cost of metal. Sky blue boxes are filters based on the heuristics developed from both GCMC and FVPSA simulations. Green boxes are filters based on GCMC simulation results. Orange boxes are filters based on FVPSA simulations.

simulations, we removed structures that were not able to achieve a 90% CO₂ purity. For the remaining 190 MOF materials, we performed process-level optimization to determine the minimum cost of CO₂ capture, subject to the constraints of 90% CO₂ purity and 90% CO₂ recovery.

4.3.3 Evaluation Metrics from the Literature

Using the calculated cost of CO₂ capture for the 190 MOFs that meet the purity target, we tested simple evaluation metrics from the literature to see how well they perform in ranking the adsorbents. Table 4.2 shows the Spearman correlation coefficients for various metrics versus the cost of CO₂ capture. To calculate these metrics, we used the following definitions, based on the work of Chung and co-workers¹²¹:

$$WC_{CO_2} = N_{CO_2}^{ads} - N_{CO_2}^{des} \quad (4.5)$$

$$WC_{N_2} = N_{N_2}^{ads} - N_{N_2}^{des} \quad (4.6)$$

$$\alpha_{ads} = \frac{N_{CO_2}^{ads}}{N_{N_2}^{ads}} \frac{y_{N_2}^{ads}}{y_{CO_2}^{ads}} \quad (4.7)$$

$$\alpha_{des} = \frac{N_{CO_2}^{des}}{N_{N_2}^{des}} \frac{y_{N_2}^{des}}{y_{CO_2}^{des}} \quad (4.8)$$

where $N_{CO_2}^{ads}$ and $N_{N_2}^{ads}$ are the CO₂ and N₂ loadings for a 15:85 CO₂/N₂ mixture at 1 bar and 313 K, and $N_{CO_2}^{des}$ and $N_{N_2}^{des}$ are the CO₂ and N₂ loadings for a 90:10 CO₂/N₂ mixture at 0.1 bar and 313 K. The desorption conditions were chosen to approximate the final conditions of the adsorption bed at the end of the depressurization step.

Table 4.2 shows that the best performing metric among the existing evaluation metrics is the Separation Factor (SF), with a Spearman Correlation Coefficient of 0.45. Other metrics show low correlation with

respect to the cost of CO₂ capture. Figure 4.4a shows that there is little correlation between the Separation Factor (SF) and the cost of CO₂ at high SF values. Upon examining these results in more detail, we noticed

Table 4.2. Spearman correlation coefficient between the screening metrics and the CO₂ capture cost. Metrics that include the working capacity of N₂ have higher correlation coefficients than the others. The right column is the Spearman correlation coefficient between the CO₂ capture cost and the evaluation metrics with a minimum N₂ working capacity of 0.01 mol/kg implemented. It can be seen that by implementing this minimum value, all of the metrics experienced an increase in the magnitude of the correlation.

Evaluation Metric	 r_s 	 r_s with modified N₂ working capacity
SF	0.45	0.75
AFM ₂	0.38	0.44
S	0.37	0.43
WC _{N2}	0.33	0.40
α_{ads}	0.31	0.31
AFM ₁	0.30	0.30
API	0.30	0.30
α_{des}	0.30	0.30
α_0	0.24	0.24
$\alpha_{ads} / \alpha_{ads}$	0.23	0.23
WC _{CO2}	0.04	0.04

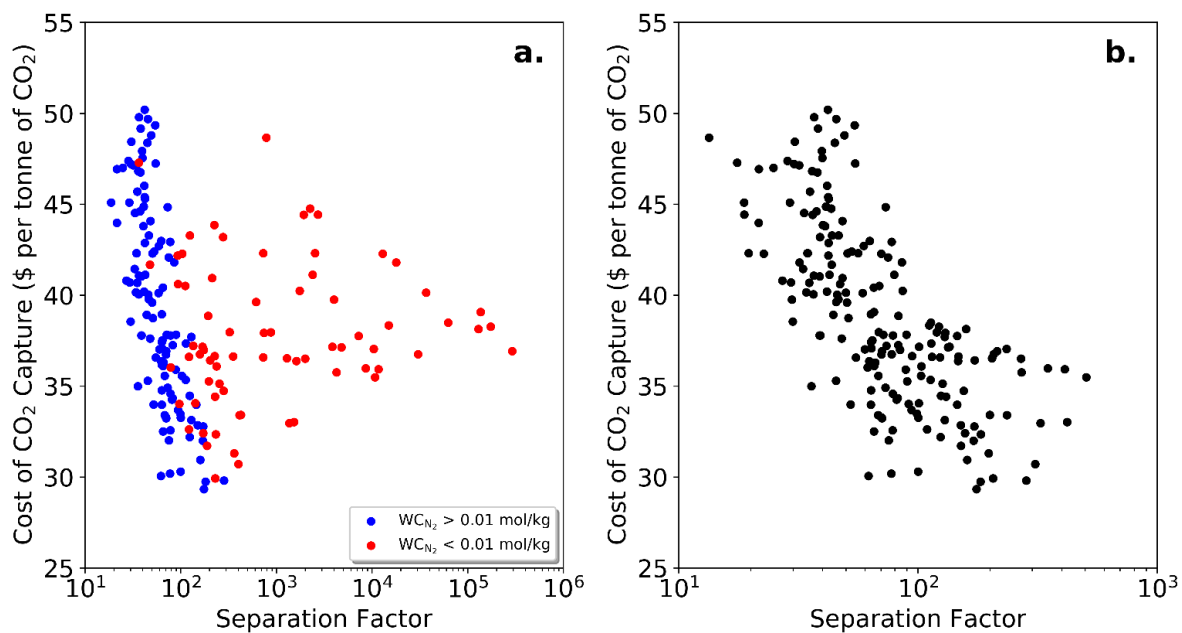


Figure 4.4. a. Relationship between the cost of CO₂ capture and the Separation Factor (SF). For MOFs with low nitrogen working capacity, the SF values are inflated due to very low working capacities of N₂. This leads to no obvious trend between the Separation Factor and the cost of CO₂ capture; b. Relationship between the cost of CO₂ capture and the Modified Separation Factor (with $WC_{N_2} < 0.01$ mol/kg values set to 0.01 mol/kg), which shows a clearer trend.

that the MOFs with the highest SF values all have very low N₂ working capacities. For example, all of the MOFs with SF values above 500 have N₂ working capacities below 0.01 mol/kg (Figure 4.4a). Since the N₂ working capacity appears in the denominator of the SF, even a very small (absolute) variation in WC_{N_2} – for example, small changes within the experimental uncertainty – may have a large impact on the SF. Figure 4.4b shows that if we set a minimum N₂ working capacity of 0.01 mol/kg, to limit its effect on the Separation Factor,

$$WC_{N_2, \text{mod}} = \max(WC_{N_2}, 0.01) \quad (4.9)$$

the Spearman correlation coefficient improves to 0.75. The new Spearman Correlation Coefficients for all metrics that contain the working capacity of N₂ are shown in Table 4.2. For the remainder of the work, we use a modified working capacity of N₂ with a minimum value of 0.01 mol/kg as shown in equation 4.9.

4.3.4 General Evaluation Metric (GEM) for MOF Ranking

Although the correlation between the cost of CO₂ capture and the modified SF is reasonably high, we wanted to use our large dataset of process-level optimization results to create an evaluation metric with even higher ability to rank adsorbents based on the cost of CO₂ capture. To do this, we created a general evaluation metric (EM) containing all features found in the literature metrics along with a few others such as the N₂ heat of adsorption and the crystal density of the MOF:

$$EM = WC_{CO_2} (WC_{N_2, \text{mod}})^a (\alpha_{ads})^b (\alpha_{des})^c (|\Delta U_{CO_2}|)^d (|\Delta U_{N_2}|)^e (\rho)^f \quad (4.10)$$

$$a - f = [-5, 5]$$

where $|\Delta U_{CO_2}|$ and $|\Delta U_{N_2}|$ are the magnitudes of the heats of adsorption of CO₂ and N₂, respectively, in kJ/mol, and ρ is the crystalline density of the MOF in kg/m³. Starting with this expression, we optimized the exponents on the different features, allowing them to range from -5 to 5, to maximize the magnitude of the Spearman Correlation Coefficient. The optimized EM is

$$EM = \frac{WC_{CO_2} \alpha_{ads}^{2.09} \rho^{0.41}}{WC_{N_2,mod}^{1.3} \alpha_{des}^{2.32} |\Delta U_{CO_2}|^{0.54} |\Delta U_{N_2}|^{0.81}} \quad (4.11)$$

We find that the metric has a higher correlation coefficient than any other performance metric, with $r_s = -0.87$.

Equation 4.11 contains a large number of features that might provide redundant information. For example, the selectivities at desorption conditions and adsorption conditions may be related. Therefore, we tested the impact of removing each feature on the correlation coefficient. After all the features had been tested, the feature with the smallest impact on the performance was removed. This process was repeated until only one feature was left. The results from this analysis are shown in Figure 4.5. Note that the process of removing features moves from right to left in Figure 4.5.

Figure 4.5 shows that there is some overlap in the information provided by the seven features. Starting from the left, after the fourth feature (ΔU_{N_2}), little improvement is seen in the performance with additional features. The most important feature is the working capacity of N_2 . While this is initially a surprising result, it is important to note that due to the high CO_2 purity required for CCS applications (> 90%), an increase in the N_2 captured during the feed step will require lower vacuum pressure during the CoC-Depressurization step, resulting in higher energy costs. In addition, similar observations on the impact of N_2 adsorption on the performance of the P/VSA cycle have been reported in the literature.^{113,114} After the working capacity of N_2 , the CO_2 working capacity is the next most important feature, which agrees with traditional thinking on the importance of the CO_2 adsorbed and released during the PSA cycle. Besides the CO_2 and N_2 working capacities, the CO_2/N_2 selectivity at desorption conditions (i.e., low pressure) and the N_2 internal energy of adsorption are also important features. The N_2 internal energy of adsorption is important as it reflects the impact that the temperature change has on the N_2 loading throughout the cycle. The importance of the

CO₂/N₂ selectivity at desorption conditions, rather than at the adsorption conditions, is because the CO₂ product is collected during the desorption step. While it is beneficial for the MOF to initially adsorb

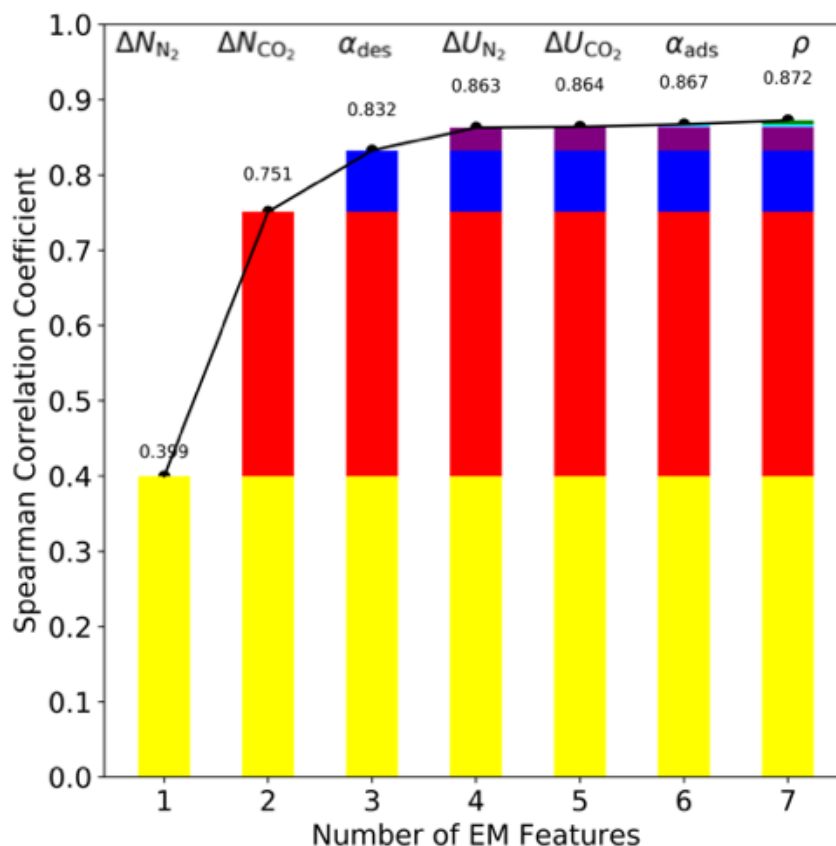


Figure 4.5. The importance of each feature in the evaluation metric (EM) (equation 4.11) developed in this work for the Spearman correlation coefficient (SCC). The higher the value of SCC, the better the metric is in terms of predicting the cost of CO₂ capture. From right to left, the features are the adsorbent density, the selectivity at adsorption conditions, the internal energy of adsorption of CO₂, the internal energy of adsorption of N₂, the selectivity at desorption conditions, the working capacity of CO₂, and the working capacity of N₂. SCC for each column is calculated with the feature listed on top plus the features listed in the previous columns. For example, the three EM features used to calculate SCC in the third column are the N₂ working capacity, the CO₂ working capacity, and the selectivity at desorption condition.

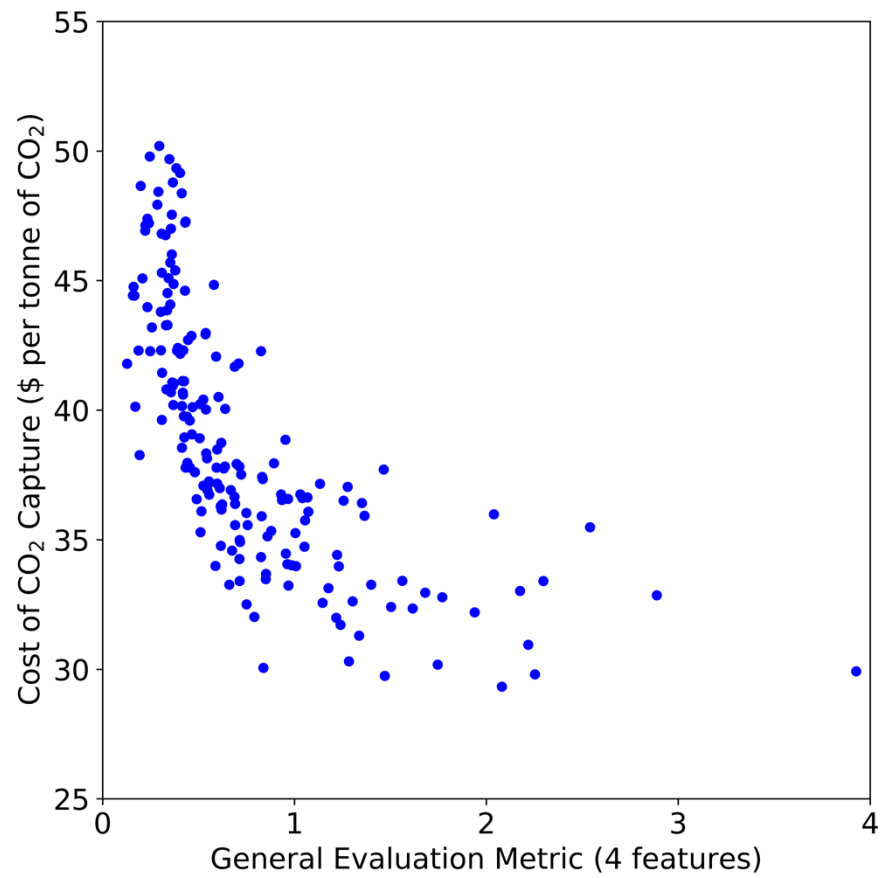


Figure 4.6. Relationship between the four feature General Evaluation Metric (Equation 4.12) and the cost of CO₂ capture. The Spearman correlation coefficient is -0.86 .

significantly more CO₂ than N₂ during the feed step, it is more important that during the desorption steps the CO₂ is de-adsorbing and being collected as a pure product. Thus, the CO₂/N₂ selectivity at the desorption conditions appears in the denominator of the evaluation metric, and we want to minimize this value. The resulting general evaluation metric (GEM) which contains the most important features is:

$$GEM = \frac{WC_{CO_2}}{WC_{N_2, \text{mod}}^{1.32} \alpha_{des}^{0.25} |\Delta U_{N_2}|^{0.97}} \quad (4.12)$$

Figure 4.6 shows the CO₂ capture costs for each of the MOFs plotted against the four-feature general evaluation metric. The Spearman correlation coefficient is -0.86 .

4.3.5 Metric Validation

How does the GEM rank MOFs that are unable to achieve the purity and recovery goals, and how well does the metric perform with new adsorbent data? To answer the first question, we took the 369 MOFs for which we had performed PSA simulation and optimization and calculated their GEM values. The results are plotted as a function of the maximum CO₂ purity attainable by each MOF in Figure 4.7. The results show that GEM can separate the high-performing MOFs (blue data points) from the MOFs that are unable to attain the purity and recovery goals (yellow data points). For the second question, we randomly selected 58 additional MOFs from the CoRE MOF DDEC 2014 database that were removed previously, ensuring to include MOFs removed for each criterion in Figure 4.3. We then carried out FVPSA simulation and optimization. In addition to these 58 MOFs, we also tested zeolite 13X to see how the metric performed with a well-known high-performing adsorbent. The isotherms for zeolite 13X were retrieved from the literature, where they were fitted to experimental results.⁵¹ Of these 59 materials (which includes zeolite 13X), only nine were able to achieve the CO₂ purity and recovery goals. For these nine materials, we calculated the cost of CO₂ capture and plotted the results as a function of the GEM along with the original data points which were used to develop the GEM. See Figure 4.8. From these results, we can see that the

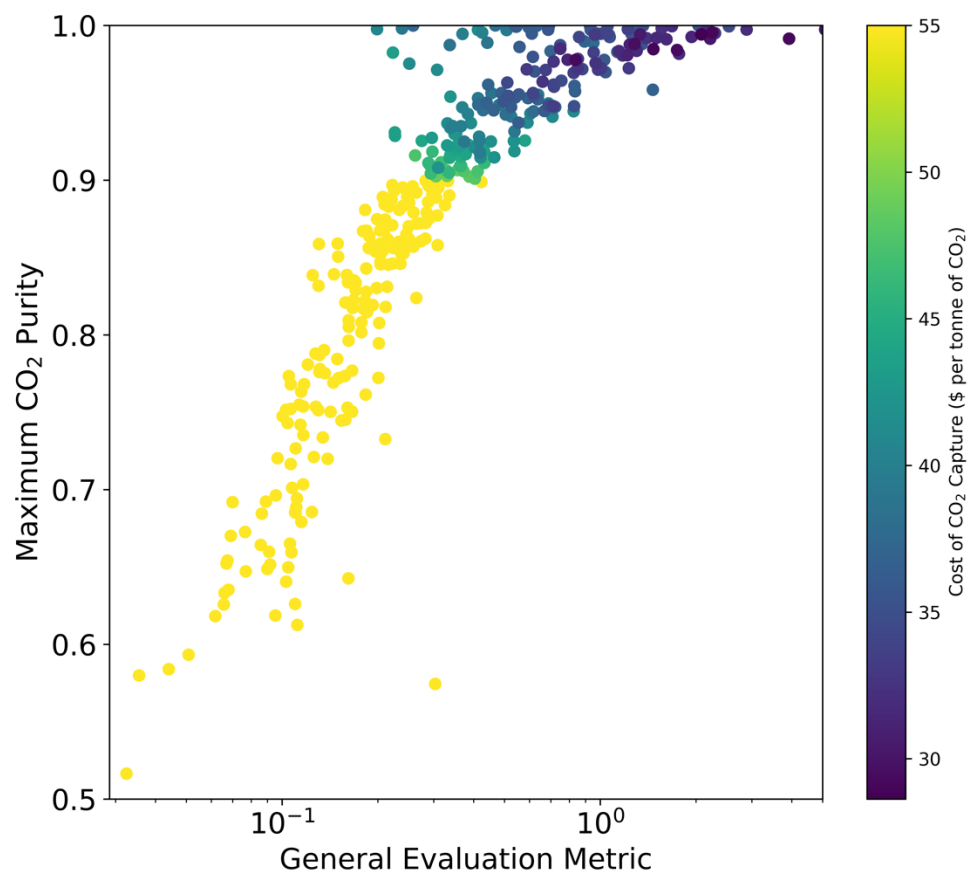


Figure 4.7. Maximum CO₂ purity as a function of the four feature General Evaluation Metric. Materials that were not able to attain 90% purity are assigned an arbitrary cost of CO₂ capture of \$55 per tonne of CO₂.

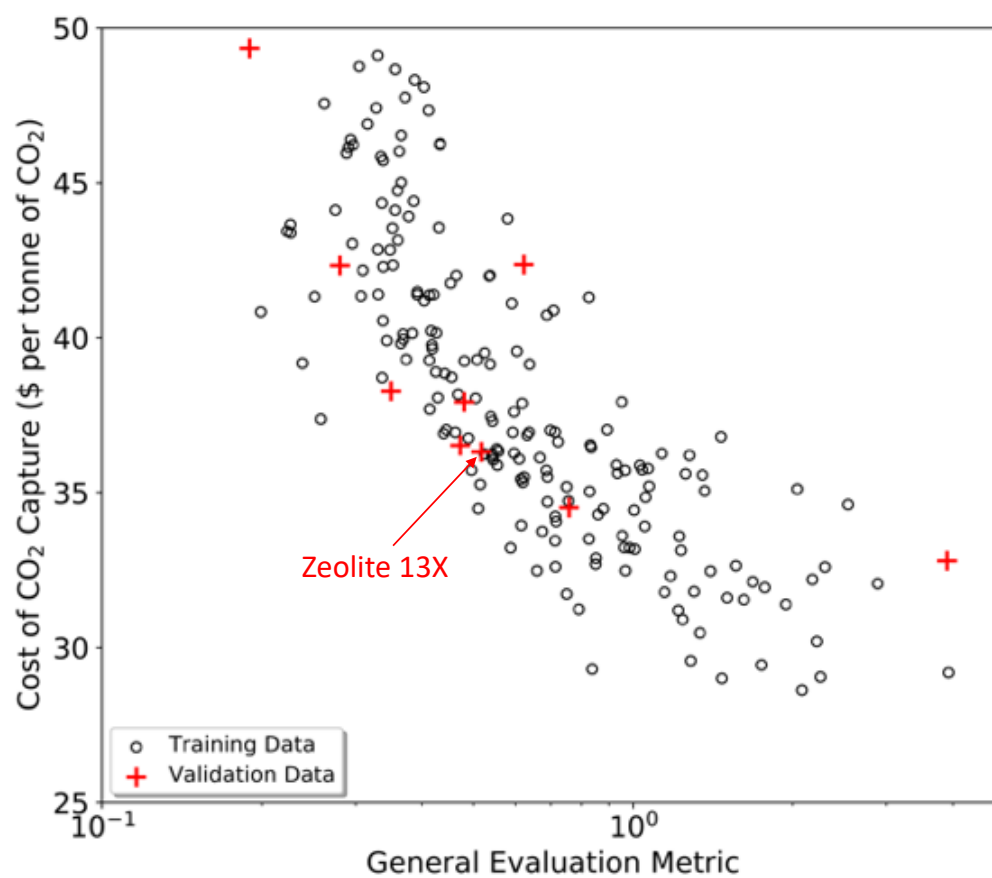


Figure 4.8. Validation of the four feature General Evaluation Metric. Results for all nine of the adsorbents in the validation data set, which the GEM was not trained on, are in good agreement with the trend from the training data. The training data is from 190 CoRE MOFs, and the validation data is from 58 CoRE MOF structures that failed the original screening criteria and zeolite 13X. Only those materials able to meet the purity and recovery requirements are plotted. Adsorption isotherm data for the CoRE MOFs are from GCMC simulations, and isotherm data for zeolite 13X is based on experimental data.⁵¹

Table 4.3. High-performing metal-organic frameworks from the screening with reported experimental gas adsorption data. Accessible geometric surface area, pore limiting diameter, and largest cavity diameter are calculated using Zeo++ software with probe radius = 1.55 Å.

REFCODE or Sorbent Material	Cost of CO ₂ capture (\$ per tonne of CO ₂)	GEM	Experimental BET Surface Area (m ² /g)	Accessible Geometric Surface Area (m ² /g)	Pore Limiting Diameter (Å)	Largest Cavity Diameter (Å)	Ref.
PIJROR (Ln-PCP)	30.1	0.84	731	1219	7.7	8.3	122
HOWQEQ (JUC-68)	31.7	1.23	-	0	3.4	5.0	123
BAXSIE	32.4	1.60	450	707	5.1	5.3	124
GULWOA	33.2	0.97	510	1612	7.2	7.6	125
UBACUX	33.7	1.40	440	0	3.4	7.3	126
XUCNOZ	34.6	0.67	230	0	3.2	6.7	127
HEBTEP	35.1	0.86	-	0	3.1	4.7	128
SAMLAV0 2	35.3	0.51	590 (Langmuir)	1335	4.6	6.4	129
BETFUD (UCY-5)	35.3	0.88	-	2003	4.3	6.2	130
TISGUY	35.9	0.83	-	0	3.5	5.9	131
YEGCUJ	36.3	0.61	600	911	4.8	7.3	132
KIXXOG	36.4	0.70	- ^a	0	2.7	3.8	133
JITPOS	37.6	0.49	117	811	4.9	5.9	134
SAMLAV0 3	37.8	0.45	590 (Langmuir)	1321	4.6	6.4	129
FUFREE	38.0	0.90	< 10	0	3.1	3.7	135
PEJMOI	38.3	0.54	254	763	4.7	7.8	136
NERSUA	38.7	0.61	< 20	1702	6.9	7.1	137
WAJHIA	38.9	0.95	725	0	2.7	3.6	138
ODODIW (PCN-513)	41.0	0.37	-	1702	4.6	7.2	139
ZEBMAW	41.8	0.71	-	1367	3.8	7.1	140

new data points show good correlation with the general trend of the plot, and the metric was able to accurately rank eight of the nine validation data points.

4.3.6 High-performing MOFs

Based on the screening, we identified a number of MOFs with low cost of CO₂ capture. Although all MOFs in the CoRE MOF database have been synthesized in the lab and have existing synthesis procedures, there is no guarantee that all of these MOFs can be successfully activated to yield porosity. One way to check if the MOF can be successfully activated is to see if the original paper reports gas adsorption isotherms for the synthesized MOF. Table 4.3 lists the structures predicted to have low CO₂ capture cost and with reported gas adsorption isotherms. The best performing MOF emerging from the screening is PIJROR (Ln-PCP),¹²² which is a lanthanide based MOF. Based on our calculations, this structure can attain a 97.7% pure CO₂ stream and can capture CO₂ in a FVPSA process at a cost of \$30 per tonne of CO₂. The structure is composed of a 1-dimensional channel densely populated with open metal sites, which likely affect the adsorption of CO₂ molecules at low pressure and, subsequently, the cost of CO₂ capture. Since our molecular simulations do not consider the interaction between open metal sites with CO₂ molecules beyond a simple general force field, further investigation is needed to validate the performance that we predicted for this structure. Since the cost of CO₂ capture for zeolite 13X is around \$36 per tonne of CO₂ captured, Ln-PCP is predicted to outperform zeolite 13X.

4.4. Conclusions

In this work, we developed a hierarchical screening approach for assessing adsorbents for their performance in post-combustion CO₂ capture using pressure-swing adsorption, and we used the approach to screen 5,109 MOFs from the literature. The approach relies on adsorption data predicted by molecular simulation and eliminates materials using simple heuristics based on the heats of adsorption for CO₂ and N₂. These heuristics were developed using process-level PSA modelling on “generic” adsorbents defined by their isotherms, heats of adsorption, and density. We applied the developed heuristics and other factors

to the CoRE MOF database to reduce the number of candidate materials from 5,109 to 369. Process-level modelling and optimization was performed for these 369 materials, and the dataset was further reduced to 190 structures based on other factors, such as CO₂ uptake and purity requirement. These 190 structures are predicted to be able to meet desired purity and recovery targets for post-combustion CO₂ capture.

Following this, we carried out process simulation, optimization, and economic analysis on these 190 MOFs to calculate the cost of carbon capture per tonne of CO₂ using pressure-swing adsorption. These simulations then provided a rich data set to test and develop simple evaluation metrics for ranking adsorbent materials for post-combustion CO₂ capture based on overall cost. We started by testing the ability of existing metrics from the literature to rank the adsorbent materials for post-combustion CO₂ capture and found that the metrics reported in the literature have difficulty ranking the materials based on the cost of CO₂ capture obtained from PSA simulation and optimization. Using our data set, we then sought to develop a new general evaluation metric (GEM) by optimizing the weighting of seven isotherm features that maximizes the magnitude of the Spearman correlation coefficient between the cost of CO₂ capture and the product of those features. We found that only 4 features, CO₂ working capacity, N₂ working capacity, selectivity at desorption condition, and heat of adsorption of N₂ were necessary to approximately rank the materials based on the cost of CO₂ capture. Among these features, the N₂ working capacity appears to be the most important feature, and we noticed that it is also present in all of the best performing metrics found in the literature. The GEM developed in this work can guide future design and screening of materials without having to rely on computationally expensive process modelling and optimization. The proposed GEM development approach may also be applicable to other separation systems.

Chapter 5: Process-Level Modeling to Evaluate Selected Metal-Organic Frameworks for Post-Combustion Capture

5.1. Introduction

Over the last few decades, thousands of MOFs have been synthesized for a variety of applications such as gas separation and storage,^{36,141,142} catalysis applications,^{143,144} and destruction of chemical warfare agents.^{145,146} Over the years, there have been numerous MOFs that have been synthesized and reported as “promising” for CCS applications. In general, MOFs were reported as promising by having high CO₂ working capacity, high CO₂ / N₂ selectivity at adsorption conditions, or some combination of the two. In this study, we wanted to evaluate these top performing MOFs using process-level simulations.

The main goal of this chapter is to investigate fifteen MOFs that have been synthesized and reported in the literature as promising for CO₂ capture applications. We perform process-level simulations for each MOF using a 5-step PSA cycle to see whether the MOFs can achieve the DOE’s goals for CCS. For each MOF that can achieve the goals, we then maximize the productivity and minimize the energy requirements to compare their economic performance. In addition to the main goal, we also investigate the impact the specific PSA cycle has on the relative economic performance of the different MOFs.

5.2. Methodology

5.2.1 Adsorbent Isotherm Fitting[‡]

For this study, experimental CO₂ and N₂ isotherms along with heat of adsorption data were gathered for 15 MOFs, listed in Table 5.1, along with zeolite 13X. The zeolite 13X isotherms were obtained from previous experimental results.⁵¹ For all MOFs, the pure component CO₂ isotherms were fitted to dual-site

[‡] Benjamin Bucior provided assistance with the research in finding the MOFs along with calculating the crystalline density of MOFs.

Langmuir isotherm models, and the pure component N₂ isotherms were fitted to single-site Langmuir isotherm models. To model the competitive isotherms of the two gases, we assumed that the stronger adsorbing CO₂ site, designated as site 1, only adsorbs CO₂ while CO₂ and N₂ compete for the weaker site 2:

$$q_{CO_2} = \frac{q_{sat,CO_2,1} B_{CO_2,1} P_{CO_2}}{1 + B_{CO_2,1} P_{CO_2}} + \frac{q_{sat,CO_2,2} B_{CO_2,2} P_{CO_2}}{1 + B_{CO_2,2} P_{CO_2} + B_{N_2,2} P_{N_2}} \quad (5.1)$$

$$q_{N_2} = \frac{q_{sat,N_2,2} B_{N_2,2} P_{N_2}}{1 + B_{CO_2,2} P_{CO_2} + B_{N_2,2} P_{N_2}} \quad (5.2)$$

where $q_{sat,i,s}$ and $B_{i,s}$ are the saturation loading and isotherm parameter of component i for site s . To account for the temperature effects on the CO₂ and N₂ loading, Arrhenius equations were fitted for the isotherm parameters,

$$B_{i,s} = b_{0,i,s} \exp\left[\frac{-\Delta U_i}{RT}\right] \quad (5.3)$$

where ΔU_i is the internal energy of adsorption of component i . One problem that arose while collecting the isotherm data was the lack of reporting of N₂ heat of adsorption data. While most scientists know the importance of the CO₂ heat of adsorption on the economic feasibility of MOFs for CCS applications and report the data, N₂ heat of adsorption data is often not reported. For MOFs with no N₂ heat of adsorption data reported, we assumed the heat of adsorption to be 12 kJ/mol. To justify this assumption, we performed a sensitivity analysis on the impact the N₂ heat of adsorption has on the maximum CO₂ purity and economic performance of the MOF, which is reported in Appendix D.

5.2.2 PSA Cycle

In this study, we used a 5-step modified Skarstrom cycle, as shown in Figure 5.1. This cycle consists of the following steps: (1) Pressurization, (2) Feed, (3) Heavy Reflux, (4) Counter-Current (CnC) Depressurization, and (5) Light Reflux. The cycle starts with the bed, initially at the low pressure (P_L), being pressurized up to the feed pressure (P_H) using the feed flue gas. After the bed is pressurized, the top end of the column is opened, and the feed gas is fed through. During this step, the CO_2 is concentrated at the front of the column, while the N_2 is leaving through the other end of the column. After a predetermined time, the gas flowing into the column is switched from the flue gas to heavy product collected during the Light Reflux step. Since this heavy product has a higher concentration of CO_2 than the feed gas, this step further increases the concentration of CO_2 at the entrance of the column. At the end of the Heavy Reflux step, the end of the column is closed, and the pressure at the entrance of the column is dropped to P_L . During this step, all the emissions from the entrance are collected as the CO_2 product. Once the bed is fully depressurized, some of the light product produced during the feed step is fed into the end of the column. As mentioned above, a fraction of the heavy product produced in this step, which is predetermined at the start of the cycle, is used as the feed gas during the Heavy Reflux step. While this reflux reduces the amount of CO_2 collected during the cycle, it does significantly enhance the maximum CO_2 purity that can be achieved with different adsorbents, and has been shown in previous investigations to be promising.⁴³

Table 5.1. MOFs investigated during this study along with references for the experimental measurements of their CO₂ and N₂ isotherms and heats of adsorption

MOF	BET Surface Area (m ² /g)	Isotherm Reference
Co-MOF-74	1327	Cho et al. ¹⁴⁷
Cu-BTTRi	1770	Demessence et al. ¹⁴⁸
Cu-TDPAT	1938	Zhang et al. ¹⁴⁹
Mg-MOF-74	1640	Marring et al. ¹¹³
MOF-177	4690	Mason et al. ¹⁵⁰
Ni-MOF-74	1218	Bae and Long ⁸³ and Yu et al. ⁸⁴
NTU-105	3543	Wang et al. ¹⁵¹
Sc ₂ BDC ₃	596	Pillai et al. ¹⁵²
SIFSIX-2-Cu-i	735	Nugent et al. ¹⁵³
SIFSIX-3-Ni	368	Elsaidi et al.(2015) ¹⁵⁴ and Elsaidi et al. (2017) ¹⁵⁵
Ti-MIL-91	380	Benoit et al. ¹⁵⁶
UiO-66	1230	Hu et al. ¹⁵⁷
UTSA-16	628	Xiang et al. ¹⁵⁸
ZIF-8	1025	Zhang et al. ¹⁵⁹
Zn-MOF-74	1176	Xiang et al. ¹⁵⁸

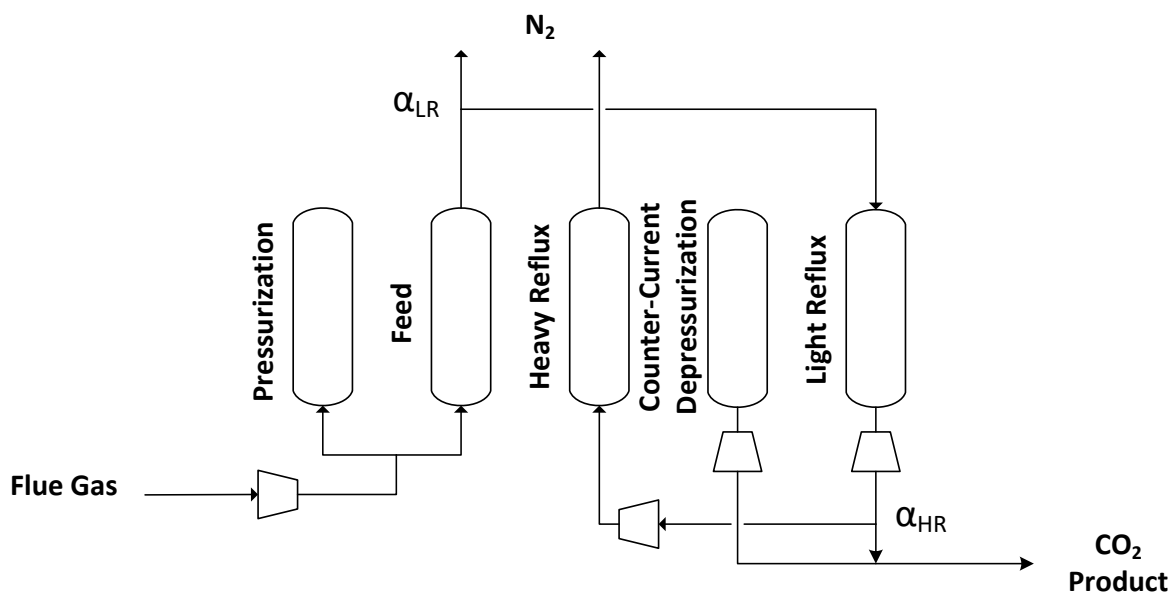


Figure 5.1. Schematic of the 5-step modified Skarstrom cycle used in this study. It is noted that the schematic displays the ordering of the steps for a single column. So, one column will first run the pressurization step, followed by the feed step.

5.2.3 NSGA Optimization Technique

In analyzing the capabilities of the different adsorbents, it is necessary to optimize the operating parameters of the 5-step Modified Skarstrom cycle to determine the maximum CO₂ purity and recovery, along with maximum productivity and minimum energy requirement for each MOF and zeolite. We use the nondominated sorting genetic algorithm (NSGA-II)⁶¹ for the optimization of the cycles. In this study, we perform two separate optimizations: process-level optimization and economic-level optimization. With the process-level optimization, we maximize the CO₂ purity and recovery to identify the MOFs that can achieve the DOE's goal of 90% CO₂ purity and recovery. The CO₂ purity and recovery are defined as

$$Purity = \frac{\int_0^{t_{depress}} \left(\frac{y_i P}{RT} \right) \Big|_{z=0+} dt + (1 - \alpha_{HR}) \int_0^{t_{LR}} \left(\frac{y_i P}{RT} \right) \Big|_{z=0+}}{\int_0^{t_{depress}} \left(\frac{P}{RT} \right) \Big|_{z=0+} dt + (1 - \alpha_{HR}) \int_0^{t_{LR}} \left(\frac{P}{RT} \right) \Big|_{z=0+}} \quad (5.4)$$

$$Recovery = \frac{\int_0^{t_{depress}} \left(\frac{y_i P}{RT} \right) \Big|_{z=0+} dt + (1 - \alpha_{HR}) \int_0^{t_{LR}} \left(\frac{y_i P}{RT} \right) \Big|_{z=0+}}{\int_0^{t_{feed}} \left(\frac{y_i P}{RT} \right) \Big|_{z=0+} dt + \int_0^{t_{pres}} \left(\frac{y_i P}{RT} \right) \Big|_{z=0+}} \quad (5.5)$$

For this optimization, we set the population of the NSGA-II algorithm to 40 and run the algorithm for 60 generations. Since we are only interested in knowing whether the MOFs can achieve the goal and not concerned with a high-level accuracy, we use a course level discretization for this stage of the optimization, dividing the column into 10 finite volume elements.

Once the MOFs that can achieve the DOE's goals are identified, we then perform economic-level optimization, minimizing the energy requirement and maximizing the productivity. The energy requirement and productivity are calculated as follows:

$$\text{Productivity} \left[\frac{\text{mols CO}_2}{\text{kg} \cdot \text{s}} \right] = \frac{\left(\text{CO}_2 \text{ collected during depressurization and LR step} \right)}{\left(\text{Mass of adsorbent} \right) \times \left(\text{Cycle time} \right)} \quad (5.6)$$

$$\text{Energy Requirement} \left[\frac{\text{kWh}}{\text{ton CO}_2} \right] = \frac{\text{Energy required for all steps}}{\text{mass of CO}_2 \text{ collected}} \quad (5.7)$$

The economic-level optimization is performed in two sections. We first perform a coarse level optimization, dividing the column into 10 finite volume elements, and run this optimization for 100 generations with a population of 60. The NSGA-II is initialized with the final results from the process-level optimization. Once the course-level optimization has been run, we then perform a finer level optimization with 30 finite volume elements, initializing this with the coarse level optimization results. We still use a population of 60 for this optimization, but we run the NSGA-II for only 30 generations. The decision variables that are optimized are listed in Table 5.2.

5.3. Results

5.3.1 Purity / Recovery Maximization

The Pareto curves for the purity / recovery optimization are shown in Figure 5.2. As seen from the figure, there is a large range in performance among the sixteen adsorbents. At the low end of the performance, we can see that MOF-177 can only purify the CO₂ product up to 30%. This makes sense, as MOF-177 has a large surface area (~4500 m²/g) and a low crystalline density (0.43 g/cm³).¹⁶⁰ While this large surface area structure is beneficial for applications that need large saturation capacities at high pressures such as hydrogen storage, at the low pressures at which CO₂ capture operates this hinders the performance of MOF-177. At the other end of the performance, we see that there are several MOFs that can achieve the CO₂ purity goal of 90% while recovering 90% of the CO₂. Along with zeolite 13X, which has been shown in earlier chapters to be able to achieve the goals, we found Mg-, Ni-, and Zn-MOF-74,

SIFSIX-Cu-2-I, SIFSIX-Ni-3, UTSA-16, Cu-TDPAT, and Ti-MIL91 met or exceeded the purity goal. From these results, we focused the economic analysis on these nine adsorbents.

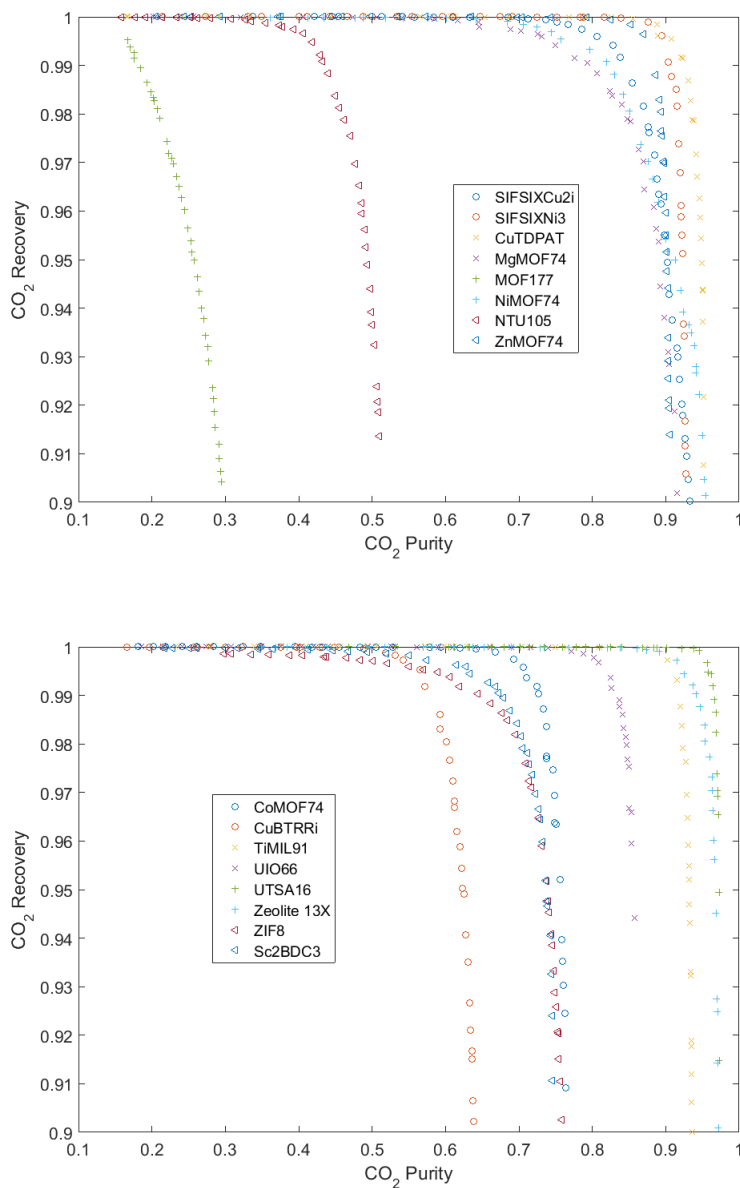


Figure 5.2. Purity / Recovery Pareto front for the 15 MOFs and Zeolite 13X. Of the 16 adsorbents tested, only 9 were able to achieve the DOE's goals for CO₂ capture.

Table 5.2. Decision parameters optimized and fixed for the modified Skarstrom cycle

Parameter	P_H [bar]	t_{feed} [s]	α_{LR} [-]	V_{feed} [m/s]	α_{HR} [-]	P_L
Process Optimization	1 - 10	10 - 1000	0.01 – 0.99	0.1 - 2	Fixed at 1	Fixed at 0.1
Economic Optimization	1 - 10	10 - 1000	0.01 – 0.99	0.1 - 2	0 - 1	0.1 – 0.5

5.3.2 Economic Analysis

While the process-level optimization results do provide information on the capabilities of the adsorbents to achieve the purity and recovery goals, the economic performance of the adsorbents is what will ultimately determine whether it will be implemented for CCS or not. In this analysis, we use the adsorbent productivity and energy requirement as a proxy for the economic cost of the different adsorbents. In the economic analysis, the best performing material will have the lowest energy requirements, minimizing the electricity needed to capture the CO₂, and the highest productivity, minimizing the amount of material needed to capture the CO₂ from a given flue gas flow rate. The results from the economic optimization are shown in Figure 5.3. We note that in the optimization, we set a constraint requiring that all points have a CO₂ purity and recovery above 90%, so all the points are meeting the CCS goals.

From these results, we can see a clear difference in the performance of different MOFs at higher productivities. At this end of the front, UTSA-16 is the best performing material, followed by zeolite 13X, Cu-TDPAT, and Ni-MOF-74. However, at the low energy requirements end of the Pareto curves, all of the materials converge around 150 kWh/ton CO₂. This convergence suggests that depending on the cost of commercially synthesizing the different MOFs, we could potentially see a small or large difference in economic costs between the materials depending on where along the Pareto front the minimum cost is realized.

In order to understand the economic performance of the different adsorbents, we took the best and worst performing materials (UTSA-16 and SIFSIX-3-Ni, respectively) along with zeolite 13X, which performed

well, and plotted their CO₂ and N₂ isotherms, shown in Figure 5.4. From the isotherms we see that the performance of the difference materials seems to be more strongly related to CO₂ isotherm than the N₂ isotherm. While SIFSIX-3-Ni has a very low N₂ isotherm, its CO₂ isotherm is very sharp at low pressures resulting in a low CO₂ working capacity. This sharp isotherm is in sharp contrast to UTSA-16, which has a high CO₂ uptake with a gradual increase in the CO₂ uptake over the pressure range. This difference in CO₂ uptake is even more visible when the working capacity of the three materials are calculated, shown in Table

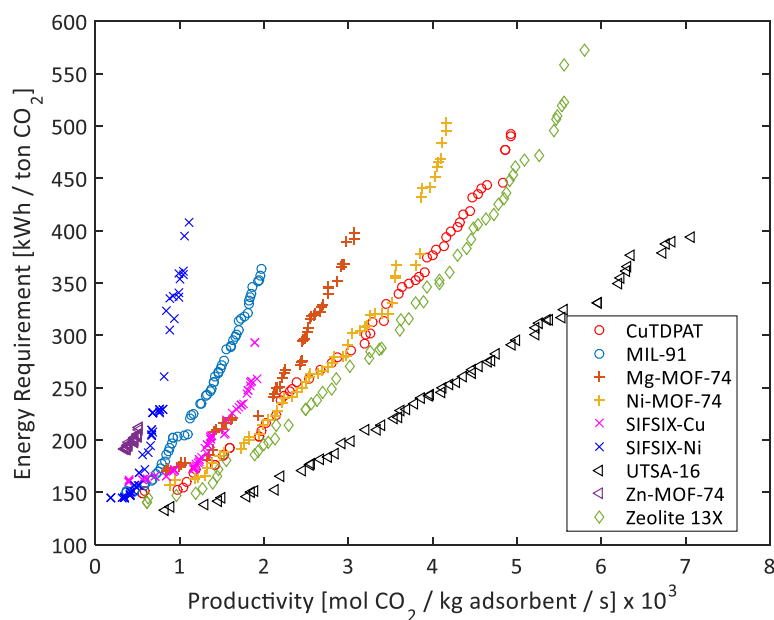


Figure 5.3. The energy / productivity Pareto front for the 9 adsorbents capable of achieving the DOE's goals. The best performing material from this analysis is UTSA-16. All of these points are ensured to have a CO₂ purity and recovery above 90%.

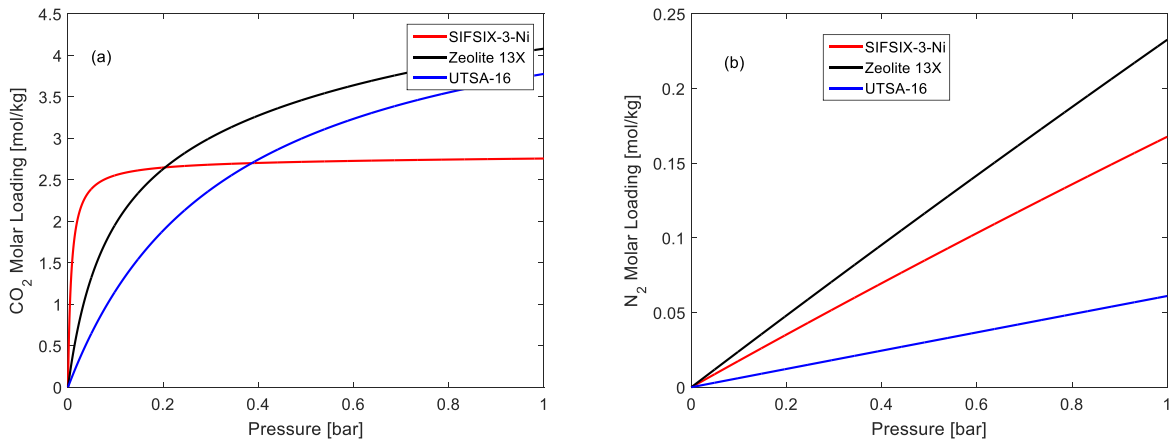


Figure 5.4. Pure Component Isotherms for (a) CO₂ and (b) N₂ at 313 K. The difference in CO₂ working capacity between the three materials is visible, explaining the difference in performance.

Table 5.3. Working capacities of three adsorbents (mol/kg) under adsorption conditions with a CO₂ mole fraction of 15% and 90%. Adsorption conditions are taken as 1 bar pressure and 313 K. Desorption conditions are taken as a 90:10 CO₂:N₂ stream at 0.1 bar at 313 K.

Adsorbent	WC _{CO₂} ($y_{\text{CO}_2} = 0.15$)	WC _{CO₂} ($y_{\text{CO}_2} = 0.9$)
UTSA-16	0.49	3.92
SIFSIX-3-Ni	0.07	0.21
Zeolite 13X	0.32	1.51

5.3. We define the working capacity earlier in chapter 4 as:

$$WC_i = N_{ads,i} - N_{des,i} \quad (5.8)$$

where $N_{ads,i}$ and $N_{des,i}$ are the uptake of component i at adsorption and desorption conditions, respectively. Similar to before, the desorption loading is for a 90:10 CO₂:N₂ stream at 0.1 bar and 313 K. For the adsorption loading, we calculate the working capacity for two streams. First we look at a 15:85 CO₂:N₂ stream at 1 bar and 313 K, along with a 90:10 CO₂:N₂ stream under the same pressure and temperature. While the conditions of the first stream are defined from the flue feed gas, since a heavy reflux step is used in this cycle, the CO₂ gas mole fraction in the column before the depressurization step is probably closer to 90% than 15%. From Table 5.3, we see there is a massive difference between the CO₂ working capacities of the three adsorbents. For the 15:85 CO₂:N₂ stream, SIFSIX-3-Ni has a low working capacity of 0.07

mol/kg, compared to zeolite 13X and UTSA-16 which have working capacities of 0.32 and 0.49 mol/kg, respectively. This difference in working capacities is magnified when the 90:10 CO₂:N₂ stream is examined. UTSA-16 has the largest large working capacity of 3.92 mol/kg, followed by zeolite 13X at 1.51 mol/kg. The working capacity of SIFSIX-3-Ni is still very low at only 0.21 mol/kg. These differences in CO₂ working capacities help to explain the difference in the performance at higher productivities, as the CO₂ working capacity of a material should be directly related to how much CO₂ a given mass of adsorbent can cycle through over a given time.

5.4. Conclusion

In this work, we tested 15 MOFs that were reported in the literature as promising candidates for carbon capture applications and tested them using a five-step Modified Skarstrom cycle, conducting both process- and economic-level analysis. From the process-level analysis, we found that only 8 of the MOFs examined were able to achieve a CO₂ purity and recovery of 90%, the DOE's goal for CCS. Economic-level analysis was then conducted on these 8 MOFs, along with zeolite 13X, using productivity and energy requirement as proxies for the economic cost of the adsorbents. From these results, we found that at low energy requirement values, all the MOFs converged around the same value of ~160 kWh / ton CO₂. However, at higher productivity values, we saw a clear difference emerge, with UTSA-16 the best performing MOF, followed by zeolite 13X, Cu-TDPAT, and Ni-MOF-74. We conclude that one reason for the good performance of the UTSA-16 MOF is its high CO₂ working capacity, especially under adsorption similar to what would be experienced during Heavy Reflux step, i.e. a 90:10 CO₂:N₂ stream at 1 bar and 313 K.

Chapter 6: Rapid Simulation of Pressure Swing Adsorption Cycles Using Artificial Neural Networks

6.1. Introduction

There has been a significant increase in the CO₂ concentration in the atmosphere, with most scientists agreeing that this increase in CO₂ is the primary cause of recent global temperature increases.^{63,161} With fossil fuels expected to be a significant part of the world's energy mix in the foreseeable future, it is important to develop new technologies to reduce and manage CO₂ emissions. One method for reducing CO₂ emissions in the near-term future is carbon capture and sequestration (CCS), where the CO₂ is separated, concentrated and stored in underground rock formations.⁶³ There are currently several methods capable of performing the separation of CO₂ from N₂, including absorption,^{65,104} membranes,^{64,162} and cryogenic distillation.¹⁶³ Of these technologies, amine scrubbing is the commercial method for separating CO₂ from N₂. In this technique, an aqueous amine solution is used to absorb CO₂, separating it from the N₂. Afterwards, the CO₂ is recovered by heating the solution. Unfortunately, the energy penalty to regenerate the aqueous amine is quite high, and making it cost prohibitive for CCS application. Due to the high energy penalty, pressure swing adsorption (PSA) has gained much interest recently as a feasible alternative, due to its low energy requirements.^{65,97}

One key challenge for successful commercial implementation of PSA technology for CCS is to design appropriate cycles for the task. In most commercial PSA applications, the weakly adsorbed (light) component is typically the product of value, and the more strongly adsorbed component (heavy) is discarded as waste. Therefore, commercial PSA processes typically focus on high purities for the light component, which explains the use of light reflux steps.²¹ However, for CCS, the heavy product (CO₂) is the product of concern, requiring high purities and recoveries. Thus for CCS, it is necessary to design cycles for purifying the strongly adsorbed CO₂.

The synthesis of PSA cycles for carbon capture has been a well-studied problem in recent years. While there are only six PSA steps (pressurization, feed, depressurization, heavy reflux, light reflux, and pressure equilibration), the different combination of steps and interactions between different steps leads to hundreds of possible cycles. There have been several studies that have looked at large numbers of cycles to determine the optimal one. Reynolds et al.⁴³ examined nine different cycles incorporating a heavy reflux step using K-promoted HTlc at high temperatures. From this study, they found that the best cycle was a 5-step cycle with light and heavy reflux steps. The heavy reflux feed came from the countercurrent depressurization step, achieving a CO₂ purity and recovery of 98.7% and a feed throughput of 5.8 L STP/hr/kg. The next best was a similar cycle with the heavy reflux feed coming from the light reflux step, achieving a CO₂ purity of 96.5%, recovery of 71.1% and a feed throughput of 57.6 L STP/hr/kg. Haghpanah et al.³⁹ modified their base 4-step Fractionated Vacuum Pressure Swing Adsorption (FVPSA) cycle with heavy reflux, light reflux, pressure equilibration and light product pressurization steps, examining the economic performance of six different cycles with zeolite 13X. From their analysis, they found that a 4-step cycle with a light product pressurization step achieved the best economic performance (lowest energy requirements and highest adsorbent productivity). In both studies, a brute force approach was taken, where every cycle was simulated and tested. One exception to this approach is the work by Agarwal et al.⁵⁹ where they developed a 2-bed PSA superstructure capable of simulating most PSA steps. They used this superstructure to determine the PSA cycle that could achieve the highest CO₂ recovery while maintaining a CO₂ purity of 90%, finding the optimal cycle to be a 6-step cycle with pressure equilibration and heavy reflux steps. A similar analysis was performed for pre-combustion CCS.⁴²

Finding optimal solutions for PSA processes is often challenging primarily due to sets of partial differential and algebraic equations (PDAE) that need to be solved. One approach to reduce the complexity of the problem is using surrogate models, which approximate the underlying model but are computationally cheaper to evaluate. While several different surrogate models have been proposed over the years for PSA,

including proper orthogonal decomposition⁶⁰ and Kriging models,² one interesting surrogate model is artificial neural networks (ANN). ANNs have gained popularity in recent years for solving complex problems including estimating life-cycle impact,¹⁶⁴ predicting adsorption energies calculated from density functional theory,¹⁶⁵ and predicting properties such as density, viscosity, refractive index and thermal conductivity of quaternary systems.¹⁶⁶ In addition to these applications, several studies have looked into using ANNs as surrogate models for PSA cycles. Sundaram¹⁶⁷ used a three-layer neural network to study the relationship between the input and output variables for three different PSA cycles. In addition to this study, there have been several works using ANNs for optimization purposes, training the ANNs on PSA data to minimize relative cost of nitrogen separation,¹⁶⁸ maximize the product purities of propylene/propane separation,¹⁶⁹ and maximize the N₂ purity from N₂/methane separation.¹⁷⁰ Sant Anna et al.¹⁷⁰ also showed that the use of ANN surrogate models reduced the optimization time from 15.7 hrs to 50 s. However, in all these cases, ANNs were used to model the entire PSA process and not individual steps. This results in different ANNs needing to be trained for different PSA cycles. If the ANNs were trained on individual steps, the ANNs could be combined for any desired cycle without the need for additional training or PSA simulations to collect the training data. To the best of our knowledge, no previous work has investigated using ANNS for surrogate models of individual PSA steps.

In this work, we present a framework for creating and training artificial neural networks (ANN) to act as surrogate models for individual pressure swing adsorption (PSA) steps. This is done to reduce the number of equations necessary to solve the steps, reducing the computational time required. We then use these ANNs to maximize the purity and recovery of the PSA cycle. We demonstrate the applicability of this framework by testing three different PSA cycles with zeolite 13X. Among the three cycles, all possible PSA steps are tested. In the future, we plan to use this framework to synthesize optimal PSA cycles for different adsorbents.

6.2. Methodology

6.2.1 Artificial Neural Network Structures

ANNs are nonlinear approximation models that have shown great predictive abilities over a variety of tasks. ANN models consist of three types of layers: input, output and hidden layers. Each of these layers consists of many neurons, with the neurons in the hidden layers containing activation functions to decide whether a neuron is turned on or off. The neurons in each layer are connected to each other by weights, which are trained during the training process to reduce the error between the predicted and expected output values. In addition to the weights, the first three layers also have a bias term which is similar to the other neurons, except that it is always turned on. An example of an ANN is shown in Figure 6.1.

We divided all possible PSA steps into six possible types: 1) Co-Current Pressurization, 2) Counter-Current Pressurization, 3) Co-Current Feed, 4) Counter-Current Feed, 5) Co-Current Depressurization, and 6) Counter Current Depressurization. The Co or Counter current designation is the direction of the gas flow during the step in relation to the flue gas feed direction (feed in through the heavy product end is considered co-current). Using these six step types, most PSA operations can be modeled.

For each step type, there are 12ANNs: 10 ANNs for predicting the 5 state variables at 10 measured locations throughout the column, 1 ANN for each location, and 2 ANNs to predict the CO₂ and total gas flowing into/out of each end of the column.

For all steps, a four layered ANN is used as a surrogate model, with two hidden layers containing 20 hidden nodes each. The number of nodes in the input layer are different for each of the six step types (the number of input nodes is not dependent on the direction of the gas in the column). Each step will have 50 input nodes for the 5 state variables (absolute pressure, CO₂ gas phase mole fraction, CO₂ molar loading, N₂ molar loading, and column temperature) at 10 measured locations throughout the column. In addition to the state variable input nodes, there are input nodes for the operating parameters for each step. For

pressurization steps, there are three operating parameters: the column length (L), the final column pressure (P_0), and the CO₂ mole fraction of the feed gas (y_0). For depressurization steps, there are two operating parameters: the column length (L) and the final column pressure (P_0). For feed steps, there are five operating parameters: the column length (L), the operating pressure (P_0), the Feed gas molar flow rate (\dot{N}_0), the CO₂ mole fraction of the feed gas (y_0), and the duration of the feed step (t). The length of the column is constant among all the steps; however all other input parameters can vary between different steps.

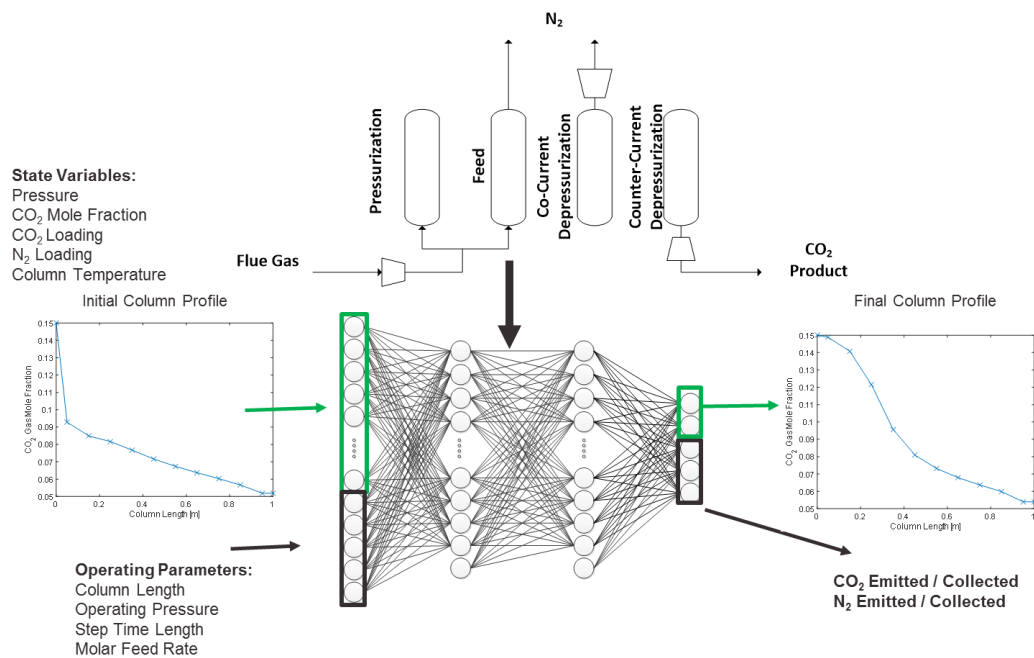


Figure 6.1. Diagram of a Fractionated Vacuum Pressure Swing Adsorption (FVPSA) Cycle and the ANN used to represent the Feed step. The input into the ANN is the column profile at the beginning of the step (which includes all the state variables) and operating parameters important for the feed step. The output of the ANN is the column profile at the end of the Feed step and CO₂ and N₂ that is being fed into / emitted from the column during the step.

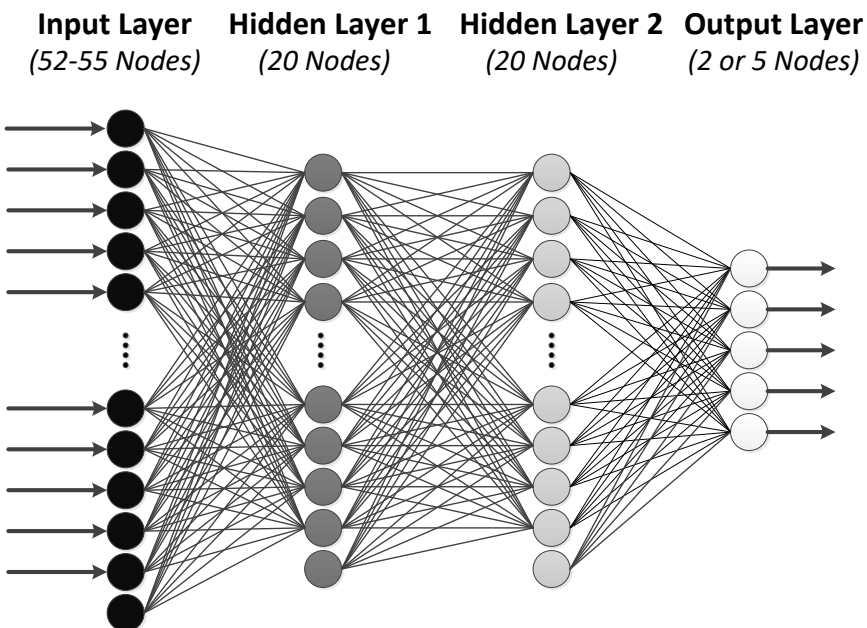


Figure 6.2. A general schematic for the artificial neural network. The initial profile of the column is fed into the input layer along with the operating parameters. The neural network calculates the profile of the column at the end of the step or the CO_2/N_2 that is fed/emitted from the column.

The number of output nodes in the output layer is dependent on whether the ANN is used to predict the column state variables at the end of the step or the CO_2 and N_2 enter/leaving the column. For ANNs used to predict the final conditions of the column, there are 5 output nodes, one for each state variable at one of the measured locations in the column. For ANNs used to predict the gases entering and leaving the column, there are two output nodes, one to predict the CO_2 entering/leaving the column and one to predict the total amount of gas entering/leaving the column. An example of this model is shown in Figure 6.2.

6.2.2 Data Collection and Initial Training

In order to initialize the ANNs, it is necessary to have simulation data for training purposes. The initial training data was first gathered by collecting 300 sample points of the operating variable using the Latin hypercube sampling method, to ensure that the variable space is well sampled. We then simulated each set of operating variables using our PDAE based PSA simulation described in Chapter 2, running the simulations until cyclic steady state (CSS) is achieved. CSS is defined as when the change in the column

profile between the start and end of the cycle is less than 0.5%. It typically takes anywhere from 10 to 200 cycles to find CSS. While the simulations are proceeding, the initial and final column profiles of every fifth cycle along with the CO₂ being fed into / flowing out of the column for each step are collected. This data collection strategy allows for a large number of data points to be collected while ensuring that each of the points is different. We also specify that the last cycle, the cycle that reaches CSS, is collected.

Once the training data has been collected, the ANNs are then initially trained using the ANN regression toolbox in Matlab.¹⁷¹ We train the ANNs on 95% of the data using the Bayesian regularization method. The ANNs are trained for either 600 epochs, i.e. 600 updates of the ANN weights, or until the normalized mean squared error reaches 10^{-8} for the state variable ANNs and the mean square error for the CO₂ and total emissions reaches 10^{-2} .

6.2.3 Optimization Framework and ANN Retraining

Once the ANNs are initially trained, the weights are fed into GAMS¹⁷² where they are used to determine the optimal CO₂ purity-recovery Pareto front. We use the epsilon-constraint method¹⁷³ to establish the Pareto front, and the nonlinear programming (NLP) problems are solved using CONOPT.¹⁷⁴ In order to test the accuracy of the ANN solution, we take the initial column profile points and operating variables and simulate one cycle with the PDAE simulation. We then calculate the error between the ANN predictions and PDAE simulation results for all steps and state variables. If the normalized error between the PDAE simulation and ANN solution is greater than 10^{-03} for any of the state variables for any of the steps, then the simulation data is added to the training data set and the ANNs are retrained on the entire data set, initial training data along with new simulation data points, for 20 epochs. If the normalized error is less than 10^{-03} for all points, optimization framework ends and the ANN results are reported as the optimal Pareto front. A flow chart of the optimization framework is shown in Figure 6.3.

6.3. Results

To test the accuracy of the ANNs and the ability to use them for optimization problems, we model three different PSA cycles, which can be seen in Figure 6.4. We first examine a 3-step cycle composed of a co-current (CoC) pressurization step, a CoC feed step, and a counter-current (CnC) depressurization step.¹¹³ Next, we test the framework on a Skarstrom cycle, which is the same as the first cycle with the addition of a light reflux (CnC Feed step) at the end of the cycle.⁵⁵ Finally, we analyze a 5-step cycle containing a light product Pressurization step (CnC pressurization), Feed step, Heavy Reflux step (CoC feed), CoC Depressurization step, and a CnC Depressurization step. For all cycles, we use zeolite 13X as the adsorbent.⁵¹

6.3.1 Three Step Cycle

The optimization framework required 29 iterations to reach the optimal solution. At the end of the algorithm, the average mean square error for all three steps was 1.7×10^{-08} . This error is broken down further

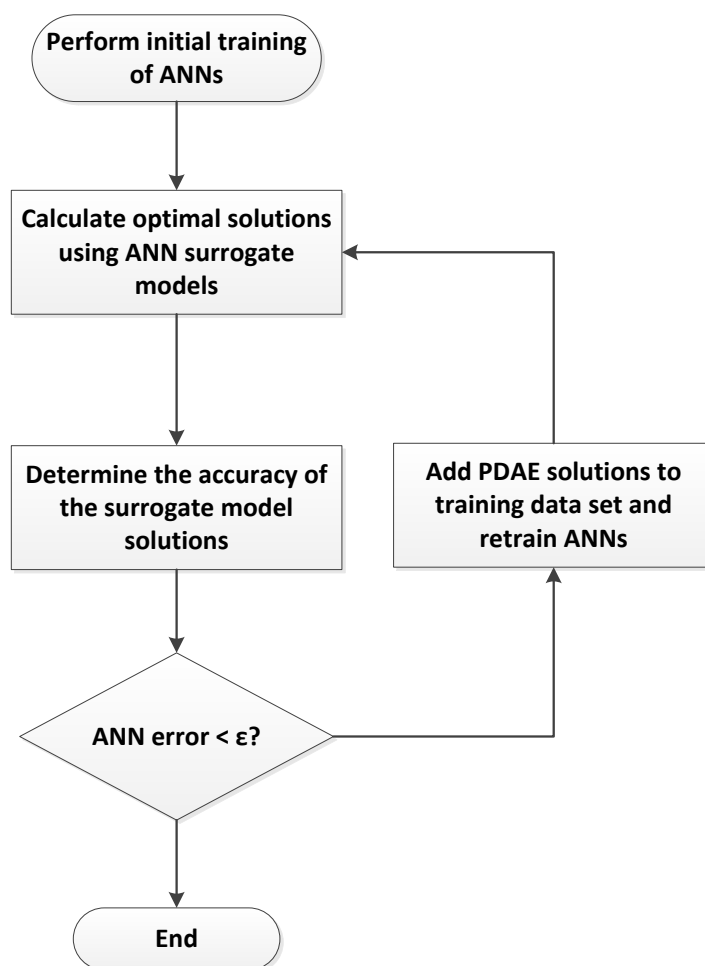


Figure 6.3. Flow diagram of the algorithm used to calculate the purity / recovery Pareto front. The ANNs are used with a derivative based optimization solver to calculate the optimal Pareto front. The predicted optimal points are then simulated with the PDAE equations to determine the accuracy of the ANN results. If the error between the ANN results and the PDE simulation results is greater than 10^{-03} for any point in the column, the PDAE simulation results are added to the training data set and the ANNs are retrained with the new training data set.

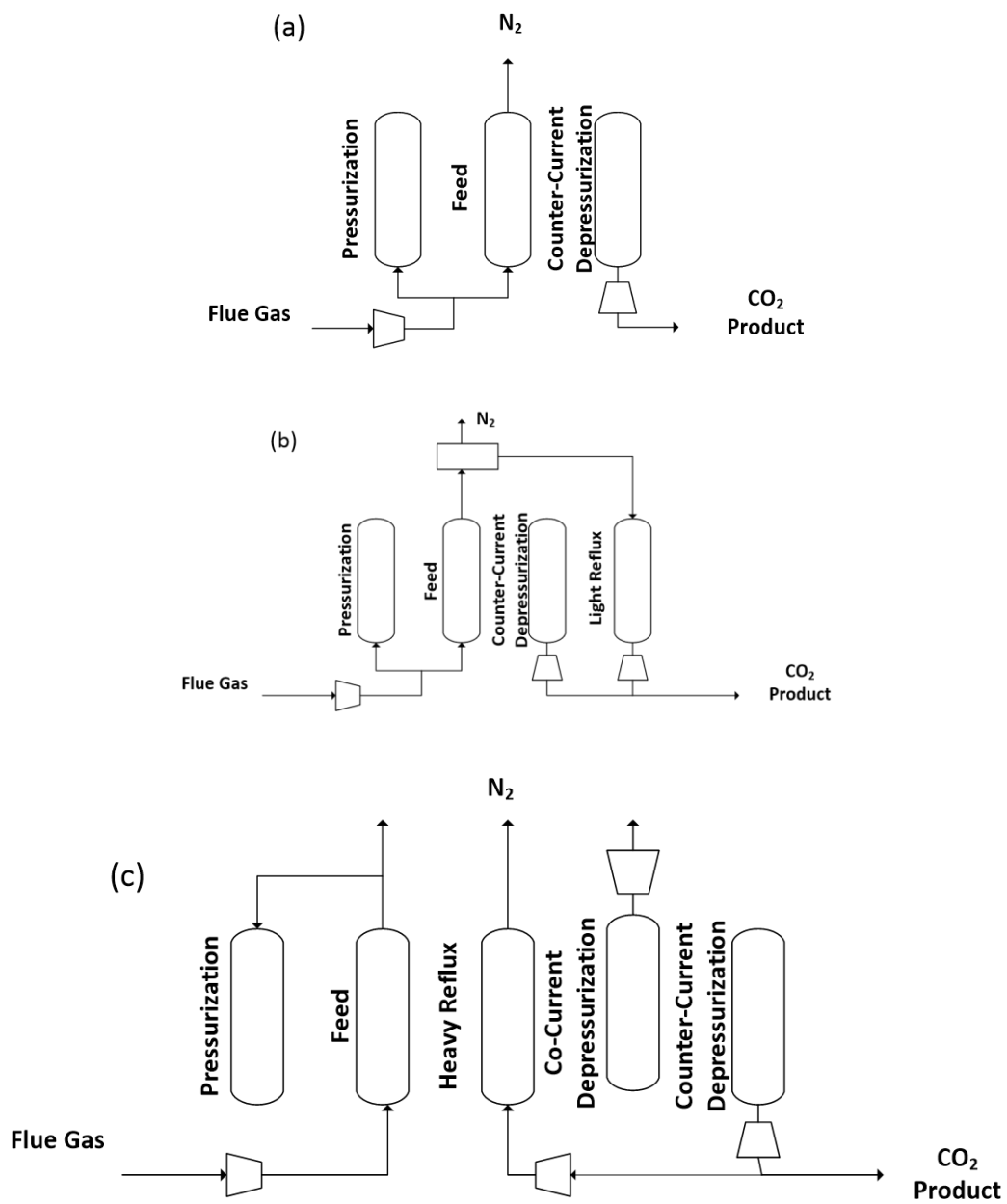


Figure 6.4. Schematics of the three steps tested in this chapter: (a) 3 step cycle, (b) Skarstrom cycle, and (c) 5 step cycle.

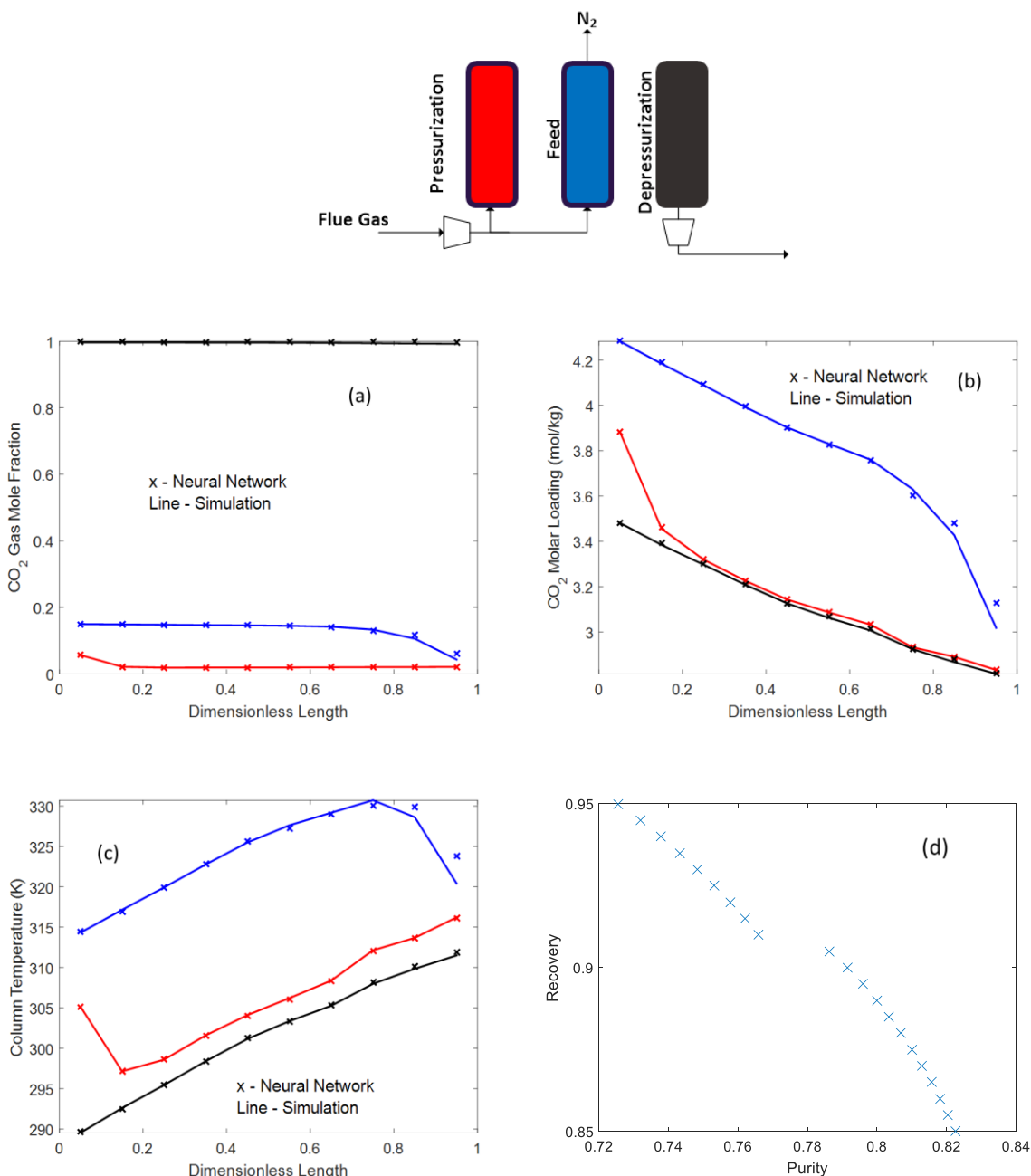


Figure 6.5. Comparison of the (a) CO₂ gas mole fraction, (b) CO₂ molar loading, and (C) temperature profiles throughout the column between the neural network and PDAE simulation results for the result with the highest CO₂ purity with a CO₂ recovery of 90%. The different colored data points correspond to the profiles at the end of the Feed Pressurization (red), Feed (blue), and CnC Depressurization (black) steps. From these plots, it is seen that there is good agreement between the ANN and PDAE simulation results, with only small differences at the end of the column during the Feed step. (d) The Pareto front established from the ANNs for the three step PSA cycle.

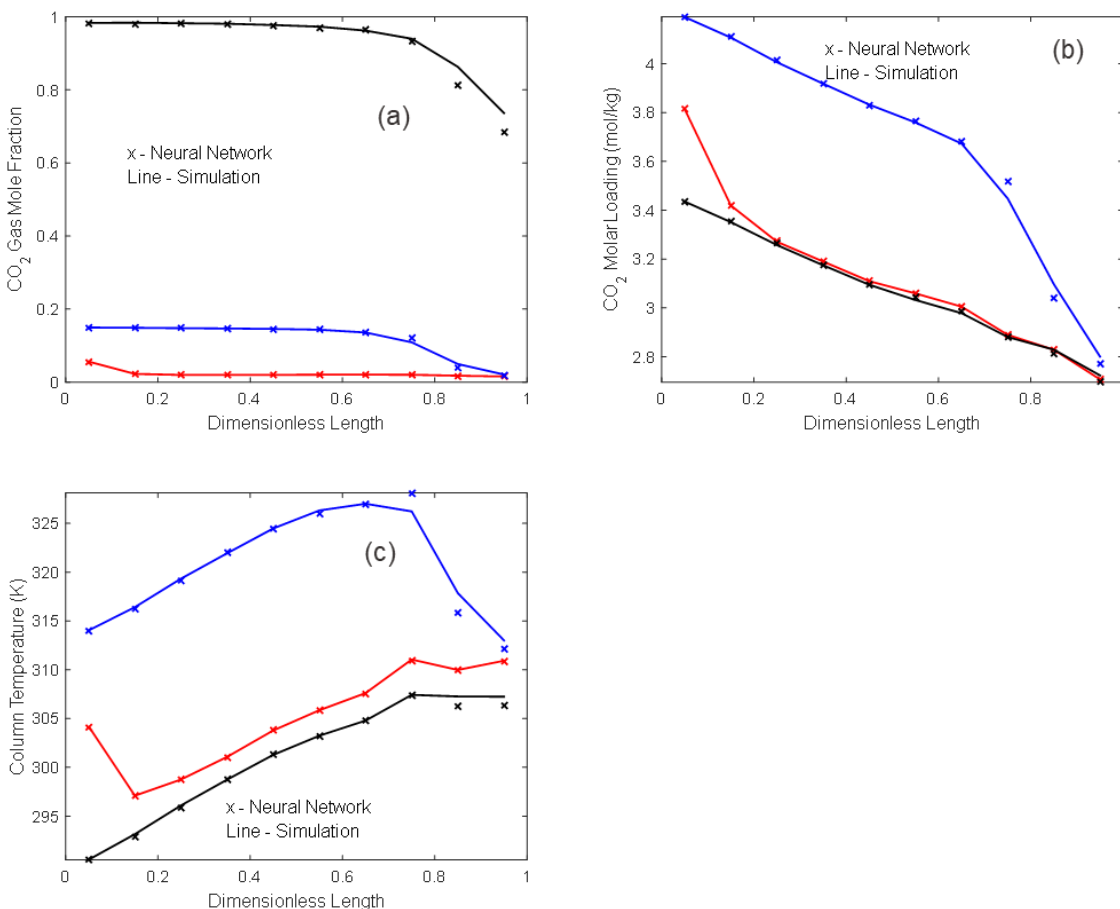


Figure 6.6. Comparison of the (a) CO₂ gas mole fraction, (b) CO₂ molar loading, and (C) temperature profiles throughout the column between the neural network and PDAE simulation results for the result with the highest CO₂ purity with a CO₂ recovery of 91%. The different colored data points correspond to the profiles at the end of the Feed Pressurization (red), Feed (blue), and CnC Depressurization (black) steps. From these plots, we can see that the CO₂ front is not reaching the end of the column at the end of the Feed step. Due to this, there is a significant decrease in the maximum CO₂ purity for a recovery of 90% and 91%. The ANN predicted CO₂ purity and recovery are 76.6% and 91% respectively. The PDAE simulation predicted CO₂ purity and recovery are 76.6% and 90.5% respectively.

Table 6.1. The Mean Square Error of the final ANNs (ANNs at the end of the optimization framework) for all data points in the training set. The MSE is broken down by the state variable and the PSA step.

	Pressure MSE	CO ₂ mole fraction MSE	CO ₂ molar loading MSE	N ₂ molar loading MSE	Temperature MSE
Pressurization	6.7e-09	2.0e-08	1.1e-08	1.2e-08	8.01e-09
Feed	2.3e-08	3.0e-08	3.8e-08	2.0e-08	2.6e-08
CnC Depressurization	9.5e-09	3.0e-08	8.8e-09	2.7e-09	6.7e-09

Table 6.2. Validation results between the ANNs and PDAE simulations for the three step cycle.

	ANN	PDAE Simulations
CO ₂ Purity	79.1%	78.6%
CO ₂ Recovery	90.0%	88.8%
Computation Time for 1000 Simulations [s]	0.5	2560

for the different steps and state variables in Table 6.1. From Table 6.1, we can see that there is good agreement between the ANN and the PDAE simulation results for all the steps. In Figure 6.5, the column profiles from the ANN and PDAE CO₂ gas phase mole fraction, CO₂ molar loading and temperature are shown for the result with the highest CO₂ purity at 90% recovery. From this plot, we can see that there is good agreement between the ANN and PDAE simulations. The only difference between the two is that the ANN slightly overpredicts all three state variables at the end of the Feed step. In Table 6.2, we compare the predicted purities and recoveries of the ANNs and PDAE simulations along with the time required to simulate 1000 cycles.

In Figure 6.5, we see the CO₂ purity / recovery Pareto front for the 3-step cycle. One interesting aspect of the front is that there is a sharp decrease in purity that occurs when increasing the recovery from 90.5% to 91%. Upon examining the column profiles of the 91% recovery point, we found that the reason for this drop off is that CO₂ is breaking through the column at the end of the Feed step. When examining the column profiles for the 91% recovery point (Figure 6.6), we see that there is significant decrease in the CO₂ molar loading at the end of the 91% recovery compared to 90% recovery point. This decrease in the CO₂ molar loading results in less CO₂ that can be capture during the depressurization step, which is why there is a sharp decrease in the CO₂ purity at that point in the Pareto front.

6.3.2 Four Step Cycle (Skarstrom Cycle)

With good results coming from the 3-step cycle, we wanted to increase the number of steps to ensure that the predictive ability is seen with more commercially relevant cycles. For the Skarstrom cycle, the optimization algorithm required 77 iterations before the solution was finalized. At the end of the algorithm, the average mean square error for the four steps was $5.8 \cdot 10^{-08}$. The mean square error is broken down further between different steps and state variables in Table 6.3. In general, there was still good agreement, as the MSE for all the steps was low. However, we can see that for the Skarstrom cycle the Feed Step was the most difficult step to simulate, with MSEs for all its state variables higher than the other steps. In Figure

6.7, the column profile from the ANN and PDAE CO₂ gas phase mole fraction, molar loading and temperature are shown for the result with the highest CO₂ purity at 90% recovery. We continue to see good agreement between the two results, with the only differences in this cycle seen in the CO₂ mole fraction and temperature of the light reflux step. In Table 6.4, we compare the predicted purities and recoveries of the ANNs and PDAE simulations along with the time required to simulate 1000 cycles. In this case, we see even better agreement, with no difference between the CO₂ purity and a small difference between the CO₂ recoveries. Looking at the difference in computational time, a three order of magnitude speed up is achieved by using the ANNs over the PDAE simulation. The CO₂ purity / recovery Pareto front is shown in Figure 6.7. As stated above, this Pareto front is formed by setting the minimum CO₂ recovery throughout the range of values, and then maximizing the CO₂ purity. From this, a smooth Pareto front is seen with a significant drop off in the CO₂ recovery if a purity higher than 84% is desired.

6.3.3 Five Step Cycle

Our final case study for the ANNs surrogate model framework is a 5-step PSA cycle. The cycle consists of (1) a Light Product Pressurization step, (2) a Feed step, (3) a Heavy Reflux step, (4) a Co-Current Depressurization step, and (5) a Counter-Current Depressurization step. A fraction of the heavy product from the Counter-Current depressurization step is used as the feed for the Heavy Reflux step. It is noted that the Feed step and the Heavy Reflux step are both modeled by the CoC Feed step. This results in CoC Feed step having a training data set twice the size as the other steps. In order to maintain the necessary accuracy for the CoC Feed step, we increase the number of nodes in the hidden layers to 30 each.

For the 5-step PSA cycle, 190 iterations were required to find the optimal solution. The average mean square error of the 5 steps is 4.4×10^{-07} , which is about an order of magnitude higher than the Skarstrom cycle. Upon further examination of the breakdown of the MSE, shown in Table 6.5, we can see that this higher error is due to the Heavy Reflux and Co-Current Depressurization steps. Both steps had high error

for all the state variables. In particular, we can see that the prediction of the CO₂ gas mole fraction had the highest error, with both steps having a MSE over 1×10^{-6} for this state variable. However, even with this

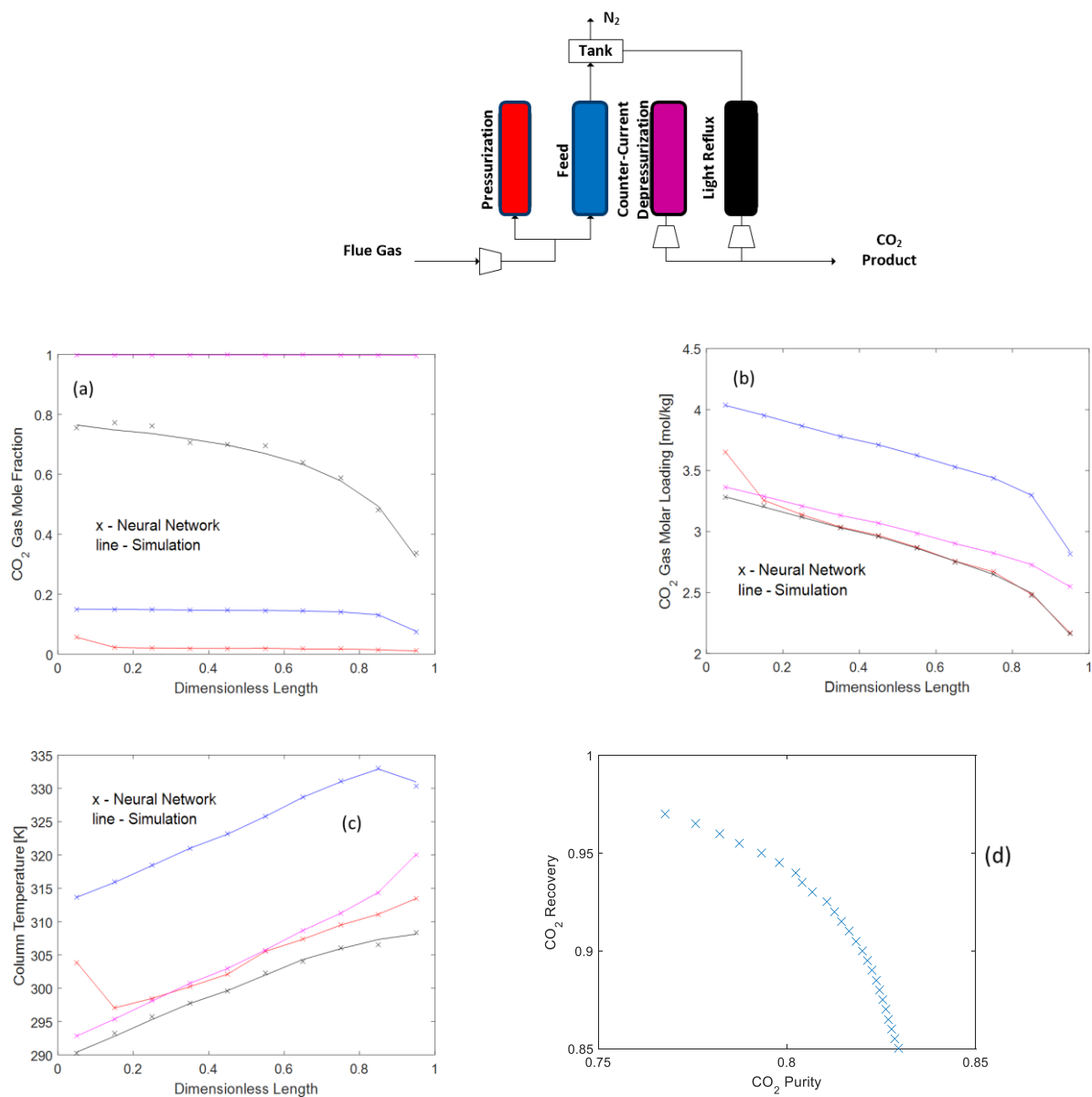


Figure 6.7. Comparison of the (a) CO₂ gas mole fraction, (b) CO₂ molar loading, and (C) Temperature column profile throughout the column between the neural network and PDE simulation results for the result with the highest CO₂ purity with a CO₂ recovery of 90%. The lines correspond to the profile at the end of the Feed Pressurization (red), Feed (blue), CnC Depressurization (purple), and Light Reflux (black) steps. (d) The Pareto front established from the ANNs for the Skarstrom cycle.

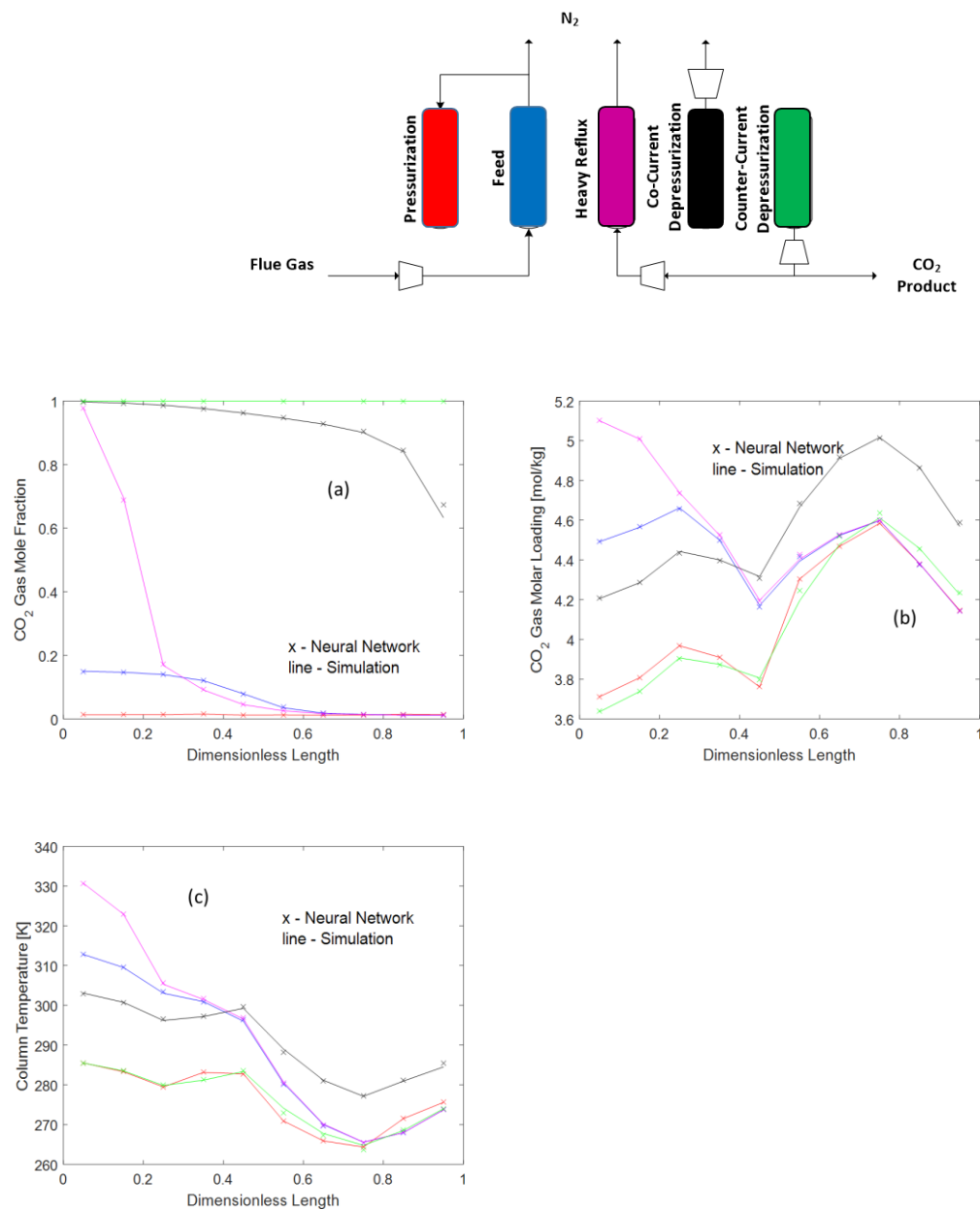


Figure 6.8. Comparison of the (a) CO₂ gas mole fraction, (b) CO₂ molar loading, and (C) Temperature column profile throughout the column between the neural network and PDE simulation results for the result with the highest CO₂ purity with a CO₂ recovery of 90%. The lines correspond to the profile at the end of the Light Product Pressurization (red), Feed (blue), Heavy Reflux (purple), CoC Depressurization (black), and CnC Depressurization (green) steps.

Table 6.3. The Mean Square Error of the final ANNs (ANNs at the end of the optimization framework) for all data points in the training set for the Skarstrom cycle. The MSE is broken down by the state variable and the PSA step.

	Pressure MSE	CO ₂ mole fraction MSE	CO ₂ molar loading MSE	N ₂ molar loading MSE	Temperature MSE
Pressurization	4.9e-09	1.4e-08	1.5e-08	9.1e-09	1.1e-08
Feed	5.1e-08	1.1e-07	1.7e-07	7.9e-08	1.6e-07
CnC Depressurization	1.2e-08	1.0e-07	2.3e-08	2.2e-09	1.5e-08
Light Reflux	5.9e-08	1.5e-07	7.3e-08	1.9e-08	5.0e-08

Table 6.4. Validation results between the ANNs and PDAE simulations for the Skarstrom cycle.

	ANN	PDAE Simulations
CO ₂ Purity	82.0%	82.0%
CO ₂ Recovery	90.0%	89.9%
Computation Time for 1000 Simulations [s]	0.7	1270

Table 6.5. The Mean Square Error of the final ANNs (ANNs at the end of the optimization framework) for all data points in the training set for the five step PSA cycle. The MSE is broken down by the state variable and the PSA step. From this, we can see the CoC Depressurization step and the Heavy Reflux step had some of the higher errors compared to the other three steps.

	Pressure MSE	CO ₂ mole fraction MSE	CO ₂ molar loading MSE	N ₂ molar loading MSE	Temperature MSE
Pressurization	1.0e-09	2.2e-08	2.4e-08	8.6e-09	2.7e-08
Feed	1.4e-07	3.1e-07	3.7e-07	1.0e-07	4.4e-07
Heavy Reflux	3.7e-08	1.8e-06	1.5e-07	8.0e-08	8.5e-08
CoC Depressurization	1.8e-07	5.4e-06	8.6e-07	7.8e-08	4.0e-07
CnC Depressurization	3.4e-08	2.6e-07	5.3e-08	2.9e-09	3.1e-08

Table 6.6. Validation results between the ANNs and PDAE simulations for the Skarstrom cycle.

	ANN	PDAE Simulations
CO ₂ Purity	99.8%	99.7%
CO ₂ Recovery	90.0%	89.4
Computation Time for 1000 Simulations [s]	0.7	3760

higher error, there is still good agreement between the ANN and PDAE solutions as shown in Figure 6.8. From these plots, the only difference between the two solutions that can be seen is with the CO₂ moles fraction profiles at the end of the column at the end of the Co-Current Depressurization step. In Table 6.6, we compare the CO₂ purity and recovery predictions between ANN and PDAE solutions. There is good agreement between the two, with small differences between the predicted purities and recoveries. In respect to the computational time required to simulate 1000 cycles, a three order of magnitude difference is achieved with the ANNs solving the simulations in less than 1 s.

6.4. Conclusions

In this work, we showed that artificial neural networks can be used as surrogate models for the rapid simulation of the individual steps of various PSA cycles. We created six PSA step types that are able to simulate the most common PSA steps used in industrial operations. For each PSA cycle, we trained separate ANNs for each step type using simulation data from our PDAE model. We then use these ANNs to calculate the highest CO₂ purity that can be achieved for each cycle while maintaining a pre-determined CO₂ recovery, retraining the ANNs as necessary to improve the accuracy of the predications.

Three PSA cycles were considered in this work: a three-step PSA cycle, the Skarstrom cycle, and a five-step PSA cycle. Among all three cycles, the six step types that are capable of representing most PSA steps in industrial applications are tested. With all three cycles, we found good agreement between the ANN and the PDAE simulation when looking at the column profiles throughout the cycle and the predicted CO₂ recovery and purity. Moreover, we saw a roughly three order of magnitude speed up with the ANN simulations compared to the PDAE simulations. The use of ANN of surrogate models for PSA steps should allow for effective synthesis of PSA cycles for different adsorbents to minimize the cost of CO₂ capture.

Chapter 7: Conclusions and Recommendations

In this chapter, we highlight the important conclusion from the previous chapters and provide suggestions for future research directions.

7.1. Conclusions

In Chapter 3, we showed the impact water has on the performance of different adsorbents for CO₂ capture, with zeolite 13X performing the best under dry flue gas conditions, but zeolite 13X and zeolite 5A performing equally well under wet flue gas conditions. In addition to these results, we also found that the best option to handle the water in the flue gas is to feed the gas directly into the bed and let the first section of the bed act as a desiccant, while the remainder of the bed separates the CO₂ from the N₂.

In Chapter 4, we developed a general evaluation metric to rapidly rank MOFs based on their expected costs of CO₂ capture. This metric contains the working capacities of CO₂ and N₂, along with the selectivity of CO₂ over N₂ at desorption conditions, and the internal energy of adsorption of N₂. From this investigation, we also found the working capacity of N₂ to be the single most predictive feature for ranking the MOFs.

In Chapter 5, we investigated 15 MOFs that were reported in the literature as promising for CCS applications, calculating their process and economic performance using a 5-step modified Skarstrom cycle. From this analysis, we found that the best performing MOF from the selection was UTSA-16, followed by zeolite 13X, Cu-TDPAT, and Ni-MOF-74.

In Chapter 6, we used Artificial Neural Networks as surrogate models for individual PSA steps to allow for the rapid simulation and optimization of three PSA cycles. We showed that ANNs are capable of simulating most of the potential steps that can be used in industrial PSA operation, testing this approach with a three-step PSA cycle, a Skarstrom cycle, and a 5-step PSA cycle with heavy reflux step.

7.2. Recommendation for Future Research

From the research performed in this dissertation, two promising research directions emerged. First, it would be interesting to continue investigating the impact of water on the PSA cycle performance, looking into different cycles and adsorbents. Second, it would be interesting to perform cycle synthesis on different adsorbents to determine difference in ideal cycles between materials.

In Chapter 3, a two-stage Skarstrom cycle was developed to capture the CO₂ and tested with multiple adsorbents. However, during the investigation we found that the Skarstrom cycle is a poor cycle for CCS, since it required two stages to achieve 90% CO₂ purity goal. Therefore it would be interesting to expand the research to look at the effect of water on other cycles such as the FVPSA or Modified Skarstrom cycle. The inclusion of steps such as the heavy reflux step might result in the water front going further into the bed, further hindering the performance. In addition, all four of the adsorbents examined in Chapter 3 were hydrophilic. Further investigation should look into the difference in performance between hydrophilic MOFs and hydrophobic MOFs like SIFSIX-3-Ni and ZIF-8.

In Chapter 6, we used artificial neural networks (ANNs) as surrogate models for the rapid simulation of PSA cycles. Ideally, these surrogate models will be used for cycle synthesis with mixed integer nonlinear programming (MINLP) solvers. One interesting direction to investigate with the cycle synthesis is to determine the ideal cycle for different adsorbents. So far, work looking into cycle synthesis has used a single adsorbent to test the different cycles. It would be interesting to determine the optimal cycle for different adsorbents and determine if adsorbents with different isotherms (high CO₂ and N₂ working capacities vs low CO₂ and N₂ working capacities) have different ideal cycles. In addition, our work focused on the rapid simulation of PSA cycle with a binary gas mixture. In the future, it would be interesting to investigate optimal PSA cycles for different adsorbents when there are three or more gases.

References

- (1) Zhao, M.; Minett, A. I.; Harris, A. T. A Review of Techno-Economic Models for the Retrofitting of Conventional Pulverised-Coal Power Plants for Post-Combustion Capture (PCC) of CO₂. *Energy Environ. Sci.* **2013**, *6* (1), 25–40.
- (2) Hasan, M. M. F.; Baliban, R. C.; Elia, J. A.; Floudas, C. A. Modeling, Simulation, and Optimization of Postcombustion CO₂ Capture for Variable Feed Concentration and Flow Rate. 2. Pressure Swing Adsorption and Vacuum Swing Adsorption Processes. *Ind. Eng. Chem. Res.* **2012**, *51* (48), 15665–15682.
- (3) Bae, Y. S.; Snurr, R. Q. Development and Evaluation of Porous Materials for Carbon Dioxide Separation and Capture. *Angew. Chemie - Int. Ed.* **2011**, *50*, 11586–11596.
- (4) Hasan, M. M. F.; Baliban, R. C.; Elia, J. A.; Floudas, C. A. Modeling, Simulation, and Optimization of Postcombustion CO₂ Capture for Variable Feed Concentration and Flow Rate. 1. Chemical Absorption and Membrane Processes. *Ind. Eng. Chem. Res.* **2012**, *51* (48), 15642–15664.
- (5) Biegler, L. T.; Jiang, L.; Fox, V. G. Recent Advances in Simulation and Optimal Design of Pressure Swing Adsorption Systems. *Sep. Purif. Rev.* **2005**, *33*, 1–39.
- (6) Sircar, S. Pressure Swing Adsorption. *Ind. Eng. Chem. Res.* **2002**, *41*, 1389–1392.
- (7) Grande, C. A. Advances in Pressure Swing Adsorption for Gas Separation. *ISRN Chem. Eng.* **2012**, *2012*, 1–13.
- (8) Biswas, P.; Agrawal, S.; Sinha, S. Modeling and Simulation for Pressure Swing Adsorption System for Hydrogen Purification. *Chem. Biochem. Eng. Q.* **2010**, *24* (4), 409–414.
- (9) Lopes, F. V. S.; Grande, C. A.; Rodrigues, A. E. Activated Carbon for Hydrogen Purification by Pressure Swing Adsorption: Multicomponent Breakthrough Curves and PSA Performance. *Chem. Eng. Sci.* **2011**, *66* (3), 303–317.
- (10) Knaebel, S. P.; Ko, D. H.; Biegler, L. T. Simulation and Optimization of a Pressure Swing Adsorption System: Recovering Hydrogen from Methane. *Adsorpt. Int. Adsorpt. Soc.* **2005**, *11*, 615–620.
- (11) Grande, C. A.; Cavenati, S.; Da Silva, F.; Rodrigues, A. Carbon Molecular Sieves for Hydrocarbon Separations by Adsorption. *Ind. Eng. Chem. Res.* **2005**, *44* (18), 7218–7227.
- (12) Grande, C. A.; Rodrigues, A. E. Propane/Propylene Separation by Pressure Swing Adsorption Using Zeolite 4A. *Ind. Eng. Chem. Res.* **2005**, *44* (23), 8815–8829.
- (13) Mofarahi, M.; Sadrameli, M.; Towfighi, J. Four-Bed Vacuum Pressure Swing Adsorption Process for Propylene/Propane Separation. *Ind. Eng. Chem. Res.* **2005**, *44* (5), 1557–1564.
- (14) Grande, C. A.; Rodrigues, A. E. Layered Vacuum Pressure-Swing Adsorption for Biogas Upgrading. *Ind. Eng. Chem. Res.* **2007**, *46* (3), 7844–7848.
- (15) Bhadra, S. J.; Farooq, S. Separation of Methane–Nitrogen Mixture by Pressure Swing Adsorption for Natural Gas Upgrading. *Ind. Eng. Chem. Res.* **2011**, *50* (24), 14030–14045.
- (16) Ritter, J. A.; Wu, F.; Ebner, A. D. New Approach for Modeling Hybrid Pressure Swing Adsorption–

- Distillation Processes. *Ind. Eng. Chem. Res.* **2012**, *51* (27), 9343–9355.
- (17) Jeong, J.-S.; Jang, B.-U.; Kim, Y.-R.; Chung, B.-W.; Choi, G.-W. Production of Dehydrated Fuel Ethanol by Pressure Swing Adsorption Process in the Pilot Plant. *Korean J. Chem. Eng.* **2009**, *26* (5), 1308–1312.
- (18) Tajallipour, M.; Niu, C.; Dalai, A. Ethanol Dehydration in a Pressure Swing Adsorption Process Using Canola Meal. *Energy and Fuels* **2013**, *27*, 6655–6664.
- (19) Bhadra, S. J.; Ebner, A. D.; Ritter, J. A. Carbon Monoxide Isotope Enrichment and Separation by Pressure Swing Adsorption. *Adsorption* **2013**, *19*, 11–23.
- (20) Izumi, J.; Yasutake, A.; Kobayashi, S.; Shikichi, A.; Kinugasa, A.; Kohanawa, O.; Okumura, M.; Kanda, T.; Izumoji, Y.; Saigusa, M.; Oguri, D.; Inoue, T.; Oumori, S. A. 14CO and 12CO Separation on Na-X Using Pressure Swing Adsorption at Low Temperatures. *Adsorption* **2005**, *11*, 817–821.
- (21) Ruthven, D. M.; Farooq, S.; Knaebel, K. S. *Pressure Swing Adsorption*; VCH Publishers: New York, NY, 1994.
- (22) Yang, R. T. *Adsorbents: Fundamentals and Applications*; John Wiley & Sons, Inc.: Hoboken, NJ, USA, 2003.
- (23) Li, G.; Xiao, P.; Zhang, J.; Webley, P. A.; Xu, D. The Role of Water on Postcombustion CO₂ Capture by Vacuum Adsorption: Bed Layering and Purge to Feed Ratio. *AIChE* **2014**, *60* (2), 673–689.
- (24) Shen, C.; Liu, Z.; Li, P.; Yu, J. Two-Stage VPSA Process for CO₂ Capture from Flue Gas Using Activated Carbon Beads. *Ind. Eng. Chem. Res.* **2012**, *51* (13), 5011–5021.
- (25) Haghpanah, R.; Rajendran, A.; Farooq, S.; Karimi, I. A. Optimization of One- and Two-Stage Kinetically Controlled CO₂ Capture Processes from Postcombustion Flue Gas on a Carbon Molecular Sieve. *Ind. Eng. Chem. Res.* **2014**, *53* (22), 9186–9198.
- (26) Reynolds, S. P.; Ebner, A. D.; Ritter, J. A. Stripping PSA Cycles for CO₂ Recovery from Flue Gas at High Temperature Using a Hydrotalcite-like Adsorbent. *Ind. Eng. Chem. Res.* **2006**, *45* (12), 4278–4294.
- (27) Krishnamurthy, S.; Haghpanah, R.; Rajendran, A.; Farooq, S. Simulation and Optimization of a Dual-Adsorbent, Two-Bed Vacuum Swing Adsorption Process for CO₂ Capture from Wet Flue Gas. *Ind. Eng. Chem. Res.* **2014**, *53* (37), 14462–14473.
- (28) James, S. L. Metal-Organic Frameworks. *Chem. Soc. Rev.* **2003**, *32* (5), 276–288.
- (29) Eddaoudi, M.; Moler, D. B.; Li, H.; Chen, B.; Reineke, T. M.; O’Keeffe, M.; Yaghi, O. M. Modular Chemistry: Secondary Building Units as a Basis for the Design of Highly Porous and Robust Metal-Organic Carboxylate Frameworks. *Acc. Chem. Res.* **2001**, *34* (4), 319–330.
- (30) Yaghi, O. M.; O’Keeffe, M.; Ockwig, N. W.; Chae, H. K.; Eddaoudi, M.; Kim, J. Reticular Synthesis and the Design of New Materials. *Nature* **2003**, *423* (6941), 705–714.
- (31) Simmons, J. M.; Wu, H.; Zhou, W.; Yildirim, T. Carbon Capture in Metal–organic Frameworks— a Comparative Study. *Energy Environ. Sci.* **2011**, *4* (6), 2177–2185.
- (32) Lin, L.-C. C.; Berger, A. H.; Martin, R. L.; Kim, J.; Swisher, J. A.; Jariwala, K.; Rycroft, C. H.; Bhowan, A. S.; Deem, M. W.; Haranczyk, M.; Smit, B. In Silico Screening of Carbon-Capture

- Materials. *Nat. Mater.* **2012**, *11* (7), 633–641.
- (33) Wilmer, C. E.; Farha, O. K.; Bae, Y.-S.; Hupp, J. T.; Snurr, R. Q. Structure–property Relationships of Porous Materials for Carbon Dioxide Separation and Capture. *Energy Environ. Sci.* **2012**, *5* (12), 9849–9856.
- (34) Krishna, R.; Long, J. R. Screening Metal–Organic Frameworks by Analysis of Transient Breakthrough of Gas Mixtures in a Fixed Bed Adsorber. *J. Phys. Chem. C* **2011**, *115* (26), 12941–12950.
- (35) Krishna, R.; Baur, R. Modelling Issues in Zeolite Based Separation Processes. *Sep. Purif. Technol.* **2003**, *33*, 213–254.
- (36) Herm, Z. R.; Wiers, B. M.; Mason, J. A.; van Baten, J. M.; Hudson, M. R.; Zajdel, P.; Brown, C. M.; Masciocchi, N.; Krishna, R.; Long, J. R. Separation of Hexane Isomers in a Metal–Organic Framework with Triangular Channels. *Science* **2013**, *340* (6135), 960–964.
- (37) Chung, Y. G.; Bai, P.; Haranczyk, M.; Leperi, K. T.; Li, P.; Zhang, H.; Wang, T. C.; Duerinck, T.; You, F.; Hupp, J. T.; Farha, O. K.; Siepmann, J. I.; Snurr, R. Q. Computational Screening of Nanoporous Materials for Hexane and Heptane Isomer Separation. *Chem. Mater.* **2017**, *29* (15).
- (38) Chung, Y. G.; Camp, J.; Haranczyk, M.; Sikora, B. J.; Bury, W.; Krungleviciute, V.; Yildirim, T.; Farha, O. K.; Sholl, D. S.; Snurr, R. Q. Computation-Ready, Experimental Metal–Organic Frameworks: A Tool To Enable High-Throughput Screening of Nanoporous Crystals. *Chem. Mater.* **2014**, *26* (21), 6185–6192.
- (39) Haghpanah, R.; Nilam, R.; Rajendran, A.; Farooq, S.; Karimi, I. A. Cycle Synthesis and Optimization of a VSA Process for Postcombustion CO₂ Capture. *AIChE J.* **2013**, *59* (12), 4735–4748.
- (40) Hasan, M. M. F.; First, E. L.; Floudas, C. A. Cost-Effective CO₂ Capture Based on in Silico Screening of Zeolites and Process Optimization. *Phys. Chem. Chem. Phys.* **2013**, *15* (40), 17601–17618.
- (41) Glueckauf, E.; Coates, J. I. Theory of Chromatography. Part IV. The Influences of Incomplete Equilibrium on the Front Boundary of Chromatograms and on the Effectiveness of Separation. *J. Chem. Soc.* **1947**, 1315–1321.
- (42) Agarwal, A.; Biegler, L. T.; Zitney, S. E. Superstructure-Based Optimal Synthesis of Pressure Swing Adsorption Cycles for Precombustion CO₂ Capture. *Ind. Eng. Chem. Res.* **2010**, *49* (11), 5066–5079.
- (43) Reynolds, S. P.; Mehrotra, A.; Ebner, A. D.; Ritter, J. A. Heavy Reflux PSA Cycles for CO₂ Recovery from Flue Gas: Part I. Performance Evaluation. *Adsorption* **2008**, *14* (2–3), 399–413.
- (44) Rodrigues, A. E.; Dias, M. M. Linear Driving Force Approximation in Cyclic Adsorption Processes: Simple Results from System Dynamics Based on Frequency Response Analysis. *Chem. Eng. Process.* **1998**, *37*, 489–502.
- (45) Hsuen, H. K. An Improved Linear Driving Force Approximation for Intraparticle Adsorption. *Chem. Eng. Sci.* **2000**, *55*, 3475–3480.
- (46) Liu, Y. J.; Ritter, J. A. Evaluation of Model Approximations in Simulating Pressure Swing Adsorption Solvent Vapor Recovery. *Ind. Eng. Chem. Res.* **1997**, *36* (5), 1767–1778.

- (47) Yang, J.; Park, M.; Chang, J.; Ko, S.; Lee, C. Effects of Pressure Drop in a PSA Process. *Korean J. Chem. Eng.* **1998**, *15* (2), 211–216.
- (48) Knaebel, K. S.; Hill, F. B. Pressure Swing Adsorption: Development of an Equilibrium Theory for Gas Separations. *Chem. Eng. Sci.* **1985**, *40* (12), 2351–2360.
- (49) Kayser, J. C.; Knaebel, K. S. Pressure Swing Adsorption: Development of an Equilibrium Theory for Binary Gas Mixtures with Nonlinear Isotherms. *Chem. Eng. Sci.* **1989**, *44* (1), 1–8.
- (50) Schiesser, W. E. *The Numerical Method of Lines: Integration of Partial Differential Equations*; Academic Press: San Diego, 1991.
- (51) Haghpanah, R.; Majumder, A.; Nilam, R.; Rajendran, A.; Farooq, S.; Karimi, I. A.; Amanullah, M. Multiobjective Optimization of a Four-Step Adsorption Process for Postcombustion CO₂ Capture Via Finite Volume Simulation. *Ind. Eng. Chem. Res.* **2013**, *52* (11), 4249–4265.
- (52) You, F. *Sustainability of Products, Processes and Supply Chains: Theory and Applications*; Elsevier, 2015.
- (53) Shampine, L. F.; Reichelt, M. W. The MATLAB ODE Suite. *SIAM J. Sci. Comput.* **1997**, *18* (1), 1–22.
- (54) Shampine, L. F.; Reichelt, M. W.; Kierzenka, J. A. Solving Index-1 DAEs in MATLAB and Simulink. *SIAM Rev.* **1999**, *41* (3), 538–552.
- (55) Skarstrom, C. W. Method and Apparatus for Fractionating Gaseous Mixtures by Adsorption. 2944627, 1960.
- (56) Ko, D.; Siriwardane, R.; Biegler, L. T. Optimization of Pressure Swing Adsorption and Fractionated Vacuum Pressure Swing Adsorption Processes for CO₂ Capture. *Ind. Eng. Chem. Res.* **2005**, *44* (21), 8084–8094.
- (57) Ko, D.; Siriwardane, R.; Biegler, L. T. Optimization of a Pressure-Swing Adsorption Process Using Zeolite 13X for CO₂ Sequestration. *Ind. Eng. Chem. Res.* **2003**, *42* (2), 339–348.
- (58) Wang, L.; Yang, Y.; Shen, W.; Kong, X.; Li, P.; Yu, J.; Rodrigues, A. E. CO₂ Capture from Flue Gas in an Existing Coal-Fired Power Plant by Two Successive Pilot-Scale VPSA Units. *Ind. Eng. Chem. Res.* **2013**, *52* (23), 7947–7955.
- (59) Agarwal, A.; Biegler, L. T.; Zitney, S. E. A Superstructure-Based Optimal Synthesis of PSA Cycles for Post-Combustion CO₂ Capture. *Aiche J.* **2010**, *56* (7), 1813–1828.
- (60) Agarwal, A.; Biegler, L. T.; Zitney, S. E. Simulation and Optimization of Pressure Swing Adsorption Systems Using Reduced-Order Modeling. *Ind. Eng. Chem. Res.* **2009**, *48* (5), 2327–2343.
- (61) Deb, K.; Pratap, A.; Agarwal, S.; Meyarivan, T. A Fast and Elitist Multiobjective Genetic Algorithm: NSGA-II. *IEEE Trans. Evol. Comput.* **2002**, *6* (2), 182–197.
- (62) IEA. Prospect of Limiting the Global Increase in Temperature to 2°C is Getting Bleaker. <http://www.iea.org/newsroomandevents/news/2011/may/name,19839,en.html>.
- (63) Wilcox, J. *Carbon Capture*; Springer New York: New York, NY, 2012.
- (64) Yan, S. P.; Fang, M. X.; Zhang, W. F.; Zhong, W. L.; Luo, Z. Y.; Cen, K. F. Comparative Analysis

- of CO₂ Separation from Flue Gas by Membrane Gas Absorption Technology and Chemical Absorption Technology in China. *Energy Convers. Manag.* **2008**, *49* (11), 3188–3197.
- (65) Rao, A. B.; Rubin, E. S. A Technical, Economic, and Environmental Assessment of Amine-Based CO₂ Capture Technology for Power Plant Greenhouse Gas Control. *Environ. Sci. Technol.* **2002**, *36* (412), 4467–4475.
- (66) Yan, S. P.; Fang, M. X.; Wang, Z.; Xue, J. L.; Luo, Z. Y. Economic Analysis of CO₂ Separation from Coal-Fired Flue Gas by Chemical Absorption and Membrane Absorption Technologies in China. *10th Int. Conf. Greenh. Gas Control Technol.* **2011**, *4*, 1878–1885.
- (67) Couling, D. J.; Prakash, K.; Green, W. H. Analysis of Membrane and Adsorbent Processes for Warm Syngas Cleanup in Integrated Gasification Combined-Cycle Power with CO₂ Capture and Sequestration. *Ind. Eng. Chem. Res.* **2011**, *50* (19), 11313–11336.
- (68) Gong, J.; You, F. Q. Optimal Design and Synthesis of Algal Biorefinery Processes for Biological Carbon Sequestration and Utilization with Zero Direct Greenhouse Gas Emissions: MINLP Model and Global Optimization Algorithm. *Ind. Eng. Chem. Res.* **2014**, *53* (4), 1563–1579.
- (69) Gong, J.; You, F. Global Optimization for Sustainable Design and Synthesis of Algae Processing Network for CO₂ Mitigation and Biofuel Production Using Life Cycle Optimization. *AIChE J.* **2014**, *60* (9), 3195–3210.
- (70) Wang, L.; Yang, Y.; Shen, W. L.; Kong, X. M.; Li, P.; Yu, J. G.; Rodrigues, A. E. Experimental Evaluation of Adsorption Technology for CO₂ Capture from Flue Gas in an Existing Coal-Fired Power Plant. *Chem. Eng. Sci.* **2013**, *101*, 615–619.
- (71) Zhang, J.; Webley, P. A.; Xiao, P. Effect of Process Parameters on Power Requirements of Vacuum Swing Adsorption Technology for CO₂ Capture from Flue Gas. *Energy Convers. Manag.* **2008**, *49* (2), 346–356.
- (72) Yu, W.; LeVan, M. D. Adsorption Equilibrium of Binary Mixtures of Carbon Dioxide and Water Vapor on Zeolites 5A and 13X. *J. Chem. Eng. Data* **2010**, *55*.
- (73) Liu, J.; Wang, Y.; Benin, A. I.; Jakubczak, P.; Willis, R. R.; LeVan, M. D. CO₂/H₂O Adsorption Equilibrium and Rates on Metal-Organic Frameworks: HKUST-1 and Ni/DOBDC. *Langmuir* **2010**, *26* (17), 14301–14307.
- (74) Yazaydin, A. O.; Benin, A. I.; Faheem, S. A.; Jakubczak, P.; Low, J. J.; Willis, R. R.; Snurr, R. Q. Enhanced CO₂ Adsorption in Metal-Organic Frameworks via Occupation of Open-Metal Sites by Coordinated Water Molecules. *Chem. Mater.* **2009**, *21* (8), 1425–1430.
- (75) Xiao, P.; Zhang, J.; Webley, P.; Li, G.; Singh, R.; Todd, R. Capture of CO₂ from Flue Gas Streams with Zeolite 13X by Vacuum-Pressure Swing Adsorption. *Adsorpt. Int. Adsorpt. Soc.* **2008**, *14* (4–5), 575–582.
- (76) Li, G.; Xiao, P.; Zhang, J.; Webley, P. A.; Xu, D. The Role of Water on Postcombustion CO₂ Capture by Vacuum Swing Adsorption: Bed Layering and Purge to Feed Ratio. *AIChE J.* **2014**, *60* (2), 673–689.
- (77) Sumida, K.; Rogow, D. L.; Mason, J. A.; McDonald, T. M.; Bloch, E. D.; Herm, Z. R.; Bae, T.-H.; Long, J. R. Carbon Dioxide Capture in Metal-Organic Frameworks. *Chem. Rev.* **2012**, *112* (2), 724–781.

- (78) EIA. Voluntary Reporting of Greenhouse Gases Program, Table of Fuel and Energy Source: Codes and Emission Coefficients <http://www.eia.doe.gov/oiaf/1605/coefficients.html> (accessed Jan 3, 2015).
- (79) Liu, Z.; Grande, C. A.; Li, P.; Yu, J.; Rodrigues, A. E. Multi-Bed Vacuum Pressure Swing Adsorption for Carbon Dioxide Capture from Flue Gas. *Sep. Purif. Technol.* **2011**, *81* (3), 307–317.
- (80) Wang, L.; Liu, Z.; Li, P.; Wang, J.; Yu, J. CO₂ Capture from Flue Gas by Two Successive VPSA Units Using 13XAPG. *Adsorption* **2012**, *18* (5–6), 445–459.
- (81) Cho, S. H.; Park, J. H.; Beum, H. T.; Han, S. S.; Kim, J. N. A 2-Stage PSA Process for the Recovery of CO₂ from Flue Gas and Its Power Consumption. *Carbon Dioxide Util. Glob. Sustain.* **2004**, *153*, 405–410.
- (82) Liu, Z.; Grande, C. A.; Li, P.; Yu, J.; Rodrigues, A. E. Adsorption and Desorption of Carbon Dioxide and Nitrogen on Zeolite 5A. *Sep. Sci. Technol.* **2011**, *46* (3), 434–451.
- (83) Bae, T. H.; Long, J. R. CO₂/N₂ Separations with Mixed-Matrix Membranes Containing Mg-2(Dobdc) Nanocrystals. *Energy Environ. Sci.* **2013**, *6* (12), 3565–3569.
- (84) Yu, D. C.; Yazaydin, A. O.; Lane, J. R.; Dietzel, P. D. C.; Snurr, R. Q. A Combined Experimental and Quantum Chemical Study of CO₂ Adsorption in the Metal-Organic Framework CPO-27 with Different Metals. *Chem. Sci.* **2013**, *4* (9), 3544–3556.
- (85) Chavan, S.; Bonino, F.; Vitillo, J. G.; Groppo, E.; Lamberti, C.; Dietzel, P. D. C.; Zecchina, A.; Bordiga, S. Response of CPO-27-Ni towards CO, N₂ and C₂H₄. *Phys. Chem. Chem. Phys.* **2009**, *11* (42), 9811–9822.
- (86) Ge, L.; Wang, L.; Rudolph, V.; Zhu, Z. Hierarchically Structured Metal-organic Framework/Vertically-Aligned Carbon Nanotubes Hybrids for CO₂ Capture. *RSC Adv.* **2013**, *3* (47), 25360.
- (87) Wang, Y.; Levan, M. D. Adsorption Equilibrium of Carbon Dioxide and Water Vapor on Zeolites 5A and 13X and Silica Gel: Pure Components. *J. Chem. Eng. Data* **2009**, *54* (10), 2839–2844.
- (88) Turton, R.; Bailie, R. C.; Whiting, W. B.; Shaiwitz, J. A.; Bhattacharyya, D. *Analysis, Synthesis, and Design of Chemical Processes*, 4th ed.; Prentice Hall: Upper Saddle River, NJ, 2012.
- (89) Seider, W. D.; Seader, J. D.; Lewin, D. R.; Widagdo, S. *Product and Process Design Principles: Synthesis, Analysis, and Evaluation*, 3rd ed.; Wiley: Hoboken, NJ, 2009.
- (90) Leperi, K.; Gao, H.; Snurr, R. Q.; You, F. Modeling and Optimization of a Two-Stage MOF-Based Pressure/Vacuum Swing Adsorption Process Coupled with Material Selection. *Chem. Eng. Trans.* **2014**, *39*, 277–282.
- (91) Goos, E.; Riedel, U.; Zhao, L.; Blum, L. Phase Diagrams of CO₂ and CO₂-N₂ Gas Mixtures and Their Application in Compression Processes. *Energy Procedia* **2011**, *4*, 3778–3785.
- (92) Liu, J.; Thallapally, P. K.; McGrail, B. P.; Brown, D. R.; Liu, J. Progress in Adsorption-Based CO₂ Capture by Metal-organic Frameworks. *Chem. Soc. Rev.* **2012**, *41*, 2308.
- (93) Webley, P. A.; He, J. Fast Solution-Adaptive Finite Volume Method for PSA / VSA Cycle Simulation ; 1 Single Step Simulation. *Science* **2000**, *23*, 1701–1712.
- (94) Jiang, G.-S.; Shu, C.-W. Efficient Implementation of Weighted ENO Schemes. *J. Comput. Phys.*

- 1996**, 126, 202–228.
- (95) Mikkelsen, M.; Jørgensen, M.; Krebs, F. C. The Teraton Challenge. A Review of Fixation and Transformation of Carbon Dioxide. *Energy Environ. Sci.* **2010**, 3 (1), 43–81.
- (96) Dessens, O.; Anandarajah, G.; Gambhir, A. Limiting Global Warming to 2 °C: What Do the Latest Mitigation Studies Tell Us about Costs, Technologies and Other Impacts? *Energy Strateg. Rev.* **2016**, 13–14, 67–76.
- (97) Webley, P. A. Adsorption Technology for CO₂ Separation and Capture: A Perspective. *Adsorption* **2014**, 20, 225–231.
- (98) Reynolds, S. P.; Ebner, A. D.; Ritter, J. A. New Pressure Swing Adsorption Cycles for Carbon Dioxide Sequestration. *Adsorption* **2005**, 11, 531–536.
- (99) Furukawa, H.; Cordova, K. E.; O’Keeffe, M.; Yaghi, O. M. The Chemistry and Applications of Metal-Organic Frameworks. *Science* **2013**, 341 (6149), 1230444.
- (100) Slater, A. G.; Cooper, A. I. Function-Led Design of New Porous Materials. *Science* **2015**, 348 (6238), aaa8075-aaa8075.
- (101) McDonald, T. M.; Mason, J. A.; Kong, X.; Bloch, E. D.; Gygi, D.; Dani, A.; Crocellà, V.; Giordanino, F.; Odoh, S. O.; Drisdell, W. S.; Vlasisavljevich, B.; Dzubak, A. L.; Poloni, R.; Schnell, S. K.; Planas, N.; Lee, K.; Pascal, T.; Wan, L. F.; Prendergast, D.; Neaton, J.B.; Smit, B.; Kortright, J.B.; Gagliardi, L.; Bordiga, S.; Reimer, J.A.; Long, J.R. Cooperative Insertion of CO₂ in Diamine-Appended Metal-Organic Frameworks. *Nature* **2015**, 93 (1), 17–19.
- (102) Bae, Y.-S.; Liu, J.; Wilmer, C. E.; Sun, H.; Dickey, A. N.; Kim, M. B.; Benin, A. I.; Willis, R. R.; Barpaga, D.; LeVan, M. D.; Snurr, R. Q. The Effect of Pyridine Modification of Ni-DOBDC on CO₂ Capture under Humid Conditions. *Chem. Commun.* **2014**, 50 (25), 3296–3298.
- (103) Andirova, D.; Lei, Y.; Zhao, X.; Choi, S. Functionalization of Metal-Organic Frameworks for Enhanced Stability under Humid Carbon Dioxide Capture Conditions. *ChemSusChem* **2015**, 8 (20), 3405–3409.
- (104) Flaig, R. W.; Osborn Popp, T. M.; Fracaroli, A. M.; Kapustin, E. A.; Kalmutzki, M. J.; Altamimi, R. M.; Fathieh, F.; Reimer, J. A.; Yaghi, O. M. The Chemistry of CO₂ Capture in an Amine-Functionalized Metal-Organic Framework under Dry and Humid Conditions. *J. Am. Chem. Soc.* **2017**, 139 (35), 12125–12128.
- (105) Wiersum, A. D.; Chang, J. S.; Serre, C.; Llewellyn, P. L. An Adsorbent Performance Indicator as a First Step Evaluation of Novel Sorbents for Gas Separations: Application to Metal-Organic Frameworks. *Langmuir* **2013**, 29 (10), 3301–3309.
- (106) Krishna, R. Screening Metal-organic Frameworks for Mixture Separations in Fixed-Bed Adsorbers Using a Combined Selectivity/Capacity Metric. *RSC Adv.* **2017**, 7 (57), 35724–35737.
- (107) Braun, E.; Zurhelle, A. F.; Thijssen, W.; Schnell, S. K.; Lin, L.-C.; Kim, J.; Thompson, J. A.; Smit, B. High-Throughput Computational Screening of Nanoporous Adsorbents for CO₂ Capture from Natural Gas. *Mol. Syst. Des. Eng.* **2016**, 1 (2), 175–188.
- (108) Huck, J. M.; Lin, L.-C.; Berger, A. H.; Shahrak, M. N.; Martin, R. L.; Bhowan, A. S.; Haranczyk, M.; Reuter, K.; Smit, B. Evaluating Different Classes of Porous Materials for Carbon Capture. *Energy Environ. Sci.* **2014**, 7 (12), 4132–4146.

- (109) Knaebel, K. S. For Your next Separation. *Chem. Eng.* **1995**, *102*, 92–98.
- (110) Rege, S.; Yang, R. A Simple Parameter for Selecting an Adsorbent for Gas Separation by Pressure Swing Adsorption. *Sep. Sci. Technol.* **2001**, *36* (15), 3355–3365.
- (111) Notaro, F.; Mullhaupt, J. T.; Leavitt, F. W.; Ackley, M. W. Adsorption Process and System Using Multilayer Adsorbent Beds. 5810909, 1998.
- (112) Pirngruber, G. D.; Hamon, L.; Bourrelly, S.; Llewellyn, P. L.; Lenoir, E.; Guillerm, V.; Serre, C.; Devic, T. A Method for Screening the Potential of MOFs as CO₂ Adsorbents in Pressure Swing Adsorption Processes. *ChemSusChem* **2012**, *5*, 762–776.
- (113) Maring, B. J.; Webley, P. A. A New Simplified Pressure/Vacuum Swing Adsorption Model for Rapid Adsorbent Screening for CO₂ Capture Applications. *Int. J. Greenh. Gas Control* **2013**, *15*, 16–31.
- (114) Rajagopalan, A. K.; Avila, A. M.; Rajendran, A. Do Adsorbent Screening Metrics Predict Process Performance? A Process Optimisation Based Study for Post-Combustion Capture of CO₂. *Int. J. Greenh. Gas Control* **2016**, *46*, 76–85.
- (115) Khurana, M.; Farooq, S. Adsorbent Screening for Postcombustion CO₂ Capture: A Method Relating Equilibrium Isotherm Characteristics to an Optimum Vacuum Swing Adsorption Process Performance. *Ind. Eng. Chem. Res.* **2016**, *55* (8), 2447–2460.
- (116) Nazarian, D.; Camp, J. S.; Sholl, D. S. A Comprehensive Set of High-Quality Point Charges for Simulations of Metal-Organic Frameworks. *Chem. Mater.* **2016**, *28* (3), 785–793.
- (117) Dubbeldam, D.; Calero, S.; Ellis, D. E.; Snurr, R. Q. RASPA: Molecular Simulation Software for Adsorption and Diffusion in Flexible Nanoporous Materials. *Mol. Simul.* **2016**, *42* (2), 81–101.
- (118) Rappé, A. K. K.; Casewit, C. J. J.; Colwell, K. S. S.; Goddard III, W. A.; Skiff, W. M. UFF, a Full Periodic Table Force Field for Molecular Mechanics and Molecular Dynamics Simulations. *J. Am. Chem. Soc.* **1992**, *114* (25), 10024–10035.
- (119) Potoff, J. J.; Siepmann, J. I. Vapor–liquid Equilibria of Mixtures Containing Alkanes, Carbon Dioxide, and Nitrogen. *AIChE J.* **2001**, *47* (7), 1676–1682.
- (120) Rao, M. B.; Sircar, S. Thermodynamic Consistency for Binary Gas Adsorption Equilibria. *Langmuir* **1999**, *15* (21), 7258–7267.
- (121) Chung, Y. G.; Gómez-Gualdrón, D. A.; Li, P.; Leperi, K. T.; Deria, P.; Zhang, H.; Vermeulen, N. A.; Stoddart, J. F.; You, F.; Hupp, J. T.; Farha, O. K.; Snurr, R. Q. In Silico Discovery of Metal-Organic Frameworks for Precombustion CO₂ Capture Using a Genetic Algorithm. *Sci. Adv.* **2016**, *2* (10), e1600909.
- (122) Kajiwara, T.; Higuchi, M.; Yuasa, A.; Higashimura, H.; Kitagawa, S.; Monge, M. A.; Margiolaki, I.; O’Keeffe, M.; Yaghi, O. M.; Watanabe, D.; Oshima, S.; Kitagawa, S. One-Dimensional Alignment of Strong Lewis Acid Sites in a Porous Coordination Polymer. *Chem. Commun.* **2013**, *49* (89), 10459–10461.
- (123) Xue, M.; Zhu, G.; Ding, H.; Wu, L.; Zhao, X.; Jin, Z.; Qiu, S. Six Three-Dimensional Metal–Organic Frameworks with (3,4)-, (4,5)-, and (3,4,5)-Connected Nets Based on Mixed Ligands: Synthesis, Structures, and Adsorption Properties. *Cryst. Growth Des.* **2009**, *9* (3), 1481–1488.

- (124) Sen, R.; Saha, D.; Koner, S. Controlled Construction of Metal–Organic Frameworks: Hydrothermal Synthesis, X-Ray Structure, and Heterogeneous Catalytic Study. *Chem. - A Eur. J.* **2012**, *18* (19), 5979–5986.
- (125) Ouellette, W.; Zubieta, J. Solid State Coordination Chemistry of Microporous Metal–organic Frameworks of the Cadmium(II)–4-Pyridyltetrazolate Family: The Structural Influences of Chloride Incorporation. *Chem. Commun.* **2009**, *0* (30), 4533.
- (126) Chang, Z.; Zhang, D.-S.; Chen, Q.; Li, R.-F.; Hu, T.-L.; Bu, X.-H. Rational Construction of 3D Pillared Metal–Organic Frameworks: Synthesis, Structures, and Hydrogen Adsorption Properties. *Inorg. Chem.* **2011**, *50* (16), 7555–7562.
- (127) Liu, H.-Y.; Zhang, Z.-J.; Shi, W.; Zhao, B.; Cheng, P.; Liao, D.-Z.; Yan, S.-P.; Kobayashi, T. C.; Wang, P.; Wang, D. J.; Wei, Y. A 3D Porous Hetero-Metal Compound with Helical Channels. *Dalt. Trans.* **2009**, *36* (23), 4416–4419.
- (128) Wang, F.; Tan, Y.-X.; Zhang, J. Hydrothermal Synthesis and Distinct Thermal Behavior of Isostructural Transition Metal-Based MIL-53 Analogs. *Solid State Sci.* **2012**, *14* (9), 1263–1266.
- (129) Wang, X.-F.; Wang, Y.; Zhang, Y.-B.; Xue, W.; Zhang, J.-P.; Chen, X.-M.; Streek, J. van de; Brammer, L.; Arcos, T.; Krasnopolski, M.; Meilikhov, M.; Winter, J.; Terfort, A.; Wöll, C.; Fischer, R. A. Layer-by-Layer Evolution and a Hysteretic Single-Crystal to Single-Crystal Transformation Cycle of a Flexible Pillared-Layer Open Framework. *Chem. Commun.* **2012**, *48* (1), 133–135.
- (130) Efthymiou, C. G.; Kyprianidou, E. J.; Milios, C. J.; Manos, M. J.; Tasiopoulos, A. J. Flexible Lanthanide MOFs as Highly Selective and Reusable Liquid MeOH Sorbents. *J. Mater. Chem. A* **2013**, *1* (16), 5061–5069.
- (131) Hu, S.; Zhang, J.-P.; Li, H.-X.; Tong, M.-L.; Chen, X.-M.; Kitagawa, S. A Dynamic Microporous Metal–Organic Framework with BCT Zeolite Topology: Construction, Structure, and Adsorption Behavior. *Cryst. Growth Des.* **2007**, *7* (11), 2286–2289.
- (132) Navarro, J. A. R.; Barea, E.; Salas, J. M.; Masciocchi, N.; Galli, S.; Sironi, A.; Ania, C. O.; Parra, J. B. H₂, N₂, CO, and CO₂ Sorption Properties of a Series of Robust Sodalite-Type Microporous Coordination Polymers. *Inorg. Chem.* **2006**, *45* (6), 2397–2399.
- (133) Raja, D. S.; Luo, J.-H.; Yeh, C.-T.; Jiang, Y.-C.; Hsu, K.-F.; Lin, C.-H. Novel Alkali and Alkaline Earth Metal Coordination Polymers Based on 1,4-Naphthalenedicarboxylic Acid: Synthesis, Structural Characterization and Properties. *CrystEngComm* **2014**, *16* (10), 1985–1994.
- (134) Horike, S.; Bureekaew, S.; Kitagawa, S. Coordination Pillared-Layer Type Compounds Having Pore Surface Functionalization by Anionic Sulfonate Groups. *Chem. Commun.* **2008**, *0* (4), 471–473.
- (135) Li, X.; Wu, B.-L.; Niu, C.-Y.; Niu, Y.-Y.; Zhang, H.-Y. Syntheses of Metal–2-(Pyridin-4-Y1)-1 H -Imidazole-4,5-Dicarboxylate Networks with Topological Diversity: Gas Adsorption, Thermal Stability and Fluorescent Emission Properties. *Cryst. Growth Des.* **2009**, *9* (8), 3423–3431.
- (136) Zhao, T.; Jing, X.; Wang, J.; Wang, D.; Li, G.; Huo, Q.; Liu, Y. Assembly of Two 3D Porous Metal–Organic Frameworks Based on 1,2,3-Triazole-4,5-Dicarboxylate Exhibiting Novel Coordination Modes. *Cryst. Growth Des.* **2012**, *12* (11), 5456–5461.
- (137) Taddei, M.; Costantino, F.; Ienco, A.; Comotti, A.; Dau, P. V.; Cohen, S. M. Synthesis, Breathing, and Gas Sorption Study of the First Isostructural Mixed-Linker Phosphonate Based Metal–organic Frameworks. *Chem. Commun.* **2013**, *49* (13), 1315–1317.

- (138) Xie, L.-H.; Lin, J.-B.; Liu, X.-M.; Wang, Y.; Zhang, W.-X.; Zhang, J.-P.; Chen, X.-M. Porous Coordination Polymer with Flexibility Imparted by Coordinatively Changeable Lithium Ions on the Pore Surface. *Inorg. Chem.* **2010**, *49* (3), 1158–1165.
- (139) Zhang, M.; Chen, Y.-P.; Zhou, H.-C. Structural Design of Porous Coordination Networks from Tetrahedral Building Units. *CrystEngComm* **2013**, *15* (45), 9544–9552.
- (140) Gotthardt, J. M.; White, K. F.; Abrahams, B. F.; Ritchie, C.; Boskovic, C. Fluorite Topology in Lanthanoid Coordination Polymers with Di- and Trimetallic Building Blocks. *Cryst. Growth Des.* **2012**, *12* (9), 4425–4430.
- (141) Jiang, J.; Furukawa, H.; Zhang, Y.-B.; Yaghi, O. M. High Methane Storage Working Capacity in Metal–Organic Frameworks with Acrylate Links. *J. Am. Chem. Soc.* **2016**, *138* (32), 10244–10251.
- (142) Zhang, H.; Deria, P.; Farha, O. K.; Hupp, J. T.; Snurr, R. Q. A Thermodynamic Tank Model for Studying the Effect of Higher Hydrocarbons on Natural Gas Storage in Metal–organic Frameworks. *Energy Environ. Sci.* **2015**, *8* (5), 1501–1510.
- (143) Platero-Prats, A. E.; Li, Z.; Gallington, L. C.; Peters, A. W.; Hupp, J. T.; Farha, O. K.; Chapman, K. W. Addressing the Characterisation Challenge to Understand Catalysis in MOFs: The Case of Nanoscale Cu Supported in NU-1000. *Faraday Discuss.* **2017**, *201* (0), 337–350.
- (144) Britt, D.; Lee, C.; Uribe-Romo, F. J.; Furukawa, H.; Yaghi, O. M. Ring-Opening Reactions within Porous Metal–Organic Frameworks. *Inorg. Chem.* **2010**, *49* (14), 6387–6389.
- (145) Moon, S.-Y.; Wagner, G. W.; Mondloch, J. E.; Peterson, G. W.; DeCoste, J. B.; Hupp, J. T.; Farha, O. K. Effective, Facile, and Selective Hydrolysis of the Chemical Warfare Agent VX Using Zr₆-Based Metal–Organic Frameworks. *Inorg. Chem.* **2015**, *54* (22), 10829–10833.
- (146) Wang, G.; Sharp, C.; Plonka, A. M.; Wang, Q.; Frenkel, A. I.; Guo, W.; Hill, C.; Smith, C.; Kollar, J.; Troya, D.; Morris, J. R. Mechanism and Kinetics for Reaction of the Chemical Warfare Agent Simulant, DMMP (g), with Zirconium(IV) MOFs: An Ultrahigh-Vacuum and DFT Study. *J. Phys. Chem. C* **2017**, *121* (21), 11261–11272.
- (147) Cho, H.-Y.; Yang, D.-A.; Kim, J.; Jeong, S.-Y.; Ahn, W.-S. CO₂ Adsorption and Catalytic Application of Co-MOF-74 Synthesized by Microwave Heating. *Catal. Today* **2012**, *185* (1), 35–40.
- (148) Demessence, A.; D’Alessandro, D. M.; Foo, M. L.; Long, J. R. Strong CO₂ Binding in a Water-Stable, Triazolate-Bridged Metal–Organic Framework Functionalized with Ethylenediamine. *J. Am. Chem. Soc.* **2009**, *131* (25), 8784–8786.
- (149) Zhang, Z.; Li, Z.; Li, J. Computational Study of Adsorption and Separation of CO₂, CH₄, and N₂ by an *Rht*-Type Metal–Organic Framework. *Langmuir* **2012**, *28* (33), 12122–12133.
- (150) Mason, J. A.; Sumida, K.; Herm, Z. R.; Krishna, R.; Long, J. R. Evaluating Metal–organic Frameworks for Post-Combustion Carbon Dioxide Capture via Temperature Swing Adsorption. *Energy Environ. Sci.* **2011**, *4* (8), 3030.
- (151) Wang, X.-J.; Li, P.-Z.; Chen, Y.; Zhang, Q.; Zhang, H.; Chan, X. X.; Ganguly, R.; Li, Y.; Jiang, J.; Zhao, Y. A Rationally Designed Nitrogen-Rich Metal–Organic Framework and Its Exceptionally High CO₂ and H₂ Uptake Capability. *Sci. Rep.* **2013**, *3* (1), 1149.
- (152) Pillai, R. S.; Benoit, V.; Orsi, A.; Llewellyn, P. L.; Wright, P. A.; Maurin, G. Highly Selective CO

- ₂ Capture by Small Pore Scandium-Based Metal–Organic Frameworks. *J. Phys. Chem. C* **2015**, *119* (41), 23592–23598.
- (153) Nugent, P.; Belmabkhout, Y.; Burd, S. D.; Cairns, A. J.; Luebke, R.; Forrest, K.; Pham, T.; Ma, S. Q.; Space, B.; Wojtas, L.; Eddaoudi, M.; Zaworotko, M. J. Porous Materials with Optimal Adsorption Thermodynamics and Kinetics for CO₂ Separation. *Nature* **2013**, *495* (7439), 80–84.
- (154) Elsaïdi, S. K.; Mohamed, M. H.; Schaefer, H. T.; Kumar, A.; Lusi, M.; Pham, T.; Forrest, K. A.; Space, B.; Xu, W.; Halder, G. J.; Liu, J.; Zaworotko, M. J.; Thallapally, P. K. Hydrophobic Pillared Square Grids for Selective Removal of CO₂ from Simulated Flue Gas. *Chem. Commun.* **2015**, *51* (85), 15530–15533.
- (155) Elsaïdi, S. K.; Mohamed, M. H.; Simon, C. M.; Braun, E.; Pham, T.; Forrest, K. A.; Xu, W.; Banerjee, D.; Space, B.; Zaworotko, M. J.; Thallapally, P. K. Effect of Ring Rotation upon Gas Adsorption in SIFSIX-3-M (M = Fe, Ni) Pillared Square Grid Networks. *Chem. Sci.* **2017**, *8* (3), 2373–2380.
- (156) Benoit, V.; Pillai, R. S.; Orsi, A.; Normand, P.; Jobic, H.; Nouar, F.; Billefont, P.; Bloch, E.; Bourrelly, S.; Devic, T.; Wright, P. A.; de Weireld, G.; Serre, C.; Maurin, G.; Llewellyn, P. L. MIL-91(Ti), a Small Pore Metal–organic Framework Which Fulfills Several Criteria: An Upscaled Green Synthesis, Excellent Water Stability, High CO₂ Selectivity and Fast CO₂ Transport. *J. Mater. Chem. A* **2016**, *4* (4), 1383–1389.
- (157) Hu, Z.; Wang, Y.; Farooq, S.; Zhao, D. A Highly Stable Metal–Organic Framework with Optimum Aperture Size for CO₂ Capture. *AIChE J.* **2017**, *63* (9), 4103–4114.
- (158) Xiang, S.; He, Y.; Zhang, Z.; Wu, H.; Zhou, W.; Krishna, R.; Chen, B. Microporous Metal–Organic Framework with Potential for Carbon Dioxide Capture at Ambient Conditions. *Nat. Commun.* **2012**, *3* (1), 954.
- (159) Zhang, Z.; Xian, S.; Xia, Q.; Wang, H.; Li, Z.; Li, J. Enhancement of CO₂ Adsorption and CO₂/N₂ Selectivity on ZIF-8 via Postsynthetic Modification. *AIChE J.* **2013**, *59* (6), 2195–2206.
- (160) Chae, H. K.; Siberio-Pérez, D. Y.; Kim, J.; Go, Y.; Eddaoudi, M.; Matzger, A. J.; O’Keeffe, M.; Yaghi, O. M. A Route to High Surface Area, Porosity and Inclusion of Large Molecules in Crystals. *Nature* **2004**, *427* (6974), 523–527.
- (161) Smit, B.; Reimer, J. A.; Oldenburg, C. M.; Bourg, I. C. *Introduction to Carbon Capture and Sequestration*; Imperial College Press, 2014.
- (162) Cersosimo, M.; Brunetti, A.; Drioli, E.; Fiorino, F.; Dong, G.; Woo, K. T.; Lee, J.; Lee, Y. M.; Barbieri, G. Separation of CO₂ from Humidified Ternary Gas Mixtures Using Thermally Rearranged Polymeric Membranes. *J. Memb. Sci.* **2015**, *492*, 257–262.
- (163) Songolzadeh, M.; Soleimani, M.; Takht Ravanchi, M.; Songolzadeh, R. Carbon Dioxide Separation from Flue Gases: A Technological Review Emphasizing Reduction in Greenhouse Gas Emissions. *Sci. World J.* **2014**, *2014*.
- (164) Song, R.; Keller, A. A.; Suh, S. Rapid Life-Cycle Impact Screening Using Artificial Neural Networks. *Environ. Sci. Technol.* **2017**, *51* (18), 10777–10785.
- (165) Balabin, R. M.; Lomakina, E. I. Neural Network Approach to Quantum-Chemistry Data: Accurate Prediction of Density Functional Theory Energies. *J. Chem. Phys.* **2009**, *131* (7), 074104.

- (166) Pouryousefi, F.; Idem, R.; Supap, T.; Tontiwachwuthikul, P. Artificial Neural Networks for Accurate Prediction of Physical Properties of Aqueous Quaternary Systems of Carbon Dioxide (CO₂)-Loaded 4-(Diethylamino)-2-Butanol and Methyl-diethanolamine Blended with Monoethanolamine. *Ind. Eng. Chem. Res.* **2016**, *55* (44), 11614–11621.
- (167) Sundaram, N. Training Neural Networks for Pressure Swing Adsorption Processes. *Ind. Eng. Chem. Res.* **1999**, *38* (11), 4449–4457.
- (168) Lewandowski, J.; Lemcoff, N. O.; Palosaari, S. Use of Neural Networks in the Simulation and Optimization of Pressure Swing Adsorption Processes. *Chem. Eng. Technol.* **1998**, *21* (7), 593–597.
- (169) Khalighi, M.; Farooq, S.; Karimi, I. A. Optimizing the PSA Process of Propylene/Propane Using Neuro-Fuzzy Modeling. *11th Int. Symp. Process Syst. Eng.* **2012**, *31*, 1336–1340.
- (170) Sant Anna, H. R.; Barreto, A. G.; Tavares, F. W.; De Souza, M. B. Machine Learning Model and Optimization of a PSA Unit for Methane-Nitrogen Separation. *Comput. Chem. Eng.* **2017**, *104*, 377–391.
- (171) Demuth, H. B.; Beale, M. H.; Hagan, M. T. *The Neural Network Toolbox for MATLAB*; The MathWorks, 2014.
- (172) Brooke, A. K. D.; Meeraus, A.; Rosenthal, R. E. *GAMS: A User's Guide: Course Technology*; GAMS Development Corporation: Washington, DC, 1988.
- (173) Deb, K. *Multi-Objective Optimization Using Evolutionary Algorithms*, 1st ed.; John Wiley & Sons, Inc.: New York, NY, 2001.
- (174) Drud, A. CONOPT: A GRG Code for Large Sparse Dynamic Nonlinear Optimization Problems. *Math. Program.* **1985**, *31* (2), 153–191.

Appendix A: Nomenclature

A : area of column [m^2]

$C_{p,a}$: specific heat capacity of the adsorbed phase [J/mol/K]

$C_{p,g}$: specific heat capacity of the gas [J/mol/K]

$C_{p,s}$: specific heat capacity of the adsorbent [J/kg/K]

$C_{p,w}$: specific heat capacity of the wall [J/kg/K]

D : inner diameter of column [m]

D_m : molecular diffusivity of CO_2 - N_2 mixture [m^2/s]

D_L : axial dispersion coefficient [m^2/s]

F : molar feed flow rate [mol/s]

k_i : mass transfer coefficient of component i [s^{-1}]

h_{in} : inner heat transfer coefficient [$\text{W/m}^2/\text{K}$]

h_{out} : outer heat transfer coefficient [$\text{W/m}^2/\text{K}$]

H : enthalpy [J/mol]

K_w : thermal conductivity of the wall [W/m/K]

K_z : effective gas thermal conductivity [W/m/K]

L : length of column [m]

L_{wf} : length of column affected by the water front [m]

MW_i : Molecular weight of component i [kg/mol]

N : number of columns

P : pressure [Pa]

P_0 : Adsorption pressure [Pa]

\bar{P} : Dimensionless pressure

q_i : molar loading of component i in the solid phase [mol/kg]

q_i^* : equilibrium molar loading of component i in the solid phase [mol/kg]

q_{s0} : molar loading scaling factor [mol/kg]

r_i : column inner radius [m]

r_o : column outer radius [m]

r_p : radius of adsorbent pellet [m]

R : Universal Gas Constant [J/mol/K]

t_c : cycle time of the PSA unit [s]

t : time

T : temperature [K]

T_a : ambient temperature [K]

T_0 : Feed Temperature [K]

T_w : column wall temperature [K]

\bar{T} : Dimensionless temperature

\bar{T}_w : Dimensionless wall temperature

u_0 : Velocity scaling factor [m/s]

u_z : superficial gas velocity [m/s]

\bar{u}_z : dimensionless superficial gas velocity

U : internal energy [J/mol]

w_l : water mole fraction in feed gas to PSA unit

x_i : dimensionless molar loading of component i in the solid phase

x_i^* : dimensionless equilibrium molar loading of component i in the solid phase

y_i : mole fraction of component i in the gas phase

z : bed length coordinates [m]

Z : dimensionless length coordinates

Greek Symbols

α : water penalty factor

α_{LR} : light reflux ratio (fraction of the Feed light product that is sent to the light reflux step) [-]

α_{HR} : heavy reflux ratio (fraction of the light reflux heavy product that is sent to the heavy reflux step) [-]

ϵ : bed void fraction

μ : gas viscosity [Pa*s]

ρ_g : density of gas [mol/m³]

ρ_s : density of adsorbent [kg/m³]

ρ_w : density of wall [kg/m³]

π : dimensionless group in energy balances

τ : dimensionless time

Subscripts

ads: adsorption step

atm: atmospheric

depress: counter current depressurization step

H: high

i: index of component

in: stream coming in

j: stage number

L: low

out: stream coming out

pres: pressurization step

pur: purge step

Appendix B: Economic Equations and Equation Parameters

P/VSA Simulation and Isotherm Parameters

The CO₂, N₂, and the H₂O isotherm parameters for all of the materials, along with the operating variables used in the simulations are provided below.

Table B.1. Operating variables for the P/VSA simulations.

ε	0.37
r_p [mm]	1
k_{CO_2} [s ⁻¹]	0.1631
k_{N_2} [s ⁻¹]	0.2044
ρ_w [kg/m ³]	7800
$C_{p,a}$ [J/mol/K]	30.7
$C_{p,g}$ [J/mol/K]	30.7
$C_{p,s}$ [J/kg/K]	1070
$C_{p,w}$ [J/kg/K]	502
μ [Pa*s]	1.72×10^{-5}
D_m [m ² /s]	1.2995×10^{-5}
K_z [W/m/K]	0.09
K_w [W/m/K]	16
h_{in} [W/m ² /K]	8.6
h_{out} [W/m ² /K]	2.5
T_0 [K]	313
T_a [K]	298
u_0 [m/s]	1
q_{s0} [mol/kg]	5.84

Table B.2. Densities of the four adsorbents in chapter 3.

Material	Zeolite 13X	Zeolite 5A	HKUST-1	Ni-MOF-74
ρ_s [kg/m ³]	1130	1130	881	1195

Table B.3. Isotherm parameters for CO₂ and N₂ for zeolite 5A, HKUST-1 and Ni-MOF-74.

Parameter*	Zeolite 5A		HKUST-1		Ni-MOF-74	
	CO ₂	N ₂	CO ₂	N ₂	CO ₂	N ₂
b_i [kPa ⁻¹]	1.41×10^{-7}	3.71×10^{-7}	6.84×10^{-8}	6.81×10^{-7}	4.47×10^{-8}	1.40×10^{-7}
d_i [kPa ⁻¹]	0.00	0.00	4.52×10^{-6}	0.00	4.71×10^{-10}	0.00
$q_{b,i}$ [mol/kg]	3.4	3.30	12.4	8.00	6.21	11.9
$q_{d,i}$ [mol/kg]	0.00	0.00	1.16	0.00	7.15	0.00
$\Delta U_{b,i}$ [kJ/mol]	-37.4	-19.4	-25.7	-12.5	-37.8	-19.4
$\Delta U_{d,i}$ [kJ/mol]	0.00	0.00	-25.7	0.00	-37.8	0.00

Table B.4. Isotherm parameters for CO₂ and N₂ for zeolite 13X.

Parameter*	CO ₂	N ₂
b_i [m ³ /mol]	8.65×10^{-7}	2.50×10^{-6}
d_i [m ³ /mol]	2.63×10^{-8}	0.00
$q_{b,i}$ [mol/kg]	3.09	5.84
$q_{d,i}$ [mol/kg]	2.54	0.00
$\Delta U_{b,i}$ [kJ/mol]	-36.6	-15.8
$\Delta U_{d,i}$ [kJ/mol]	-35.7	0.00

* In the dual-site Langmuir isotherms, $q_{b,i}$ and $q_{d,i}$ are the saturation loadings of component i for the first and second sites, respectively, $\Delta U_{b,i}$ and $\Delta U_{d,i}$ are the heats of adsorption for component i for the first and second sites, respectively, and b_i and d_i are the isotherm parameters for component i for the first and second sites, respectively.

Table B.5. Water isotherm and impact parameters.

Zeolite 13X						
Parameters	a [mol/kg/kPa]	b [kPa ⁻¹]	t [-]	c [kg/mol]		
Values	35000	2333	0.383	0.337		
Zeolite 5A						
Parameters	a [mol/kg/kPa]	b [kPa ⁻¹]	t [-]	c [kg/mol]		
Values	3.56 x 10 ⁶	1.52 x 10 ⁵	0.18	0.337		
Ni-MOF-74						
Parameters	q _b [mol/kg]	b [kPa ⁻¹]	q _d [mol/kg]	d [kPa ⁻¹]	c [kg/mol]	
Values	27.7	16.42	0.975	0.27	0.142	
HKUST-1						
Parameters	a [kPa ⁻⁵]	b [kPa ⁻⁴]	c [kPa ⁻³]	d [kPa ⁻²]	e [kPa ⁻¹]	c [kg/mol]
Values	0.132	-2.25	13.5	-33.5	35.9	0.095

Process Objective Equations

The following equations are used to calculate the purity, recovery and mass balance of each stage.

$$moles_{CO_2, out|depr} = \frac{P_0 L}{RT_0} \varepsilon A \int_0^{\tau_{depr}} \bar{u}_z y_{CO_2} \frac{\bar{P}}{T} d\tau \quad \forall Z = 0^+$$

$$moles_{CO_2, out|pur} = \frac{P_0 L}{RT_0} \varepsilon A \int_0^{\tau_{pur}} \bar{u}_z y_{CO_2} \frac{\bar{P}}{T} d\tau \quad \forall Z = 0^+$$

$$moles_{total, out|depr} = \frac{P_0 L}{RT_0} \varepsilon A \int_0^{\tau_{depr}} \bar{u}_z \frac{\bar{P}}{T} d\tau \quad \forall Z = 0^+$$

$$moles_{total, out|pur} = \frac{P_0 L}{RT_0} \varepsilon A \int_0^{\tau_{pur}} \bar{u}_z \frac{\bar{P}}{T} d\tau \quad \forall Z = 0^+$$

$$moles_{CO_2, out|ads} = \frac{P_0 L}{RT_0} \varepsilon A \int_0^{\tau_{ads}} \bar{u}_z y_{CO_2} \frac{\bar{P}}{T} d\tau \quad \forall Z = 1^-$$

$$moles_{CO_2, in|ads} = \frac{P_0 L}{RT_0} \varepsilon A \int_0^{\tau_{ads}} \bar{u}_z y_{CO_2} \frac{\bar{P}}{T} d\tau \quad \forall Z = 0^+$$

$$moles_{CO_2, in|pr} = \frac{P_0 L}{RT_0} \varepsilon A \int_0^{\tau_{pr}} \bar{u}_z y_{CO_2} \frac{\bar{P}}{T} d\tau \quad \forall Z = 0^+$$

$$moles_{CO_2, in|pur} = \frac{P_0 L}{RT_0} \varepsilon A \int_0^{\tau_{pur}} \bar{u}_z y_{CO_2} \frac{\bar{P}}{T} d\tau \quad \forall Z = 1^-$$

$$Pur = \frac{moles_{CO_2, out|depr} + moles_{CO_2, out|pur}}{moles_{total, out|depr} + moles_{total, out|pur}}$$

$$Rec = 1 - \frac{moles_{CO_2, out|ads}}{moles_{CO_2, in|pres} + moles_{CO_2, in|ads}}$$

$$Mass\ Balance = \frac{moles_{CO_2, out|depr} + moles_{CO_2, out|pur} + moles_{CO_2, out|ads}}{moles_{CO_2, in|pres} + moles_{CO_2, in|ads} + moles_{CO_2, in|pur}}$$

Economic Equations

The total annualized cost (TAC) of the P/VSA system, dehydration technology and the post separation compression is calculated as followed:

$$TAC = ACC + AOC + PSCC + DC$$

where ACC and AOC are the Annualized Capital Cost and Annualized Operating Cost of the P/VSA system, PSCC is the overall annual cost of the post separation compression (PSC) system, and DC is the overall annual dehydration cost. The cost parameters used in the economic evaluation can be found in Table S6.

Table B.1. Economic Parameters.

Interest Rate	10%
Life Span of Equipment	20 years
Cost of TEG	\$2000/ ton
Cost of Electricity	\$0.06 / kWh
Operating Time	8000 hours/year
Cost of Cooling Water	\$0.02/m ³
Cost of Natural Gas	\$4.76 / MMBtu
Cost of Chilled Water	\$4/GJ

P/VSA System

The annualized capital cost is defined as:

$$ACC = \sum_j \left(\phi_{equip} C_{bm, equip, j} + \phi_{adsorb} C_{adsorb, j} + MC_j \right)$$

where ϕ_{equip} and ϕ_{adsorb} are the annualization factors for the equipment and adsorbents, respectively, $C_{bm, equip, j}$ is the bare module cost for the equipment and $C_{adsorb, j}$ is the cost of the adsorbent. The maintenance cost is assumed to be equal to 5% of the annualized equipment costs.

The equipment cost is calculated as follows:

$$C_{bm, equip, j} = N_{col, j} \left(F_{bm, comp} C_{p, comp, j} + F_{bm, vac} C_{p, vac, j} + F_{bm, col} C_{p, col, j} \right)$$

where F_{bm} is the bare module factor for each piece of equipment and $C_{p, comp}$, $C_{p, vac}$ and $C_{p, col}$ are the purchase cost of the compressor, vacuum pump and column, respectively. We use a bare module factor of 2.15 for the compressors and vacuums and 4.15 for the column.

The purchase cost of the column is calculated using the following equation:

$$C_{p,col,j} = C_{v,j} + C_{pl,j} + C_{dr,j}$$

where $C_{v,j}$ is the cost of the vessel for a single column in stage j with a weight of W_j , $C_{pl,j}$ is the cost of the platforms and ladders and $C_{dr,j}$ is the cost of the flow distributor. These are calculated as follows:

$$W_{col,j} = \pi (2r_{in} + t_{col})(L + 1.6r_{in})t_{col}\rho_{col}$$

$$C_{v,j} = \exp \left[7.0132 + 0.18255 \ln(2.2W_{col,j}) + 0.02297 \ln(2.2W_{col,j})^2 \right]$$

$$C_{pl,j} = \left((6.56r_{in,j})^{0.7396} \right) \left((3.28L_j)^{0.70684} \right)$$

$$C_{dr,j} = 125\pi (3.28r_{in,j})^2$$

where L_j and $r_{in,j}$ are the length and radius of the columns in stage j , t_{col} is the thickness of the column and ρ_s is the density of the material. We use carbon steel for the column with a density of 7800 kg/m³ and a thickness of 0.015 m.

The purchase cost of the vacuum pumps for stage j , $C_{p,vac,j}$, is calculated as follows:

$$\mathcal{G}_j = 0.588 \frac{y_{0,j} \text{Rec}_j F_j}{\text{Pur}_j} \frac{RT_0}{P_{L,j}}$$

$$C_{p,vac,j} = 8250 (\mathcal{G}_j)^{0.35}$$

where $y_{0,j}$ is the mole fraction of CO₂ in the feed gas, Rec_j is the CO₂ recovery, Pur_j is the purity of the CO₂ product, and $P_{L,j}$ is the purge pressure.

The purchase cost of the compressor, $C_{p,comp,j}$, is calculated using the following expressions.

$$Power_{ads,j} = \frac{1}{\eta} RT_0 F_j \frac{\gamma}{\gamma-1} \left[\left(\frac{1.05 P_{0,j}}{P_{atm}} \right)^{(\gamma-1)/\gamma} - 1 \right]$$

$$C_{p,compressor,j} = \begin{cases} \exp \left[6.8929 + 0.79 \ln \left(\frac{Power_{ads}}{745.7} \right) \right] & \text{if } P_0 \leq 2 \text{ bar} \\ \exp \left[7.58 + 0.8 \ln \left(\frac{Power_{ads}}{745.7} \right) \right] & \text{if } P_0 > 2 \text{ bar} \end{cases}$$

where η is the efficiency of the compressor/vacuum pump. It is noted that either a blower or a compressor is able to perform the compression duties for the P/VSA cycles. If the adsorption pressure is below 2 bar, the blower is used with an efficiency of 80%. If the adsorption pressure is above 2 bar, than a compressor with an efficiency of 75% is used.

The purchase cost of the adsorbent is calculated with the following expression:

$$C_{p,adsorbent} = C_{pk} \rho_s V_p$$

$$V_p = \pi r_{in}^2 L$$

where C_{pk} is the cost of the adsorbent, ρ_s is the density of the adsorbent and V_p is the packing volume of the adsorbent.

Finally, the operating cost, OC_j is calculated as follows:

$$AOC = \sum_j EC \left(W_{pres,j} + W_{ads,j} + W_{depress,j} + W_{pur,j} \right) \frac{8000 \cdot 3600}{t_{c,j}} N_{col,j}$$

where EC is the cost of electricity, $W_{pres,j}$, $W_{ads,j}$, $W_{depress,j}$ and $W_{pur,j}$ are the energy requirements for the pressurization, adsorption, depressurization and purge steps, respectively, and $t_{c,j}$ is the cycle time of stage j . The energy requirements are calculated as follows.

$$W_{pres,j} = \begin{cases} \frac{1}{\eta} \varepsilon \pi r_{in}^2 v_0 P_0 \frac{\gamma}{\gamma-1} \int_0^{t=t_{pres}} (\bar{v} \bar{P}|_{Z=0}) \left[\left(\frac{P_0 \bar{P}|_{Z=0}}{P_f} \right)^{(\gamma-1)/\gamma} - 1 \right] dt & \text{if } P|_{z=0} \geq P_f \\ 0 & \text{if } P|_{z=0} < P_f \end{cases}$$

$$W_{ads,j} = \frac{1}{\eta} \varepsilon \pi r_{in}^2 v_0 P_0 \frac{\gamma}{\gamma-1} \int_0^{t=t_{ads}} (\bar{v} \bar{P}|_{Z=0}) \left[\left(\frac{P_0 \bar{P}|_{Z=0}}{P_f} \right)^{(\gamma-1)/\gamma} - 1 \right] dt$$

$$W_{depress,j} = \begin{cases} \frac{1}{\eta} \varepsilon \pi r_{in}^2 v_0 P_0 \frac{\gamma}{\gamma-1} \int_0^{t=t_{depress}} (\bar{v} \bar{P}|_{Z=0}) \left[\left(\frac{P_{atm}}{P_0 \bar{P}|_{Z=0}} \right)^{(\gamma-1)/\gamma} - 1 \right] dt & \text{if } P|_{z=0} \leq P_{atm} \\ 0 & \text{if } P|_{z=0} > P_{atm} \end{cases}$$

$$W_{pur,j} = \frac{1}{\eta} \varepsilon \pi r_{in}^2 v_0 P_0 \frac{\gamma}{\gamma-1} \int_0^{t=t_{pur}} (\bar{v} \bar{P}|_{Z=0}) \left[\left(\frac{P_{atm}}{P_0 \bar{P}|_{Z=0}} \right)^{(\gamma-1)/\gamma} - 1 \right] dt$$

Post-Separation Compression

For calculating the cost of the PSC system, the following equation is used:

$$PSCC = \sum_1^{k=5} (C_{bm,comp,k} + AOC_{comp,k}) + \sum_1^{l=6} (C_{bm,HE,l} + AOC_{HE,l}) + (C_{bm,pump} + AOC_{pump})$$

where $C_{bm,comp,k}$ and $AOC_{comp,k}$ are the bare module cost for compressor k , $C_{bm,HE,l}$ and $AOC_{HE,l}$ are the bare module cost and operating costs for Heat Exchanger l , and $C_{bm,pump}$ and AOC_{pump} are the bare module cost and operating costs for the pump. It is noted that as shown in Figure 1, the PSC section consists of five compressors, six heat exchangers (five using cooling water as the coolant and one using chilled water) and a pump. The bare module cost for each piece of equipment is given as follows:

$$\begin{aligned}
C_{bm,comp} &= F_{bm,comp} F_{mat,comp} \exp \left[7.58 + 0.8 \ln \left(\frac{P_{PSC}}{745.7} \right) \right] \\
P_{comp,PSC} &= \frac{1}{\eta} \frac{\gamma}{\gamma-1} F_{product} RT_0 \left[(2.45)^{\frac{\gamma-1}{\gamma}} - 1 \right] \\
C_{bm,HE} &= F_{bm,HE} F_{mat,HE} F_{P,HE} \exp \left[11.147 + 0.9186 \ln(A_{HE}) + 0.0979 \ln(A_{HE})^2 \right] \\
C_{bm,pump} &= F_{bm,pump} (F_{mat,pump} C_{p,pump} + C_{p,dr}) \\
C_{p,dr} &= \exp \left[5.8259 + 0.13141 \ln \left(\frac{P_{pump,PSC}}{\eta_{motor} \eta_{pump}} \right) + 0.053255 \ln \left(\frac{P_{pump,PSC}}{\eta_{motor} \eta_{pump}} \right)^2 \right. \\
&\quad \left. + 0.028628 \ln \left(\frac{P_{pump,PSC}}{\eta_{motor} \eta_{pump}} \right)^3 - 0.0035549 \ln \left(\frac{P_{pump,PSC}}{\eta_{motor} \eta_{pump}} \right)^4 \right] \\
P_{pump,PSC} &= 9.81 Q_{product} H \rho_{product,l} \\
C_{p,pump} &= \exp \left[9.7171 - 0.6019 \ln(Q_{product} H^{0.5}) + 0.0519 \ln(Q_{product} H^{0.5})^2 \right]
\end{aligned}$$

where F_{mat} are the material factors for the equipment, $F_{product}$ is the molar feed rate of the CO₂ product stream, $F_{P,HE}$ is the pressure factor for the heat exchangers, $Q_{product}$ is the volumetric flow rate of the liquid CO₂ product, H is the required pump head of the pump η_{motor} and η_{pump} are the efficiencies of the motor and pump, respectively, $\rho_{product,l}$ is the density of the liquid product and $p_{pump,psc}$ is the power requirements from the pump. We assumed that the liquid density of the product is 770 kg per m³.

The Annualized Operating Costs of the PSC section is calculated as follows:

$$\begin{aligned}
AOC_{comp,k} &= 8 p_{PSC} EC \\
AOC_{HE,l} &= C_{cool,k} Q_{cool,k} \\
AOC_{pump} &= EC \frac{P_{pump,PSC}}{\eta_{pump} \eta_{drive}}
\end{aligned}$$

where $C_{cool,k}$ and $Q_{cool,k}$ are the cost and volumetric flow rate requirements of coolant needed for Heat Exchanger k .

Dehydration Schemes

Both the Cooling and Condensing (C&C) and triethylene absorption (TEG) dehydration schemes are modeled in Aspen HYSYS using the UNIQUAC Fluids package. Based off of the results of the simulations, the annualized cost for each scheme is estimated using cost equations from literature.¹

For the C&C scheme, the Total Annualized Cost is calculated using the following equation.

$$TAC_{C\&C} = (EC \cdot P_{comp} + CWC \cdot Q_{HE}) + \left(C_{bm,comp} + C_{bm,vessel} + \sum_m C_{bm,HE,m} \right)$$

where P_{comp} is the power requirements of the compressor, CWC is the cost of the cooling water, Q_{HE} is the necessary flow rate of water required by the heat exchangers, and $C_{p,comp}$, $C_{p,HE,m}$ and $C_{p,vessel}$ are the purchase cost of the compressor, the heat exchanger and the vessel. These purchase costs are calculated using the following equations

$$C_{bm,comp} = F_{bm,comp} C_{p,comp}$$

$$C_{bm,HE,m} = F_{bm,HE} C_{p,HE,m}$$

$$C_{bm,vessel} = F_{bm,vessel} C_{p,vessel}$$

$$\log_{10} C_{p,comp} = 2.2897 + 1.3604 \log_{10} (P_{comp}) - 0.1027 \log_{10} (P_{comp})^2$$

$$\log_{10} C_{p,HE,m} = 4.8306 - 0.8509 \log_{10} (A_m) + 0.3187 \log_{10} (A_m)^2$$

$$\log_{10} C_{p,vessel} = 3.4974 + 0.4485 \log_{10} (V) + 0.1074 \log_{10} (V)^2$$

where A_i is the heat transfer area of heat exchanger m in m^2 , V is the volume of the process vessel in m^3 and P_{comp} is in units of kW. We used a bare module factor of 2.27 for the compressor, 3.29 for the heat exchangers and 4.07 for the process vessel.

For the TEG dehydration scheme, the Total Annualized Cost was calculated using the following equation.

$$TAC_{TEG} = \left(EC \cdot P_{pump} + CWC \cdot Q_{HE} + MU_{TEG} C_{TEG} + HR \cdot C_{NG} \right) + \left(C_{bm,vessel} + \sum_m C_{bm,HE,m} + C_{bm,pump} + C_{bm,FH} + \sum_n C_{bm,tower,n} \right)$$

where P_{pump} is the power requirements of the pump, MU_{TEG} is the makeup flowrate of triethylene glycol, HR is the heating requirements of the fired heater, C_{NG} is the cost of natural gas, C_{TEG} is the cost of triethylene glycol, $C_{p,pump}$ is the purchase cost of the pump, $C_{p,FH}$ is the purchase cost of the fired heater and $C_{p,tower,j}$ is the purchase cost of tower. For the heat exchangers and the vessel, the same equations are used. The purchase costs of the towers, pumps, and fire heater were calculated with the following equations.

$$\begin{aligned} C_{bm,FH} &= F_{bm,FH} C_{p,FH} \\ C_{bm,pump} &= F_{bm,pump} C_{p,pump} \\ C_{bm,tower,n} &= F_{bm,column,n} C_{p,column,n} + F_{bm,tray,n} C_{p,tray,n} \\ \log_{10} C_{p,FH} &= 2.0829 + 0.9074 \log_{10} (HR) - 0.0243 \log_{10} (HR)^2 \\ \log_{10} C_{p,pump} &= 3.3892 + 0.0536 \log_{10} (P_{pump}) - 0.1538 \log_{10} (P_{pump})^2 \\ \log_{10} C_{p,trays,n} &= 2.9949 + 0.4465 \log_{10} (A_{tray}) + 0.3961 \log_{10} (A_{tray})^2 \end{aligned}$$

where A_{tray} is the area of the tray in m^2 and P_{pump} is in kW. In calculating the purchase cost of tower m , the cost of the column is calculated using the same equations as the vessels above. The bare module factors used are 2 for the trays, 3.24 for the pump and 2.2 for the fire heater.

Appendix C: Competitive dual-site Langmuir isotherm validation

In order to perform the process level simulations, it is necessary calculate the CO₂/N₂ mixture loadings at various pressures, temperatures, and gas-phase mole fractions throughout the process simulation. Thus, one needs an analytical expression or some other way of very quickly calculating the mixture behavior from the single-component isotherms. As is common in the literature, we decided to use a two site competitive Langmuir isotherm to determine the mixture loadings at various pressures, temperatures, and gas-phase mole fractions. As mentioned in Chapter 4, the pure CO₂ and N₂ isotherms of the adsorbents were fitted simultaneously to a dual and single site Langmuir isotherm (equations 2 and 3 from main text), respectively. In order to employ the competitive isotherms, we assumed that the CO₂ site with the larger binding energy (site with the larger $B_{CO_2,s}$ term) only adsorbs CO₂. For the weaker CO₂ binding energy site, the CO₂ and the N₂ molecules compete for the adsorption sites. In order to maintain thermodynamic consistency for this site, the saturation loading for CO₂ and N₂ are set equal to each other on this site.¹²⁰ In order to confirm the accuracy of using this competitive isotherm model to predict mixture loadings, mixture GCMC simulations were run on ten random MOFs from the CoRE MOF data set. These mixture GCMC simulations were run up to 10 bar with a 15:85 CO₂/N₂ gas-phase composition at 313 K. The mixture simulation data were then compared to the predicted loading from the competitive isotherm model. The results from all ten MOFs are shown below. It is seen from the ten MOFs that the mixture loading results were predicted reasonably well by fitting competitive isotherms to the pure component loading data. The mean unsigned errors between the multicomponent Langmuir model and the GCMC data are 0.049 and 0.022 mol/kg for CO₂ and N₂, respectively.

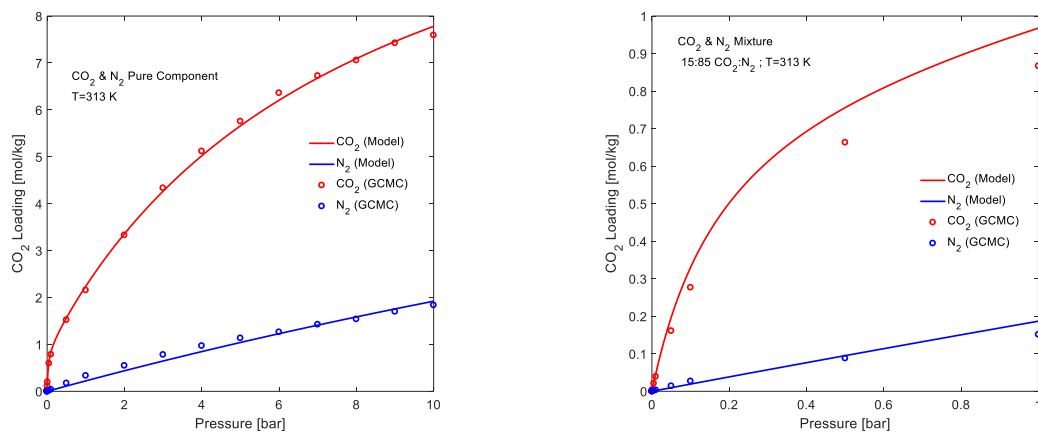


Figure C.1. Pure Component and Mixture Isotherms for AMIMEP

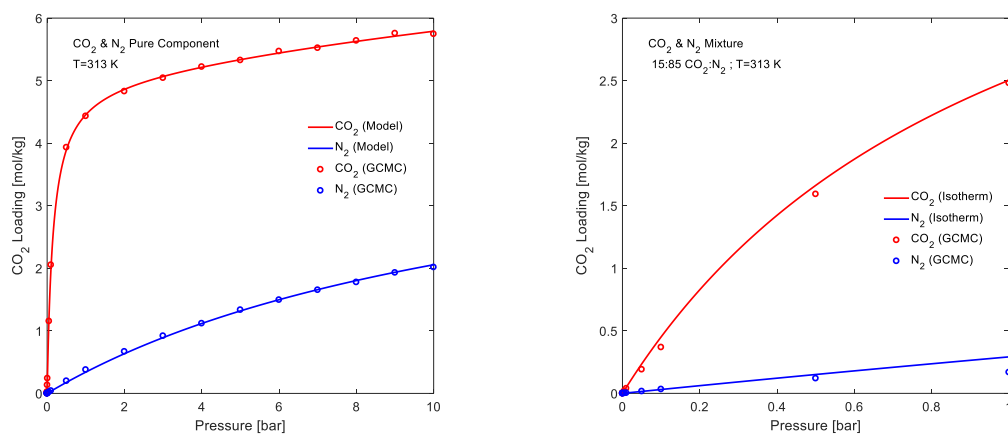


Figure C.2. Pure Component and Mixture Isotherms for FIJDIM12

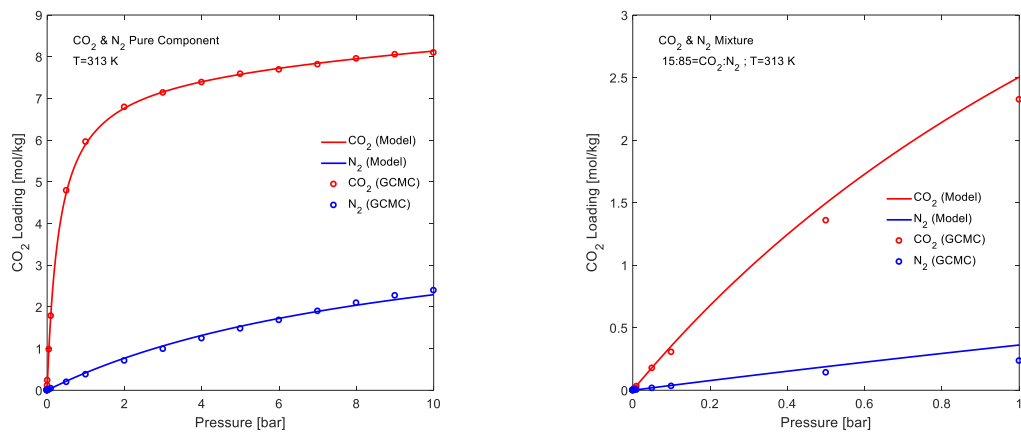


Figure C.3. Pure Component and Mixture Isotherms for MOF ISUCUV

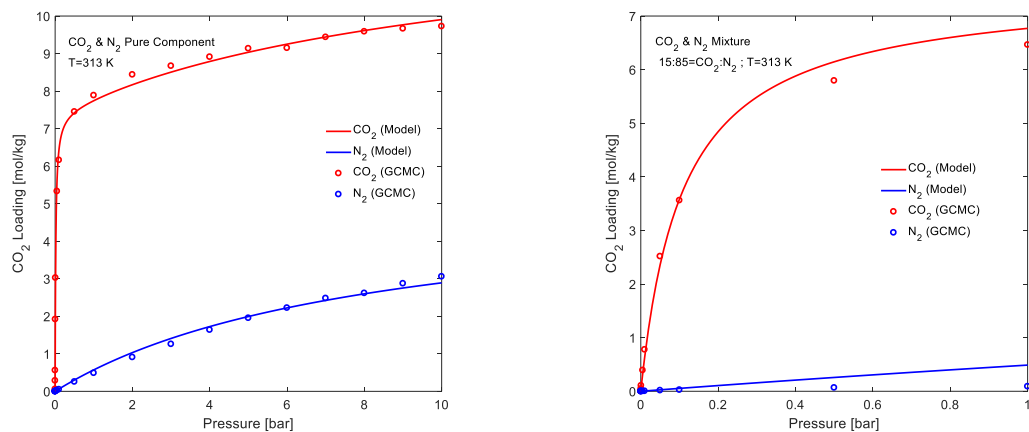


Figure C.4. Pure Component and Mixture Isotherms for LAGNEO

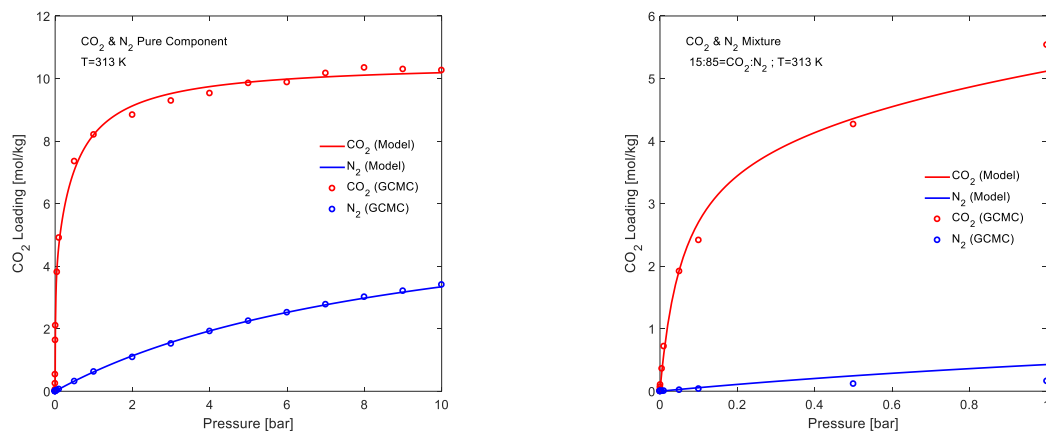


Figure C.5. Pure Component and Mixture Isotherms for LEVNOQ

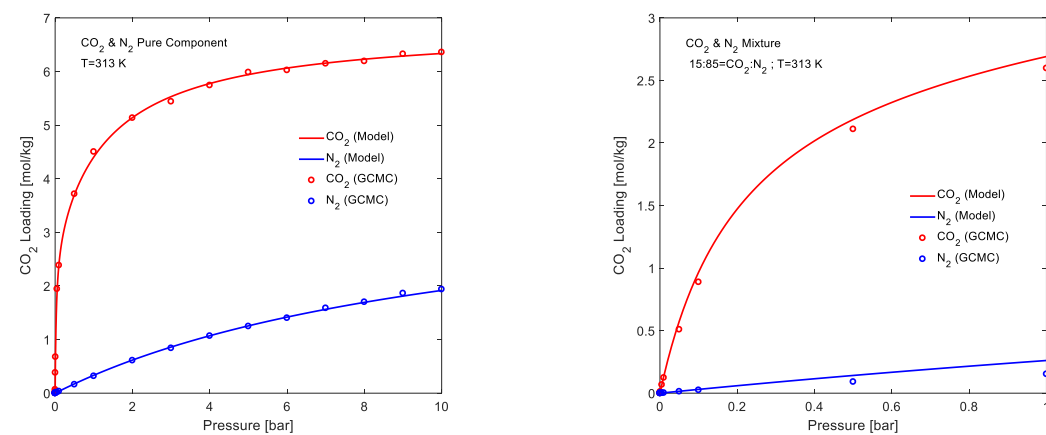


Figure C.6. Pure Component and Mixture Isotherms for LIGHAM

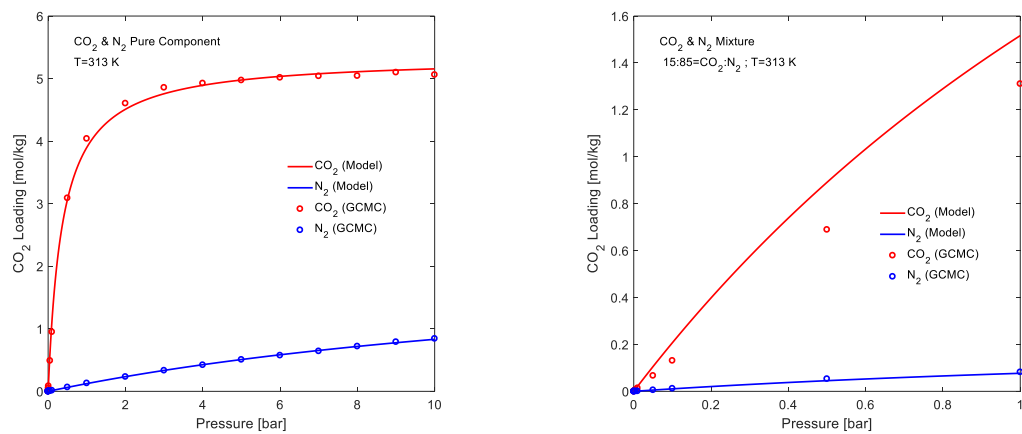


Figure C.7. Pure Component and Mixture Isotherms for NANMEW

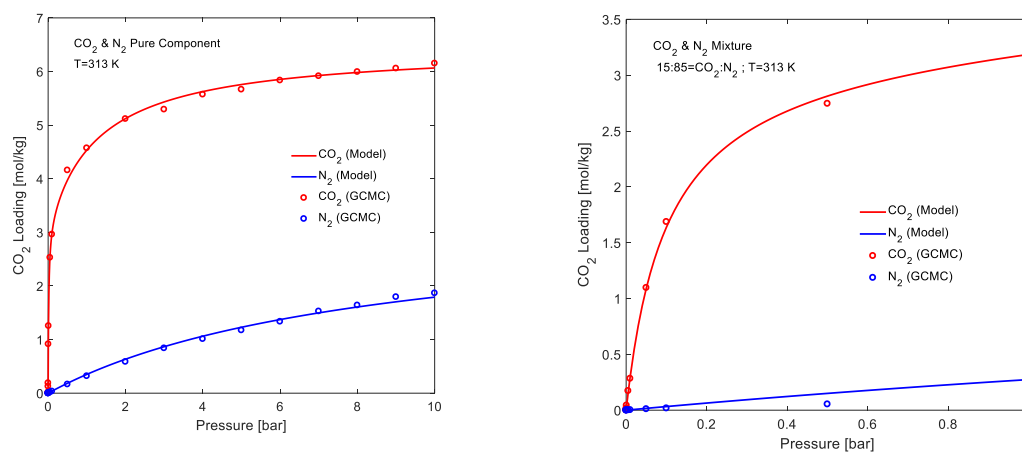


Figure C.8. Pure Component and Mixture Isotherms for QOCSAD

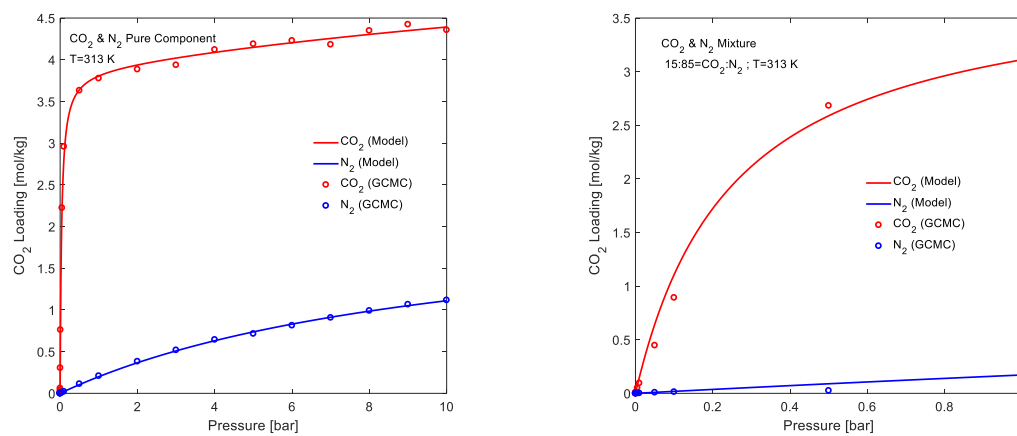


Figure C.9. Pure Component and Mixture Isotherms for MOF TISKOW

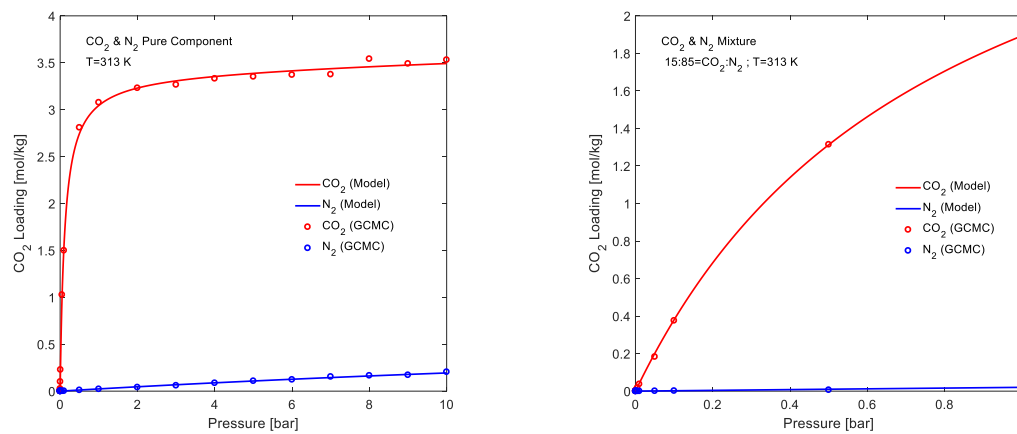


Figure C.10. Pure Component and Mixture Isotherms for XAMLUS

Appendix D: N₂ Heat of Adsorption Sensitivity Analysis

In most experimental studies looking into synthesizing new MOFs for CO₂ capture applications, the primary focus is on measuring the CO₂ isotherm at room temperature in order to be able to report the CO₂ working capacity. It is also quite common for studies to measure the isosteric heat of adsorption of CO₂ to see how strongly the CO₂ is binding to the MOF and the isotherm of N₂ at room temperature to calculate the selectivity of CO₂ over N₂. However, the isosteric heat of adsorption of N₂ is commonly not reported. This was the case for three of the MOFs that we examined in Chapter 5: Co-MOF-74, SIFSIX-3-Ni and SIFSIX-2-Cu-i. In order to see the impact the N₂ heat of adsorption has on the final results of the PSA analysis, we performed a sensitivity analysis on SIFSIX-2-Cu-i and Co-MOF-74. For both of these MOFs, N₂ isotherms were reported at 298 K. We took these isotherms and fitted the isotherm to an Arrhenius-type equation as noted above to account for temperature effects. Process-level optimization was performed for each N₂ heat of adsorption and the results are reported below in Figure D.1. In this analysis, we see there is a big difference in the range of CO₂ purities between the two MOFs. While the range was only 2% for SIFSIX-2-Cu-i, the range for Co-MOF-74 was higher at 6%. However, for both MOFs we see that the choice of N₂ heat of adsorption value did not determine whether the MOF achieved the DOE's goal or not. SIFSIX-2-Cu-i was able to exceed the goal no matter the N₂ heat of adsorption value, and Co-MOF-74 was unable to meet the goal no matter the heat of adsorption value. From this analysis, if N₂ heat of adsorption data was unable to be obtained for a specific MOF, but the remaining information was found, we assumed the N₂ heat of adsorption was 12 kJ/mol.

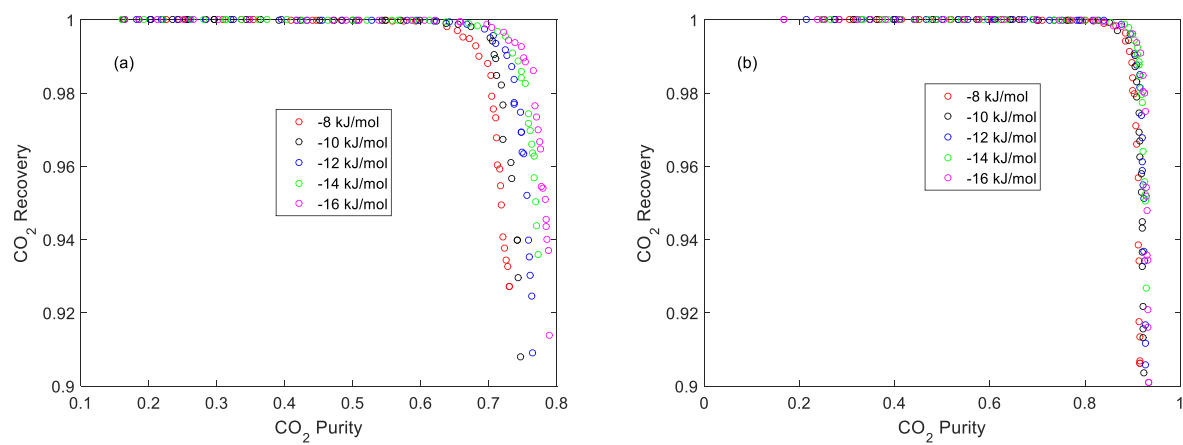


Figure D.1. Purity / recovery Pareto fronts for (a) Co-MOF-74 and (b) SIFSIX-2-Cu-i, with N₂ heat ranging from -8 kJ/mol to -16 kJ/mol. While the range in CO₂ purity was significant, 73% - 79%, the range for SIFSIX-2-Cu-i was smaller, 91% - 93%.